UNIVERSITÀ
DEGLI STUDI
DI PADOVA

Sede Amministrativa: Università degli Studi di Padova

Dipartimento di Ingegneria Industriale

CORSO DI DOTTORATO DI RICERCA IN: INGEGNERIA INDUSTRIALE

CURRICOLO: INGEGNERIA MECCANICA

CICLO XXX

Enhancing optical measuring systems for manufacturing process control

Coordinatore: Ch.mo Prof. Paolo Colombo

Supervisore: Ch.mo Prof. Enrico Savio

Co-Supervisore: Ch.mo Prof. Simone Carmignato

Dottorando: Fabrizio Medeossi

Alla mia Famiglia,

a Martina,

a Me.

Abstract

Modern industries are stressed by the market for a crazy and continuous reduction of time-to-market and an increase of required quality of final products. Manufacturing should evolve in order to satisfy market, by increasing the process complexity and fighting against requirements (in terms of batch sizes and tolerances). Production should be fast and accurate and this implies that measuring systems have to be faster, more flexible and possibly in-line, in order to continuously adjust the process. Optical metrology seems to be the perfect solution for this challenging context. However, optical metrology is characterized by binding physical limitations that reduce accuracy and sometimes applicability. Nevertheless, the exponential increase of computational power helps the evolution and optimization of optical measuring systems by permitting real time corrections and fast post-process. The aim of this work is the development of different correction and numerical methods to enhance optical measuring system capabilities. Confocal microscopy, optical CMM (coordinate measuring systems) and X-ray computed tomography are analysed in different types of applications, ensuring a reduction of measuring process variability and increasing measurement accuracy. Algorithms developed specifically for quantification and minimization of influencing factors are presented and implemented for real time correction and control of manufacturing process. Void pixels in confocal microscopy are studied and managed, thus reducing variability of surface roughness parameters and increasing capabilities of measuring instrument for micro-milling process control. Optical systems are analysed for thread measurements proposing a correction method for inline, fast and reliable evaluation of threads geometry. Finally, surface roughness is taken into account for correction of computed tomography dimensional measurements. Different technologies applied in different fields are joined by the common need of correction for enhancing measuring capabilities.

Contents

List of figures

List of Tables

Introduction

Metrology in production engineering must be fast, accurate, robust and automated, and ideally integrated into the production line. These characteristics are necessary in order to reduce the cost and increase the benefits of the measuring steps. Optical methods and in general non-contact systems seem to fulfil these requirements. For these reasons, for over a century optical methods have played and are still playing an important role in dimensional measurement (Schwenke et al. 2002). Different technologies were developed in the past, based on different physical principle. Clearly, measurements can be performed with a variety of instruments, which have different capabilities and limitations, from optical profilers to X-ray computed tomography. Limitations are the focus of this research, considering the application of non-contact metrology in four different fields. Physical limitations of different systems are analysed and studied in order to overcome them in some cases and in some others use these limitations in an original way. Therefore, finally, the main goal of the research is the development of methods for improving optical measurements. Study of correction algorithms for the quantification and minimization of influencing factors in order to enhance capabilities of optical instruments (in surface characterization and control of the machining process).

Firstly, an analysis of the optical systems in production environments is presented, considering also the economic and technological benefits. This chapter is mainly focused on the application of optical systems, trying to present the actual situation. Correction methods are necessary for flexibility, moreover for some particular applications, in which the accuracy could be increased.

The second chapter is focused on surface characterization. The variability of surface roughness parameters is analysed. As well described in Leach's publications (Leach 2011; Leach 2013), local slopes, defects, scanning speed, light intensity and material transparency etc. cause local measuring defects in the topographies and in general in optical measuring systems. These defects could be treated in different ways, as well described by MacAulay (MacAulay 2015) in NPL (National Physical Laboratories) publication: treated using a best fit value or interpolation methods using the neighbours value, or ignore them for not introducing additional error. A lot of work was developed in trying to solve the problem of identification and indexing of these points (for example

the works of Wang, Blunt Scott, Senin). But a small percentage of void pixels is unavoidable, in particular in confocal microscopy. These pixels affects the variability of the parameters. An extended study on real and numerically generated surfaces is presented for quantifying this effect. This quantification highlights the beneficial effect of the reconstruction in terms of variability reduction.

In addition, the void pixels were also used to improve the capabilities of confocal microscopy for micromachining process quality control. This is the focus of the third chapter in which a newly method for burrs detection is presented. A complete characterization of the machined slot requires a control of the geometry, roughness but also burrs presence and dimensions, in order to decide if deburring processes are necessary or not. Optical systems, based on cameras, microscopes, laser, interferometers, conoscopic holography and triangulation were developed by different authors in the past (Ko & Park 2006). This systems are advantageous respect to the contact systems (used in machining processes but not compatible with micromachining burrs dimensions), as they allow preserving the burrs while measuring them. Though, even if they are suitable for micro-burrs detection, they are not designed for in-line measurements. On the other hand, Tsai (Tsai & Lu 1996) developed a machine vision system based on automatic contour detection for burrs and peripheral defects of casting parts, but limited to macro-sized burrs. However, systems developed exclusively for burrs measurement, either macro or micro, are not flexible enough for a comprehensive quality control of the micro-machined part, since, applying these methods, additional measuring instruments have to be set-up inline for the verification of the geometry and surface roughness quality of the part. The proposed method try to enlarge the capabilities of confocal microscopy, overcoming the limitation related to the steep surfaces, and using this limitation in a different way. Void pixels are treated in order to evaluate the burrs width and enlarge the capabilities of the confocal microscopy: a complete quality control of the micro machined slot through a single and in-line measurement step.

Then, in the next chapter, correction methods are applied to a shadow based optical measuring system. An optical in-line system developed specifically for the thread measurements is analysed and the shadow generated by the system is corrected in order to obtain reliable threads parameters (the shadow is distorted respect to the section of the thread). The correction method is developed starting from the mathematical formulations available from Lotze's (Lotze & Will 1991) publications and try to overcome the

limitations of different patents in this field. The final result permits to enhance the capabilities of the system, improving the accuracy in threads measurement and ensuring the comparison with the calibrated values.

On the other side, the study of the effect of surface roughness in dimensional metrology using Computed Tomography systems (CT-systems) ensures a reduction of the uncertainty associated with this effect. The relevant deviations between CT and tactile dimensional measurements were studied in the past mainly in Niggemann and Bartscher publications (Schmitt & Niggemann 2010; Kruth et al. 2011), considering the roughness effect as one of the uncertainty contributions. Boeckmans and Aloisi (Boeckmans et al. 2015; Aloisi et al. 2015) showed that the roughness effect could be considered as a systematic effect in some particular cases. A generalized correction is obtained through an extended and combined experimental-numerical study, studying the relations between surface morphology and measurement deviations. The proposed correction, presented in the last chapter, reduces the uncertainty of the CT measurement result considering the surface roughness effect as a systematic error.

1. Optical measuring systems in manufacturing

Lord Kelvin said: “I often say that when you can measure what you are speaking about, and express it in numbers, you know something about it; but when you cannot measure it, when you cannot express it in numbers, your knowledge is meagre and of unsatisfactory kind; it may be the beginning of knowledge, but you have scarcely in your thoughts advanced to the stage of science, whatever the matter may be.” Measurement are done to gain reliable quantified information about the world. This is valid for all kinds of research, in natural sciences and engineering. Metrology is generally recognized as an important part of the technological process, in particular in manufacturing processes. But it is also seen as being a cost factor and very seldom as being a value-adding activity (Kunzmann et al. 2005). Instead of considering metrology as a basis for decision-making, process control, manufacture and function, sometimes it is considered as an additional and unnecessary expense. Otherwise, in any advanced mass production the metrology equipment are largely present (Savio et al. 2016). A lot of work was developed for the quantification of costs strictly connected with metrology (Savio 2012), trying to developed and propose methodology for the evaluation of the impact of metrology in manufacturing. Otherwise it is clear that the mutual relations among quality, production planning and maintenance control should not be underestimated while configuring and managing the manufacturing system as a whole (Colledani et al. 2014). Therefore, metrology stages and systems should be designed in order to be suitable for the modern manufacturing requirements. High productivity and flexibility implies also flexible and fast measuring systems. Metrology should be thought as an essential tool to achieve a complete understanding and control of the manufacturing process. Manufacturing companies are continuously facing the challenge of operating their manufacturing processes and systems in order to deliver the required production rates of high quality products, while minimizing the use of resources (Colledani et al. 2014). Product quality and delivery reliability are key factors for success in the manufacturing industry. Moreover, the increasing emphasis on sustainable production requires maintaining the resource efficiency and effectiveness along the product, process and production system life cycle (Takata et al. 2004). Clearly in order to reduce the economic impact of the measurement steps, it should be performed as early as possible in the production process.

If a defective part can be identified early, there is no reason for further processing. Further, the economic impact of defective parts rises as the production process progresses. This is fundamental for both productive and process viewpoint. Early measurements allow to gain knowledge about specific production process steps and about the feasibility of subsequent steps (Kunzmann et al. 2005), moreover for process optimisation it is clearly convenient to acquire measurement data not only at the end of the entire production process, especially for complex, multi-step production processes. Measurements directly after a production process step allow for selective optimisation of the individual step (Hocken & Pereira 2017). Therefore, process optimisation can be broken down into simplified subtasks. Moreover, effects of a production process step on the geometry after subsequent process steps could be assessed, given that models of the involved steps are available. Process improvement is also a key factor for increasing quality in all the modern quality management methodologies (e.g. SixSigma, ISO 9000). Considering the modern definition of quality, the final goal is everytime a minimization of the variability in the output of a production process. In statistical process control (SPC) this could be achieved by identifying and eliminating the causes that generate large process variations. Then in Engineering process control (EPC) all the process parameters are adjusted online such that the process output is as close to the target as possible (Butte & Tang 2008). But finally, in order to apply different statistical techniques for modelling and controlling the process, is necessary to collect as much output as possible from the production process (e.g. geometrical characteristics). So finally, also from a statistical point of view, measurement process is fundamental: measurement trueness and precision are fundamental factors for process control and process adjustment. As a matter of fact, quality, maintenance and production planning strongly interact and jointly determine those aspects of a company's success that are related to production quality, i.e. the company's ability to timely deliver the desired quantities of products that are conforming to the customer expectations, while keeping resource utilization to a minimum level (Colledani et al. 2014). Moreover, there is another fundamental aspect releated to the metrology in production, not strictly related to the product itself, but to the control process in terms of machine tool enhancement. Compensation of systematic geometrical errors is an extremely important and widespread application of metrology in manufacturing. Without this kind of embedded metrology, machine tools would be considerably more expensive, which provides another evidence of the productivity benefits of metrology in manufacturing (Savio et al. 2016). The general development of manufacturing technology

is directed towards better quality of products and a higher productivity. These objectives are achieved by optimizing the entire production system, whereby optimizing means to realize the technical requirements with the most economic means. (Schwenke et al. 2002). Therefore, measurements are done to determine specified quantities or functional process-parameters in numbers and units. These measuring results are content of information, which is transferred to some person or programmed information processing system for comparison with quantitative figures expected, set, or known by other experiments. Acquisition of knowledge is the target of a measurement and information transfer for being able to derive consequences from this knowledge for developing the know–how and finally the wisdom for managing improvements of manufacturing processes and products. "Productive metrology" (Kunzmann et al. 2005) as the field of knowledge concerned with measurement to gain information and subsequently knowledge to change something or somebody, either by becoming grounds for actions, or by making an individual (or an institution) capable of different or more effective actions. Therefore, in a changing production environment with permanently growing demands on quality, flexibility and speed, traditional metrology is no more suitable and competitive. Mechanical systems are not flexible enough, moreover not fast enough for the actual production requirements. Optical methods often can acquire more data in less time (e.g. CMM versus fringe projection) and without touching the part. These characteristics qualify optical methods especially for in-process measurement. Moreover optical and non-contact measurements find a fundamental application also in the field of surface characterization, considering that surface topography is playing a fundamental role in manufacturing (Hocken et al. 2005). Surface phenomena play a decisive role in the behaviour of engineering parts; their understanding and control are fundamental to the development of many advanced fields (Bruzzone et al. 2008).

Thank to the publication of (Schwenke et al. 2002) is possible to shortly synthetize the story of optical measuring systems, starting from the origins. From its early beginnings dimensional metrology was closely related to the use of light for measurement. An early example is the so-called 'Jacob Bar', system used for taking optical bearings in the fields of civil engineering and navigation. A really simple system based on the intercept theorem able to determine either the distance from an object (if its lateral dimension is known) or its dimension (if the distance is known). Really important milestones in the application of optics for dimensional measurement are: the invention of the microscope (Hans and

Zacharias 1590), the utilization of light interference (Michelson 1892) and the development of gas lasers (Maiman 1960). Later, the rapid growth of computational power and the wide application of opto-electronic components for consumer products increased the speed of development of optical metrology (Schwenke et al. 2002).

Thanks to the growth of computational power, not only the speed was increased, but also the accuracy and the technologies. Real time corrections, data processing and data management are available and applicable in in-line systems mainly thanks to the reduction of computational time. Finally, X-ray computed tomography, technology that becomes an increasingly promising tool for dimensional metrology, is a clear example of the importance of computational power in measuring systems.

This work is focused on three different technologies: confocal microscopy, video probe CMM system and finally X-ray computed tomography, presenting four different examples of measuring system enhancement through numerical correction methods and simulations.

Confocal optical microscopy has several advantages over conventional optical microscopes. Thank to this technology is possible to generate three-dimensional images of objects by means of optical sectioning. It allows profiling of surfaces, 3D objects and multi-layer structures. Confocal microscopy is also capable of generating high resolution digitised data sets for the 3D objects that can be stored and are suitable for subsequent image processing (Schwenke et al. 2002; Leach 2011). This technology is suitable for surface characterization but also for controlling micro-machining process (Fang et al. 2017). Some limitations are caused by the optical nature of this technology, one of these, connected to the slope of the surface is studied in this work, enhancing the accuracy of the surface parameters through a numerical model. These limitations are also used for enlarging the measurement capabilities of this instrument.

Correction method were also developed for video sensors applied in threads characterizations. Also in this case the limitations of the instrument are treated numerically in order to enlarge the measurement capabilities. A video probe combines an optoelectronic camera with microscope optics and appropriate illumination. On technical surfaces, especially the interaction between illumination and workpiece surface influences the measurement quality. Although image processing has significantly improved over the last few years, optical edge detection on real product surfaces generally

has not yet reached the accuracy and reliability of mechanical probing (Schwenke et al. 2002). In particular, in the case of threads it is clear the benefit of the optical systems (mainly for speed and in-line application), neverthless geometry of the sample under investigation is not compatible with the measuring principle. Apply these kind of fast and flexible systems also in this field is possible only after development of a correction method.

Finally Computed tomography, far primarily used for medical diagnostics is now largely used for dimensional metrology, thanks to capability to measure both internal and external features. The object to be scanned is located on a rotary table. As the X-rays propagate through the workpiece material, the X-rays are attenuated due to absorption or scattering. The amount of attenuation is determined by the length traveled in the absorbing material, by the material composition and its density and by the energy of the X-rays. The attenuation is captured by an X-ray detector, resulting in a 2D grey image. Thanks to the rotary table, images are taken from different angular positions of the workpiece. All these projected images are then reconstructed through mathematical model, creating the 3D voxel model of the sample (Kruth et al. 2011). The voxel is the 3D analogue of a pixel, and the gray value of it is proportional to the absorptivity of the material. The next steps concern the post-processing of the voxel data, including the detection of the workpiece edges (segmentation) and subsequent dimensional measurement and quality control. *CT can be considered as a third revolutionary development in coordinate metrology, following the introduction of tactile 3D coordinate measuring machines (CMMs) in the seventies and that of optical 3D scanners in the eighties* (De Chiffre et al. 2014). The power of this new technology is fighting with the limitations. A lot of different quantities not completely mapped and still understood are influencing the measurement uncertainty. The relative distances of source, object and detector, the geometry of the object, the lateral resolution of the detector, the geometrical deviation of the mechanical axes, X-ray source spectrum, beam hardening, object composition (material, roughness) and the detector properties are just an example of some possible sources. Increasing the accuracy of the system means try to understand these sources, map them and eventually correct them (if systematic). Roughness of the sample is analysed and the effect on the final dimensional measurement is mapped. Through a numerical analysis was understood the effect and proposed a correction model.

Optical systems are clearly suitable and perfectly compatible with the requirements of manufacturing system. Research should try to enlarge the capabilities of the existing technologies in order to extend the applicability and ensure a constant increase of metrology culture in production contests. Four different models for enhancement of optical systems are presented in the next chapters: accuracy and capabilities are increased through numerical methods.

2. Enhancing optical surface characterization through void pixels control

This chapter is focused on the effect of the presence of void pixels on surface topography. Void pixels are points of the topography that are not measured by the optical system, so pixels with no-information. The presence of void pixels influences the computation of surface roughness parameters, causing a variability of these parameters. Void pixels could be ignored in the computation, considering them as holes in the topography, or they could be reconstructed through interpolation of the missing values using the neighbours' information. Variability associated with the different choices is analysed and quantified in this chapter, using sensitivity analysis on real and numerically generated surfaces. Final considerations and relations are based on a total amount of more than 2'000'000 simulations. Findings highlight the need of reconstruction in order to minimize the variability of the parameters and ensure an enhancement of the optical measuring process.

Introduction

In optical metrology, many problems are related to the difficulties of the instrument in catching surface morphology. Reflections, dust, noise and steepness of the surface influence the quality of the obtained topography. In particular when analysing surfaces for surface parameters calculation, these problems could influence the result of the measuring process. The instrument indexes as void pixels (pixels that are not directly measured and for this indexed with really high values or not a number values) all points that reflect the light outside the objective or points that generate spikes. Missing measurement values are generated when the probe does not receive sufficient information to compute height for a specific pixel (Leach 2011; Lonardo & Bruzzone 2000). These points are handled in different ways, commercial software allows the user to interpolate the void pixels in order to obtain continuous surfaces or exclude them from the parameters evaluation. Voids are not as easily handled in range/intensity images, where a validity mask is required, i.e. a binary image maintained in parallel to the original image to keep track of invalid pixels. Biggest problem related to the masked images, is correlated with the processing algorithms. These algorithms (e.g. convolution, fast Fourier transform, etc.) are not adapted to deal with such data. Generally, because of the limitations induced

by the mask, most common software are replacing these voids with a reference value. This procedure is called padding. Padding introduces a source of error but generally this error is small when the analysis is carried out over a large image (Leach 2011). Some investigators prefers to tend to fill the unmeasured points for obtain a complete surface, some others leave them as unmeasured, for not introducing additional errors (MacAulay 2015). Some potential solutions to reduce the number of unmeasured points were studied and described in the past (Blateyron 2011). Linear and non-linear interpolation of valid neighbours (Senin, L. A. Blunt, et al. 2012; Senin, L. Blunt, et al. 2012) or interpolation via median operator on moving windows seems to be the most promising solution. A deep study of median operator was done in image processing literature (Gonzalez & Woods 2008). Outliers and artefacts identification also causes the generation of void pixels on the topography. Also in this field different identification methods were studied (Wang & Feng 2014; Ismail et al. 2010), trying to overcome the limitations of ISO recommended filters (ISO16610-60:2015; ISO16610-30:2015). Moreover, particular techniques to increase the maximum detectable slope were also developed (Marinello et al. 2007), trying to reduce the void pixels caused by the slope of the surface. However, generally a small number of void pixels is still present and not reducible because of the nature of the surface. In these cases the presence of void pixels in the scale limited surface influences the evaluation of surface parameters, which can be evaluated either on the reconstructed surface (in which the void pixels are replaced using interpolation algorithms) or, on not-reconstructed datasets (in which the void pixels are not considered for parameters evaluation). In both cases, as previously said, introduced uncertainty and variability should be stated, but no publications that try to quantify the effect of the choice are currently available.

This work started from a preliminary evaluation of the effect of void pixels on some real samples (Medeossi et al. 2016), in order to quantify the effect of the presence of void pixels and moreover to quantify the variability of parameters evaluated on reconstructed surfaces and rough surfaces (not-reconstructed). After preliminary evaluation the study was extended to a large number of surfaces. In order to do this, a numerically surface generator was used: thousands different periodic surfaces were analysed and different distribution of void pixel were analysed. At the end, the generalization permits a general view of the effect and the creation of tables in which the variability of surface parameters is expressed in function of the void percentage. The final goal of this work was to

highlight the effect of the reconstruction on surface parameters evaluation. The analysed cases presents percentage of void pixels lower than 7%, in order to correlate the effect of the measurement in the case of high quality measurements. It is demonstrated that reconstruction of surface topography ensures a lower variability of surface parameters. Generally, it causes a drift of the values, but the obtained variability (evaluated in terms of standard deviation of the entire batch of surfaces analysed) is smaller. The work will propose an evaluation of this variability, different quantification were done for different areal parameters. The study was limited to the periodic surfaces because of the complexity in the generalization of the approach and because of the particular interest on these kind of surfaces.

Materials and methods

The most important output of this work was the quantification of the sensitivity of surface roughness parameters to the presence of void pixels. As described in the introduction, the void pixels are caused mainly by physical limitations of the optical instruments or by the presence of particular points that are not completely measured. These different effects generate holes in the acquired height map. This loss of information of some pixel influences the evaluation of the surface parameters. Some of the typical parameters used during surface characterization are the average mean height (called *Sa*), the skewness of the surface (*Ssk*) and Kurtosis (*Sku*). These three parameters were selected for this study because of their largely diffused use in surface characterization, moreover because of their sensitivity to the slope of the surface and to the presence of peaks and valleys. ISO standard (ISO25178-2:2012) defines the parameters as follow:

$$Sa = \frac{1}{A}\iint_A |z(x,y)|\,dx\,dy$$

$$Sq = \sqrt{\frac{1}{A}\iint_A z^2\,(x,y)\,dx\,dy}$$

$$Ssk = \frac{1}{{S_q}^3}\left[\frac{1}{A}\iint_A z^3(x,y)\,dx\,dy\right]$$

$$Sku = \frac{1}{{S_q}^4}\left[\frac{1}{A}\iint_A z^4(x,y)\,dx\,dy\right]$$

The presence of void pixels causes discontinuities in the function that represent the surface topography. These discontinuities are solved thank to the discretize nature of the measured topography. Measured points are organized in a sorted matrix (an height map), so the integrals are discretized and computed using summarization. This means that the presence of void pixels is not causing discontinuities and limitations in the numerical evaluation of the parameters. Moreover, as extensively described in the previous chapter, is possible to substitute the void pixels with a value obtained from the interpolation of the neighbour pixels or eventually through different padding methods. The interpolated values are clearly not directly measured. The calculation creates a point with a hypothetic height: this calculation introduces an information that is not completely reliable. In this way, this process introduces an additional source of uncertainty to all the subsequent calculation steps. Nevertheless, also a complete loss of information from the void pixels can produce a variability in the computation methods, because of the weight of those points during the parameters computation. Therefore, the focus of this work is to understand how the two different approaches are influencing the final surface parameter and how the different parameters are influenced by the presence of the voids.

The only way to understand completely this effect is comparing void-affected topography parameters to reference ones. In order to do that, the analysis was developed through a numerical simulation of void pixels generation. This void generation process was applied both on real surfaces in a preliminary study and then to a batch of numerical generated surfaces.

As previously said, the void pixels are linked to noise, artefacts, reflection and physical limitations. Noise, artefacts and reflection are randomly distributed on the surface and their position is not strictly linked to the morphology of the surface. On the contrary, the physical limitations are mainly connected with the slope of the measured surface. So, void pixels were created following two different procedures: a completely random distribution linked to the presence of noise, dust etc. and a tilt distribution linked to the numerical aperture of the objective (physical limitations). The results obtained in the two different cases are completely different and influences the parameters following different rules and trends. The overall procedure followed for the study on the real surfaces is shortly described in Figure 1.

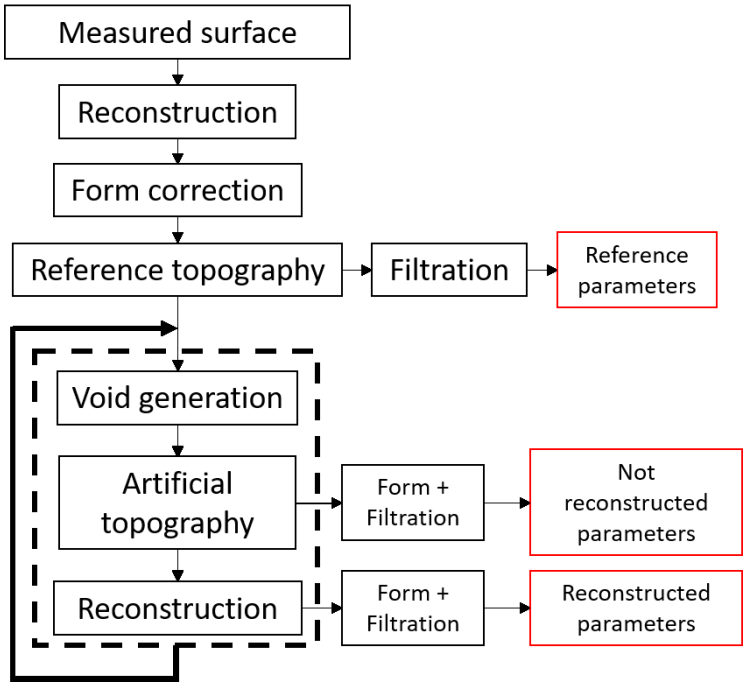

Figure 1 Diagram of the simulation procedure for real surfaces

The surfaces are measured using a state of the art 3D optical profiler (SENSOFAR Plu Neox), operating in confocal mode with blue light (λ_{blue} = 460 nm). For the measurements was selected a Nikon CFI-LU-EPI-P objective with 20x magnification. The surfaces were accurately measured in order to ensure a percentage of void pixels lower than 0.05%. The small amount of void pixels are reconstructed through a polynomial interpolation, using a 3rd degree equation. The window used for the interpolation is 10x10 pixels, moved on the acquired topography and centred on each void pixel. Then the void pixels are substituted with the interpolated value.

According to ISO standards, the reference topography and then the reference parameters were obtained from the measured surface after reconstruction, form correction and filtration. The reference topography is used as input for the sensitivity analysis.

Void pixels are generated with two different methods (described in the subsequent sections) and a total amount of 25'000 different void distribution are analysed. For each distribution, surface is managed and processed following two different procedures. Firstly, surface parameters are calculated directly on the rough surface, characterized by the presence of voids in the topography. In this case, implementing the formulations for surface roughness parameters calculation provided by SPIP User's manual, the summarization that discretizes the integrals are not influenced by "holes" in the height map. After the calculation of the parameters on the not-reconstructed surface, the void

pixels are substituted using an interpolation criterion. A simply linear interpolation was applied, considering the effect of a square window of 10x10 pixels. Linear interpolation ensures a good cycle time, 3 times smaller than the 3rd degree polynomial. The not-a-number values that represent void pixels, were finally replaced with the calculated values. The obtained complete topography was used for surface roughness parameters calculation. All the steps will be analysed in the subsequent paragraphs, focusing on the methods used for void generation. Finally, all the calculated parameters were compared and analysed.

In order to generalize the results obtained from the real measurement (real measurements represent only some particular cases of combined parameters) was decided to create the surfaces numerically. In this case a generalization for the periodic surfaces could be done. A large number of periodic surfaces with largely distributed parameters were simulated and analysed. The overall process is shortly presented in Figure 2. In this case, the preliminary reconstruction is not necessary: the numerical generation of the surface ensured a perfect height map with no voids. Moreover, the filtration steps are not used in this phase of the work. Through the generation algorithm, only surface roughness is simulated, no form error or waviness are introduced on the surface.

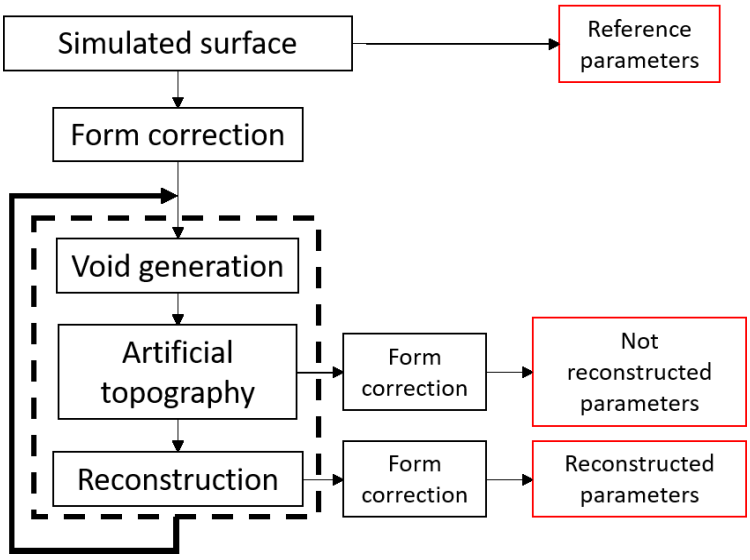

Figure 2 Diagram of the simulation procedure for simulated surfaces

Surface generation, algorithm used and parameters fixed for the generation will be analysed in a dedicated paragraph.

Random based void creation

Void pixels are created in order to simulate the random distribution caused by dust, small and localized reflections and outliers. In this case, the distribution of the void pixels is perfectly random, with no relation with the characteristics of the surface. In order to develop a distribution that follows these characteristics, the pseudorandom numbers generation was used. A random matrix characterized by values in between 1 and 100 was generated. The dimensions of the matrix are the same of the height map. The distribution of the points was based on a Gaussian distribution. The entire process developed for the random generation is shortly presented in Figure 3. A variable threshold was used for the determination of the void pixels. The threshold identifies the limit above which the values of the matrix should be replaced with a *not-a-number (Nan)* value. In this way was possible to create a mask: all the points not characterized by *Nan* value were replaced with a zero value. So only zero and Nan characterize the mask: a simple sum to the height map generates a surface with some distributed void pixels. The threshold was used in the iterative process for varying the percentage of void pixels. The pseudorandom distribution of points in the matrix (different distributions are developed for each threshold) ensures a variable distribution of void pixels. The position of the void pixels is not associated with the morphology of the surface. The void mask matrices are randomly generated for every surface and for every different threshold. The matrices are not stored in order to exclude every systematic error or particular effect caused by use of the same void pixels position.

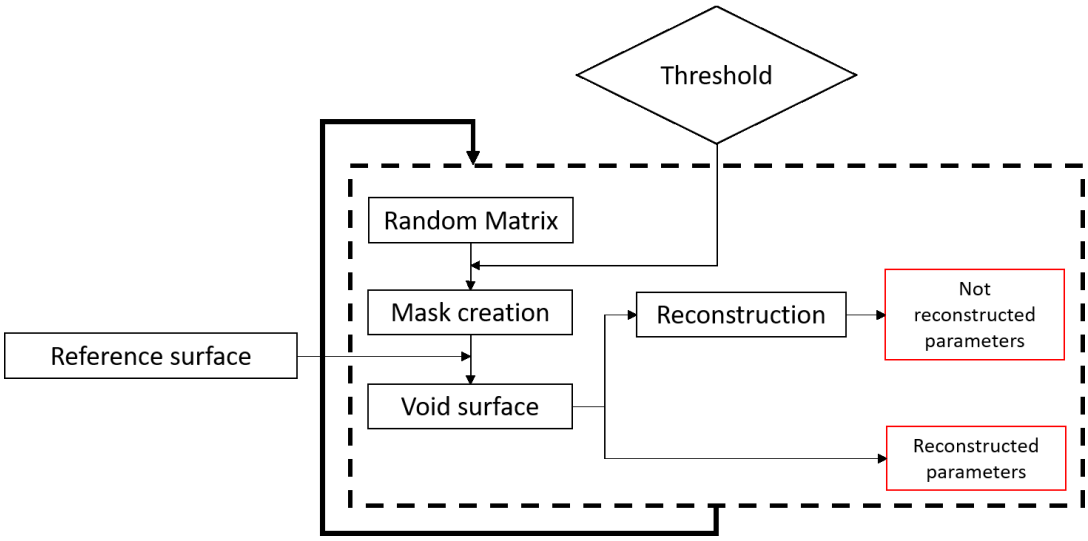

Figure 3 Diagram of the random based void generation

Changing the threshold value is possible to obtain different percentage of void pixels. The threshold is moved from 93 to 99.9 with steps of 0.3. In order to provide an

example of the obtained surface, a 7% void distribution surface is shown in Figure 4. All the white holes in figure are the not-a-number values, which simulates the presence of void pixels.

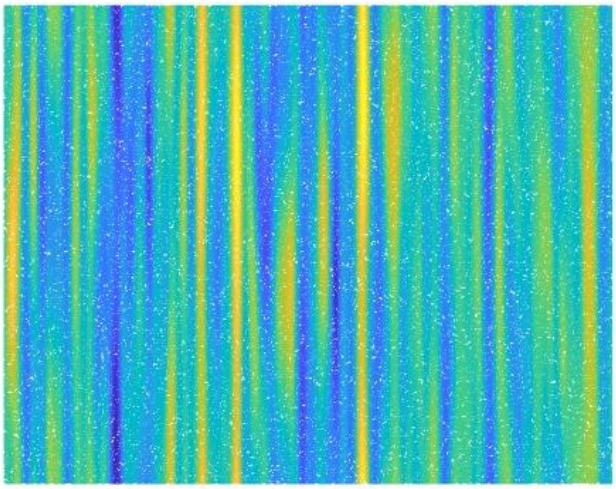

Figure 4 Example of a 7% void pixels distribution

Slope based void creation

In this case, the void pixels are created through the simulation of the tilting process of the surface. The numerical aperture of the objective influences the capabilities of the instrument to measure steep surfaces. Moreover, the tilting of the sample could influence the position of the voids associated with the slopes. Increasing or decreasing the angle between the steep surfaces and the optical axis could change the final topography. In order to simulate this effect, the surfaces are rotated through the y-axis. The absolute system of reference is based on the optical axis (defined as O_0), *z-axis* parallel to the optical axis and the *x-axis* and *y-axis* aligned in order to complete a right hand system of reference. Another system of reference could be placed perfectly aligned with the previous one in the initial state, then, this system is changing the orientation because of the rotation of the topography. This different system is called O_1. In a preliminary phase, the rotation was developed through the creation of the rotation matrices. The height map was treated as a sorted *x-y-z* point cloud, in order to apply the transformation. The transformation matrix was constructed starting from the rotation angle. In this way, changing the simulated rotation angle was possible to simulate the rotation of the points and consequently the rotation of the steep surfaces.

$$\begin{Bmatrix} x' \\ y' \\ z' \end{Bmatrix} = [T]_0^1 \begin{Bmatrix} x \\ y \\ z \end{Bmatrix}$$

In this way is possible to simulate rotations around *x* and *y-axis*, changing the steepness of the surface. After the rotation was calculated the gradient of the surface, gradient both in x and y direction. At this point, in order to simulate the limitation of the optical system, was applied a threshold on the numerical value of the gradient. All the points exceeding the numerical gradient corresponding to a surface steeper than the limit of the objective (e.g. 21° for the 20x magnification) are indexed as *Nan*. After the void generation process is necessary to develop again the form removal, fit a plane to the point and remove the form from the point cloud. Moreover, at the end of this process, is also necessary to interpolate the existent data in order to go back to a sorted matrix. All these steps are time consuming (in particular the interpolation of a new equi-spaced and sorted grid of data) and not compatible with the number of cycles that we want to simulate.

In order to overcome this limitation and not considering a removal of the form based only on z translations a different approach was developed. The rotations that are influencing the detected surfaces, in the case of periodic surfaces, are the ones around an axis parallel to the machining path (in this case the axis that is every time parallel to the machining axis is the *y-axis*). For example in the case of a turned workpiece, the machining process would create a path orthogonal to the rotation axis; in order to rotate the flanks is necessary to rotate around an axis orthogonal to the rotation axis too. As we previously said, after the rotation the gradient is used for the evaluation of the steepness of the surface. Changing the optical axis inclination could be simulated through an offset on the gradient matrix. Fixing the rotation of the optical axis is equal to rotate the surface. From a numerical point of view, this rotation is equivalent to a rotation of the surface. The gradient of the surface calculated on the reference plane, with the *z-axis* orthogonal to the surface should be offset. The quantity of the offset is equal to the tangent of the rotation angle of the optical axis. This procedure limits the possible rotations only around y-axis, but this limitation is necessary for the generalization of the analysis.

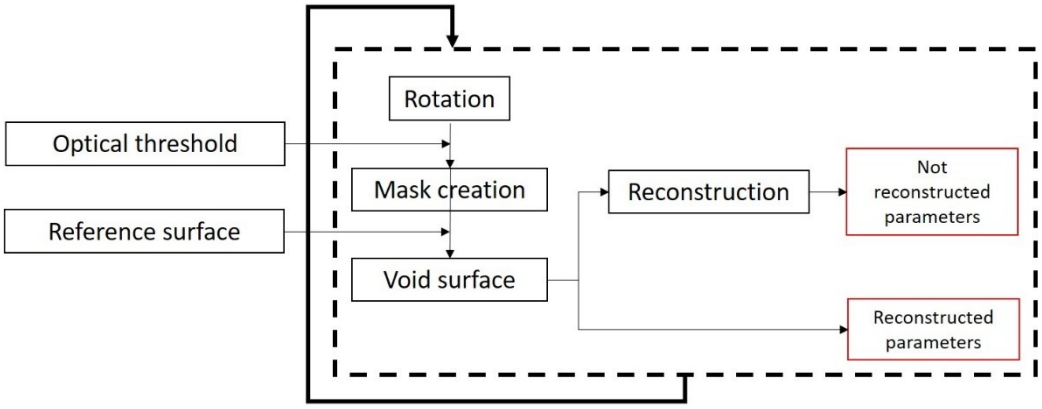

Figure 5 Diagram of the slope based void generation

In this case, the threshold is fixed (according to the limitation of the optical instrument) and applied to the modified gradient matrix. All the values that exceeds the threshold are indexed as *Nan*. All the others are indexed as zero. Using the same procedure developed for the random distribution, the mask is directly summarized to the original matrix and a new void distribution is analysed. Figure 5 presents the iterative process developed for void generation changing the slope of surfaces. Every surface is rotated using a random distribution of angles in between +5 and -5 degrees around the zero position. 230 different rotations are developed, and each time the obtained void mask is applied to the reference surface. The so-called not-reconstructed parameters are calculated on the void surface. Then, after the linear interpolation of the voids, the so-called reconstructed parameters are evaluated and stored for each orientation and for each reference surface. Figure 6 shows an example of a surface obtained through the slope based method. This surface presents a percentage of void pixels equal to the surface shown in Figure 4 and equal to 7%.

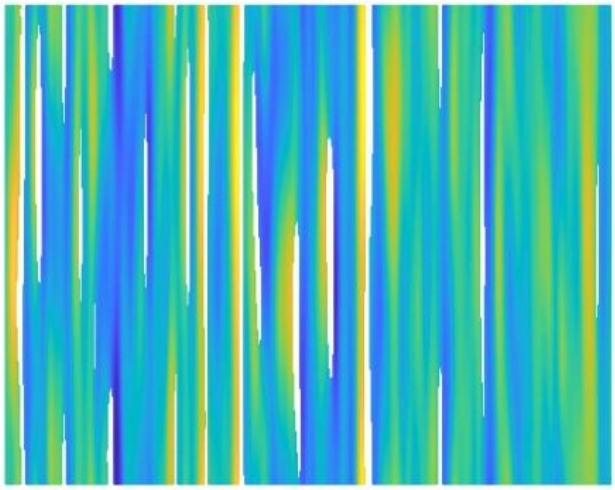

Figure 6 Example of a 7% void pixels distribution obtained through slope based method

Measured surface

The preliminary study was developed on 6 different turned surfaces. The real surfaces were used to identify first correlation and deviation of the parameters, and for a subsequently verification of the numerical simulation. The parameters that characterize the analysed surfaces are reported in Table 1.

Parameter	Surface 1	Surface 2	Surface 3	Surface 4	Surface 5	Surface 6
Sa	1.354	1.359	1.518	1.519	3.131	3.142
Ssk	-0.439	-0.449	-0.259	-0.263	0.482	0.489
Sku	2.831	2.827	2.316	2.313	2.245	2.242

Table 1 Parameters of the measured surfaces

All the six different measured surfaces were obtained through external turning. Figure 7 shows an example of the measured surface. In this particular case surface number 1, after filtration and form removal stages is shown. Gaussian filter with a standard nesting index was applied. A polynomial fitting was applied for the form correction, in order to remove the cylindrical form of the turned sample.

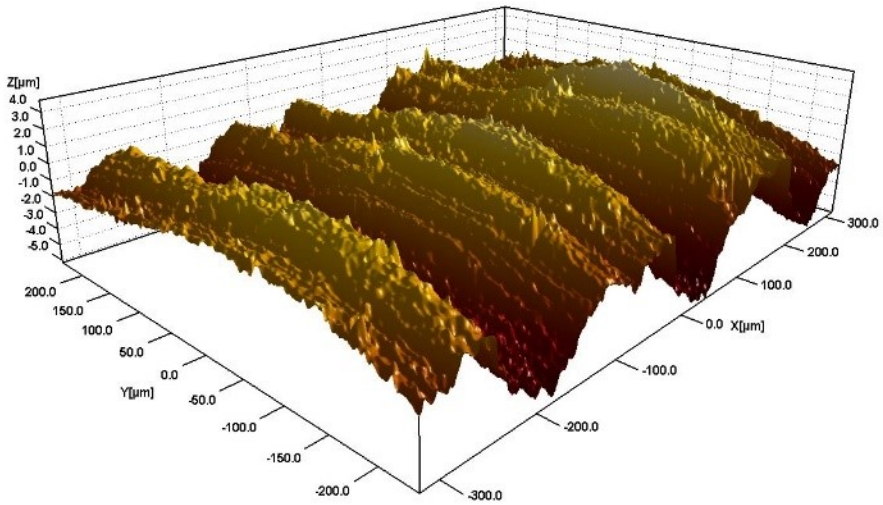

Figure 7 Example of a measured surface, before the sensitivity analysis

The surfaces obtained from the measurement are then used as input for the sensitivity analysis. In this case, the simulation of the void pixels was developed as follow: 230 different distributions for the random algorithm and 200 different for the slope based distribution. The total amount of analysed surfaces is equal to 2580 surfaces. The results are divided in classes based on the percentage of void pixels. The results are presented in the next section considering the mean value and the standard deviation of the classes, for all the different surfaces.

Numerical surface generation

Random rough surfaces with Gaussian statistics are generated using a method outlined by Garcia and Stoll: uncorrelated distribution of surface points using a pseudorandom number generator is convolved with a Gaussian filter to achieve correlation. Random rough surface are created through the developed algorithm (Bergstrom 2008). Two-dimensional (isotropic and non-isotropic) square surfaces with Gaussian height distribution function and Gaussian auto covariance function are numerically generated. The input necessary for the creation of the surface are: the number of surface points, the length of the surface side, the correlation length along the two axis. Through the changing of the root mean square height value and the autocorrelation length is possible to generate different surfaces with variable surface parameters. This means that the generated surfaces are characterized by different steep surfaces and morphology. As described in Figure 8, for each value of the root mean square height, the autocorrelation function is looped. For combination of values, because of the stochastically height distribution, different surfaces are created. The mean square height was varied in between 0.5 and 5 um, and the autocorrelation length on the x direction between 5 and 20 (x is decided to be orthogonal to the machining tracks). In order to ensure a turned profile, y autocorrelation length is fixed constant and equal to 200. For every couple of parameters 100 surfaces were created. At the end, 4500 different surfaces were stored and analysed.

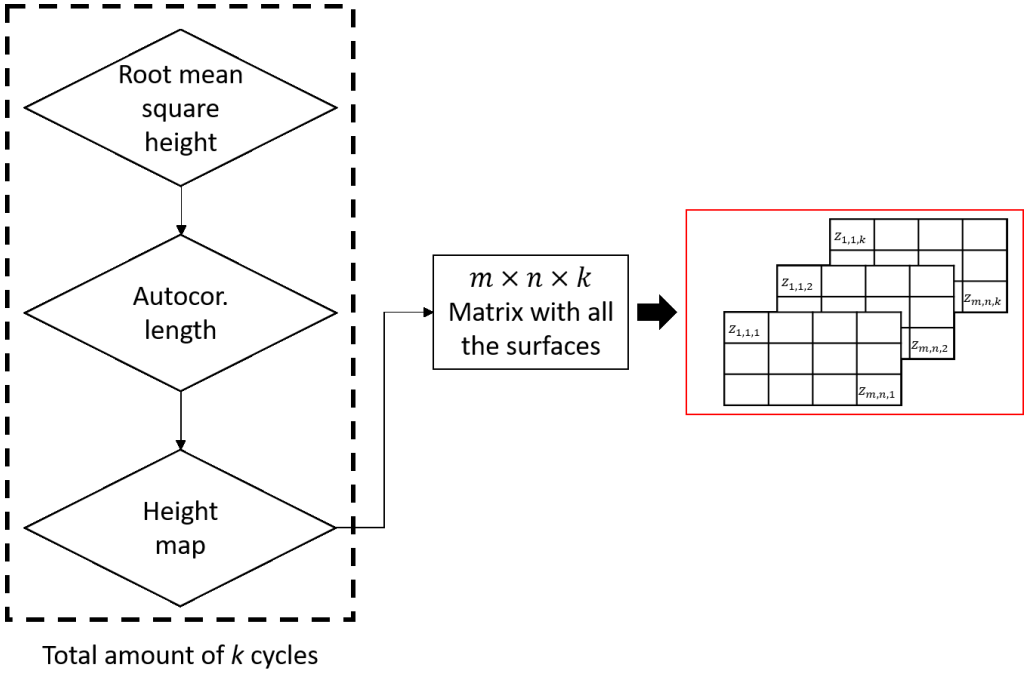

Figure 8 Scheme of the surface generation procedure

The most important aspect of the generation loop is ensuring a distribution of *Ssk* and *Sku* for each *Sa* group. This is necessary in order to understand the sensitivity of the other parameters to the void presence and to isolate the effect of void on different parameters.

As shown in Figure 8, all the obtained surfaces are stored in a matrix and subsequently imported for void generation. The dimension of the topography is fixed to 476x476 pixels. The dimension of the surface was imposed by the storage availability and computational time required for subsequent steps. The resolution in x and y was fixed equal to the optical measurement, 0.83 µm. Figure 9 and Figure 10 show an example of two different simulated surfaces.

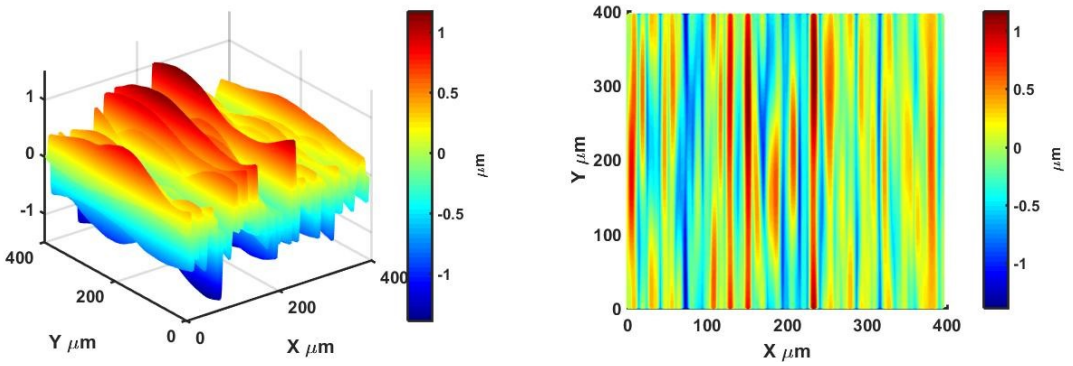

Figure 9 Example of simulated surface with Sa=0.323 μm: on the left 3D view, on the right top view of the surface

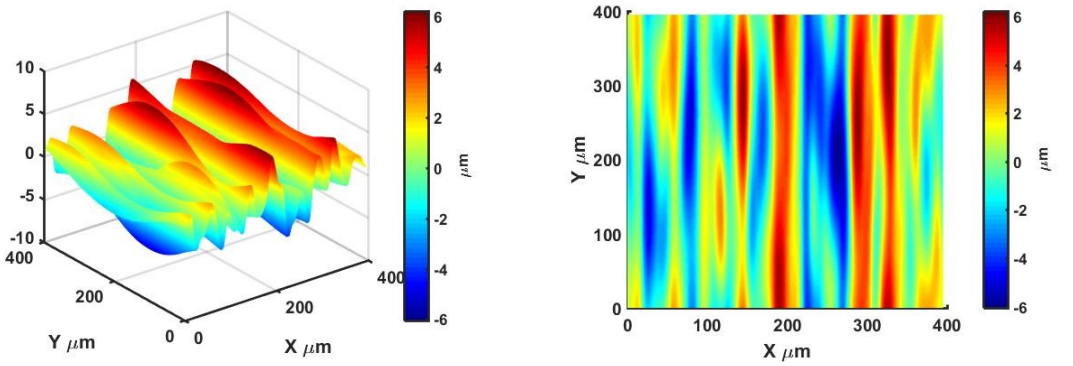

Figure 10 Esample of simulated surface with Sa=2.073 μm: on the left 3D view, on the right top view of the surface

The parameters that characterize the two surfaces shown in the previous figures are reported in Table 2.

Surface	Sa	Sz	Sq	Ssk	Sku
1	0.3283	2.5609	0.4097	0.109	2.9299
2	2.0734	12.2756	2.5463	0.0231	2.4260

Table 2 Surface roughness parameters of the presented topographies

The *Sa* and *Sq* parameter distribution histogram on all the simulated surfaces is reported in Figure 11. As it is clearly demonstrated, the surfaces simulated are mainly distributed in between 0.3 and 2.5 μm. In Figure 11 is reported the distribution of the *Sq* parameter, considering 10 different classes. In this case, the values are equally distributed, except for the last two classes. *Sz* parameter was not taken in great consideration, but for a complete understand of the distribution of the surfaces, was reported in Figure 12. As clearly described, the analysed surfaces are spread all over the values from small *Sz* (some hundreds of nanometers) to 20 μm.

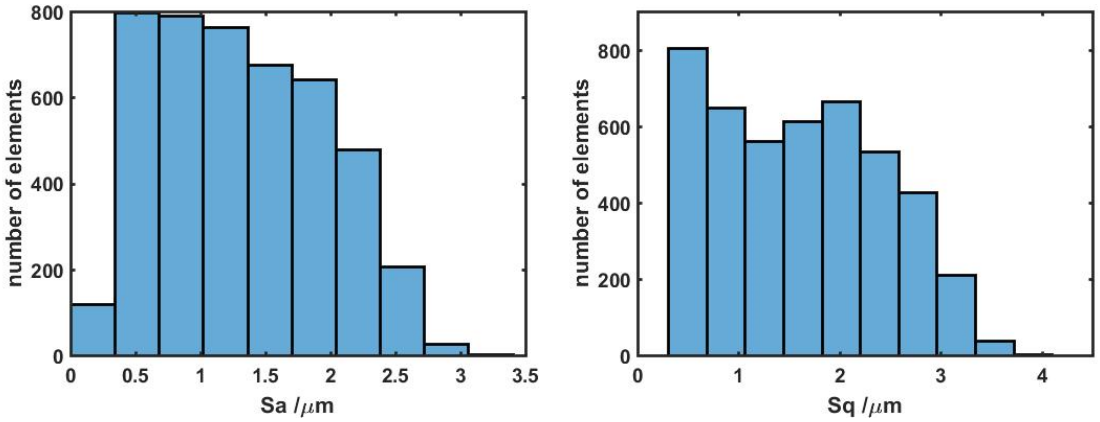

Figure 11 Distribution of Sa and Sq parameters

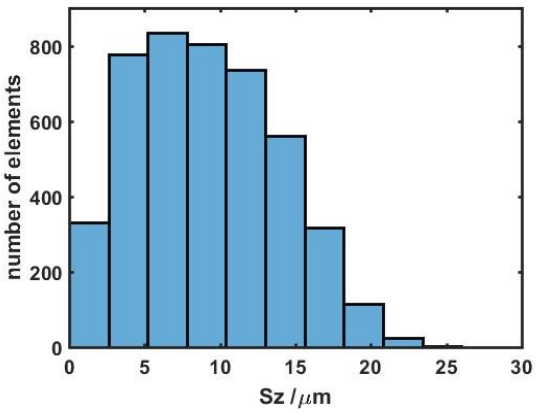

Figure 12 Distribution of Sz parameter

Skewness and Kurtosis are shown in Figure 13. Kurtosis is centred on 3, and most of the surfaces are in between 2.1 and 3.7. Same considerations for Skewness, centred on 0 and mainly between -0.5 and 0.5. These two parameters are influenced by the Gaussian nature of the simulated surfaces.

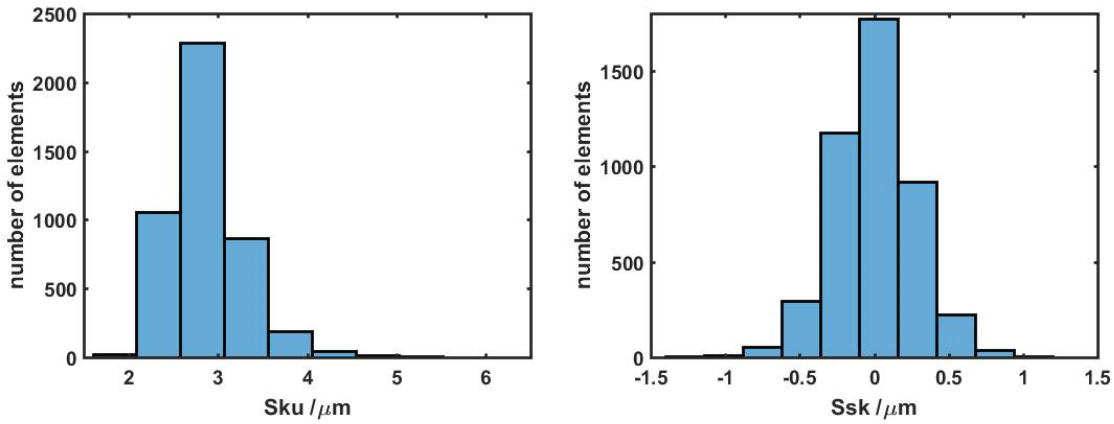

Figure 13 Sku and Ssk parameter distribution

In order to find a relation between the effect of void pixels and parameters was also checked that inside each class (different classes based on *Sa* parameter) contain the entire spread of other parameters. The surfaces were divided in 10 classes, as previously said, but the first and the last one were not consider (because of the low frequency of the class). The classes were divided according to the class limits presented in Table 3.

Class:	**1**	**2**	**3**	**4**	**5**	**6**	**7**	**8**
Class limits (Sa)	0.34-0.68	0.68-1.02	1.02-1.36	1.36-1.7	1.7-2.04	2.04-2.38	2.38-2.72	2.72-3.06
Class marks (Sa)	0.51	0.85	1.19	1.53	1.87	2.21	2.55	2.89

Table 3 Class limits and class marks respect to the Sa value used for class division

In the next figures, Figure 14, Figure 15, Figure 16, Figure 17, Figure 18, Figure 19, Figure 20 and Figure 21 the distribution of the Sku and Ssk parameters inside the different classes is presented. These figures are shown in order to highlight the distribution of these parameters inside each Sa class. In this way was possible to study the effect of each single parameter in each single different class. 8 different classes were studied and presented.

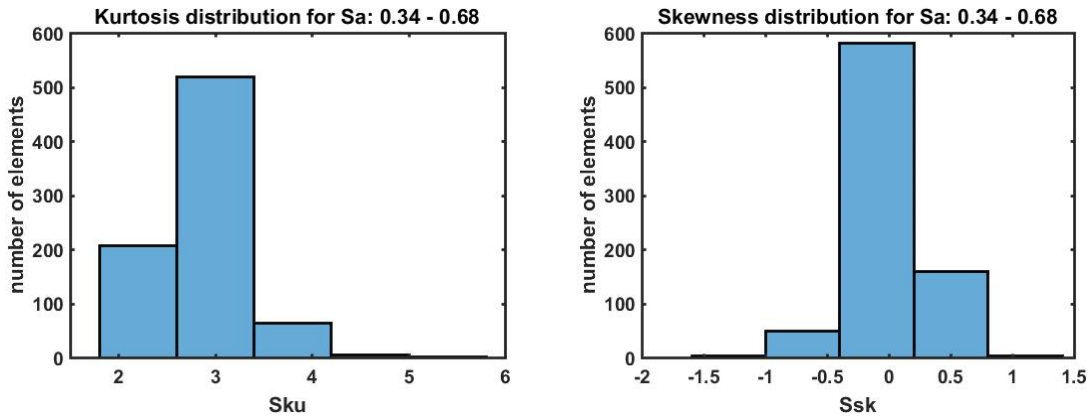

Figure 14 Distribution of *Ssk* and *Sku* parameters in for *Sa* in between 0.34 and 0.68 μm

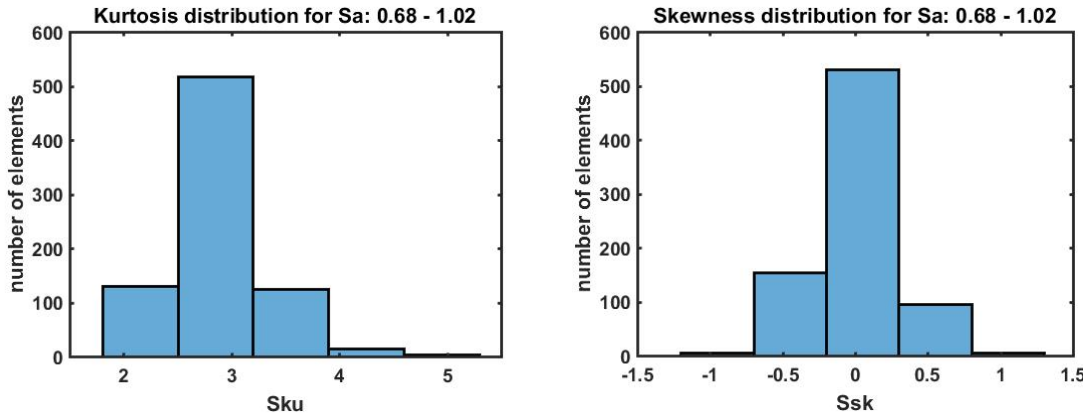

Figure 15 Distribution of Ssk and Sku parameters in for Sa in between 0.68 and 1.08 µm

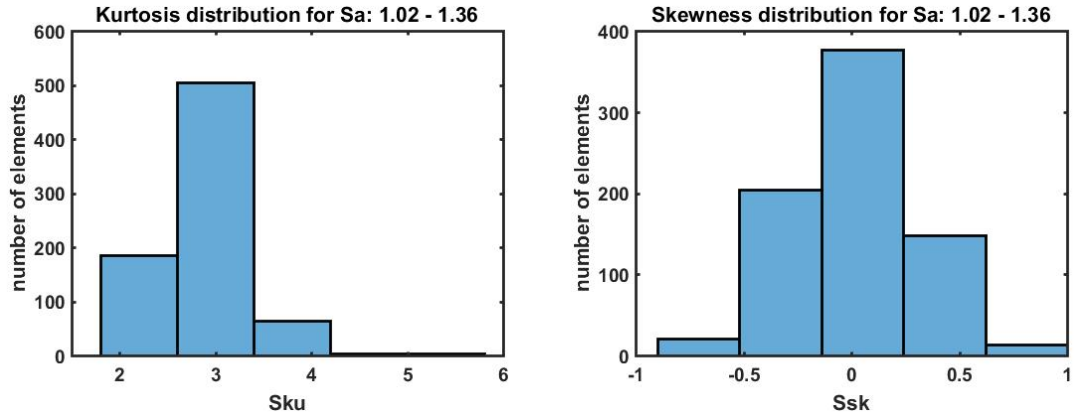

Figure 16 Distribution of Ssk and Sku parameters in for Sa in between 1.02 and 1.36 µm

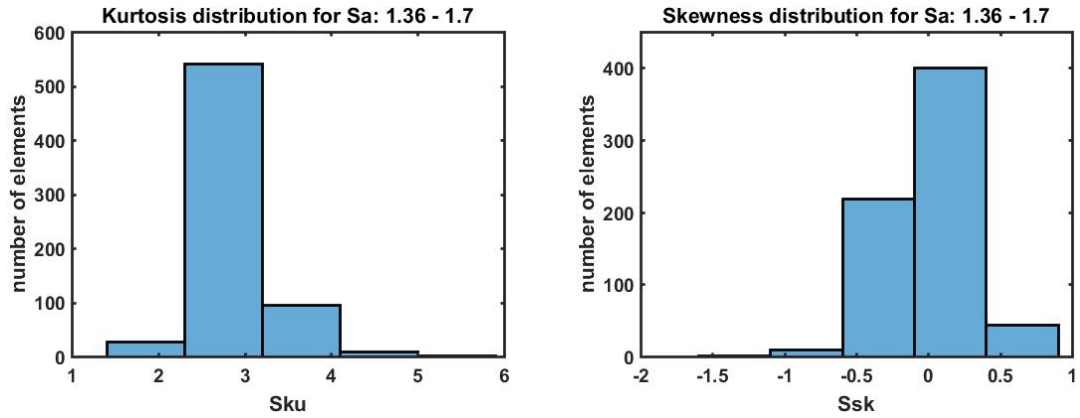

Figure 17 Distribution of Ssk and Sku parameters in for Sa in between 1.36 and 1.7 µm

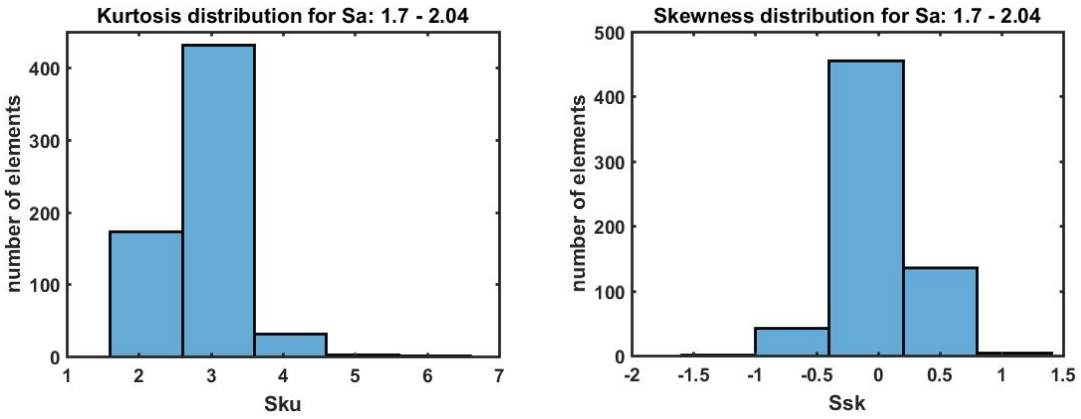

Figure 18 Distribution of Ssk and Sku parameters in for Sa in between 1.7 and 2.04 μm

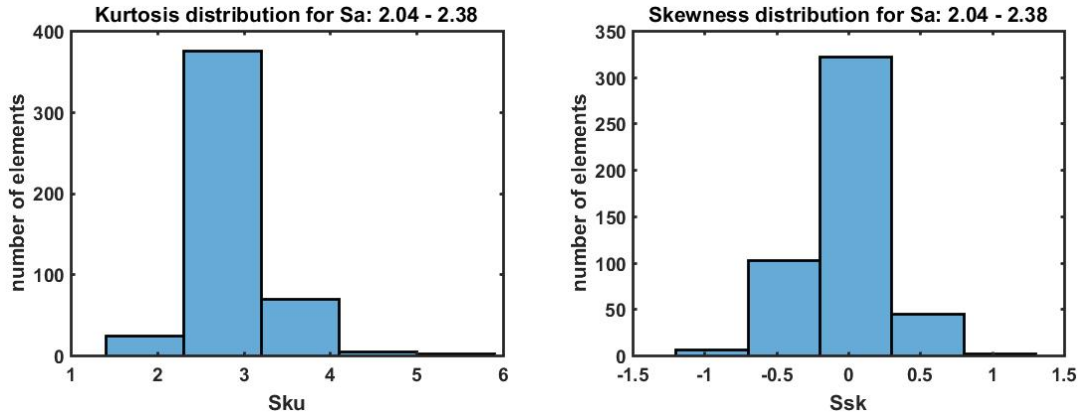

Figure 19 Distribution of Ssk and Sku parameters in for Sa in between 2.04 and 2.38 μm

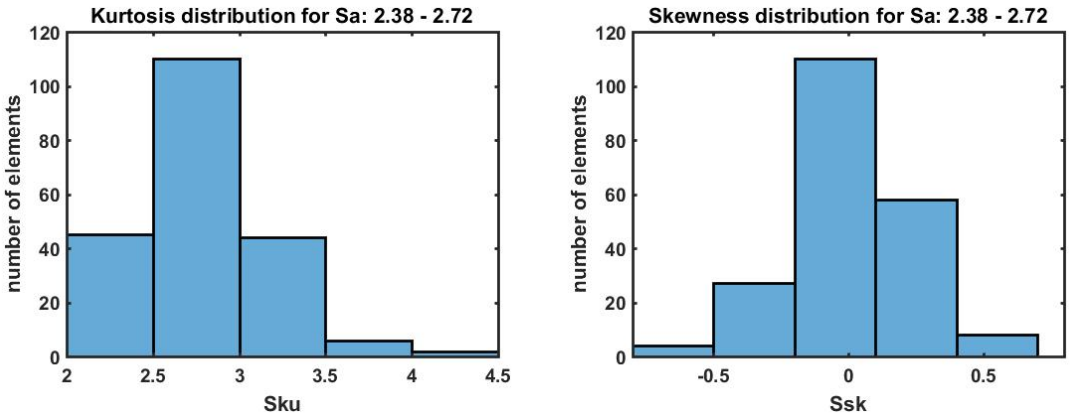

Figure 20 Distribution of Ssk and Sku parameters in for Sa in between 2.38 and 2.72 μm

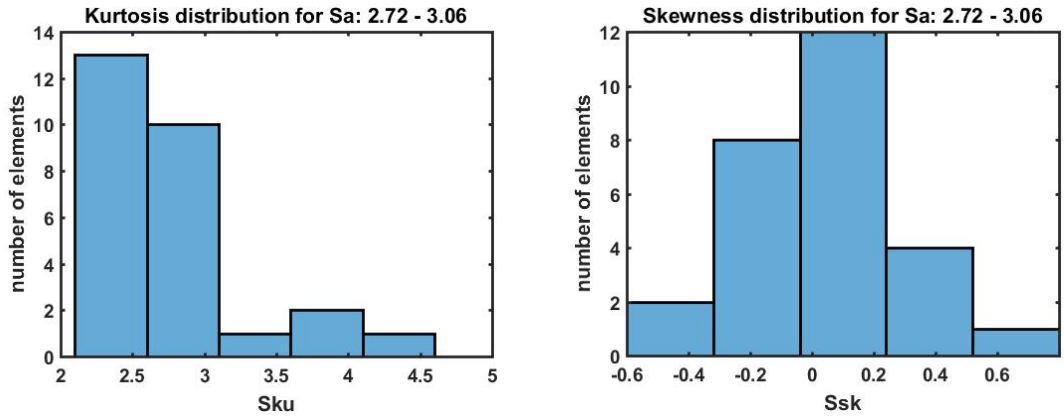

Figure 21 Distribution of Ssk and Sku parameters in for Sa in between 2.72 and 3.06 µm

Figure 14, Figure *15*, Figure *16*, Figure *17*, Figure *18*, Figure *19*, Figure *20* and Figure 21 show that each class presents spread values of *Ssk* and *Sku* and this is fundamental in order to generalize the conclusions and moreover in order to find the relation between the void pixels and each single parameter.

Data Processing

The results for parameter Sa are presented in Figure 22. Figure shows the results obtained for a single surface (the results are qualitatively similar for the measured surface). In this paragraph it is highlighted how the results are managed for obtaining the final tables and the results presented in the next paragraph. Each point in orange represent the value calculated on the topography not reconstructed, and then the blue circles represent the values calculated on the reconstructed topography. These data, for each different surface and moreover for each different parameter are managed and analysed following the described procedure.

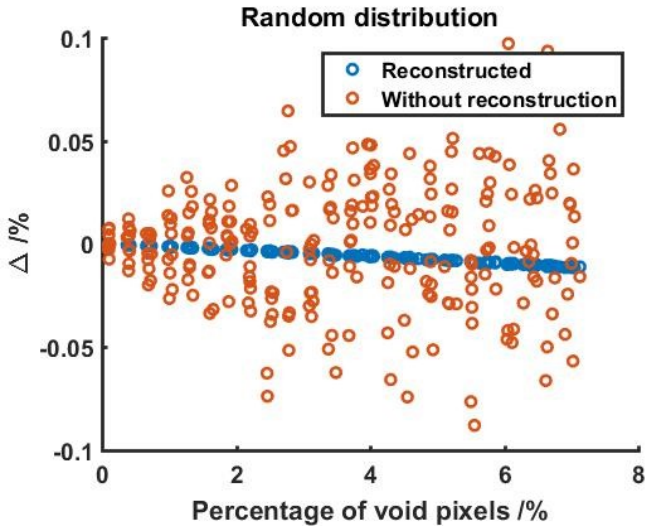

Figure 22 Example of the results obtained for a numerically generated surface

At the end of the simulation process, the obtained prameters are stored in a $m \times n \times k$ matrix, in which k is the number of surfaces analysed in that class. For each k (this means for each height map), the number of rows of the matrix, m, is equal to the void pixels distribution analysed. For each surface and for each void distribution are saved the number of voids, the parameters evaluated on the reconstructed surface and the parameters evaluated on the not-reconstructed surface. Figure 22 presents only the results for one single surface; for the overall analysis a total amount of 2'070'000 scatter points were analysed for reconstructed surfaces and similar amount of cases for not-reconstructed surfaces. The variation Δ is expressed as percentage. The difference between the obtained value (after the void creation process) and the reference value (calculated on the reference surface) is divided by the reference value and multiplied by 100. In order to analyse the effect of every single parameter, the surfaces are divided in classes following the Sa parameter. Moreover, for each single class the points are divided in classes considering the percentage. The division was developed considering an interval of 1%, starting from the 0% value. In this way, the mean value and the standard deviation inside the class are computed and discussed. An example of the result of this process is presented in Figure 23. On the left part of the above mentioned are presented the results for a corrected surface, then on the right side are shown the results for a single surface without reconstruction (not-reconstructed).

In order to understand the correlation between the Sa parameter and the other parameters, considering the class division previously done, for each class is analysed the tendency of the parameter (in terms of delta respect to the reference value). The results are presented in the next chapter. Moreover, the final correlation was developed on the entire batch of surfaces, considering separately every single parameter.

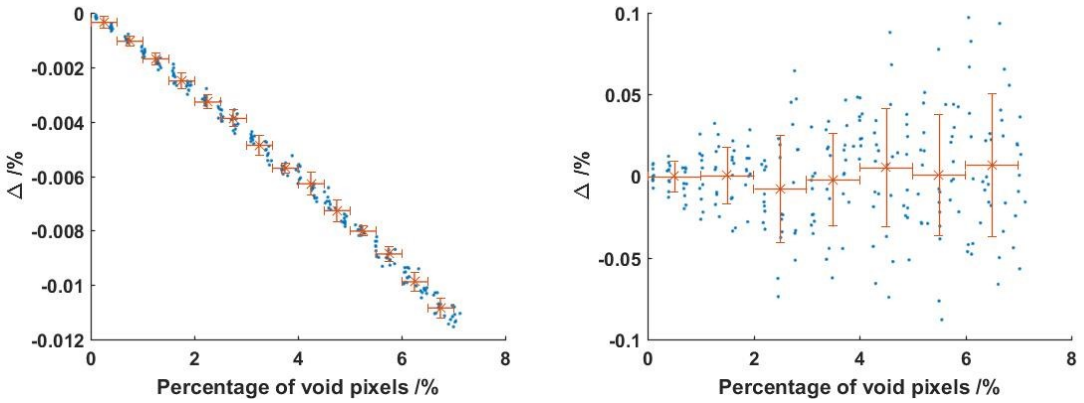

Figure 23 Example of distribution of the results for reconstructed surfaces (on the left) and not-reconstructed surfaces (on the right) considering a random void distribution

Results and discussion

In this part are presented all the results obtained on the simulated and real surfaces. Results for the different *Sa* classes are shown in the first part of the chapter. No clear correlation between the Δ and the percentage changing the *Sa* parameter was identified. These results ensure that an overall consideration, on the entire batch of surfaces, considering separately each single parameter would give general and applicable relation.

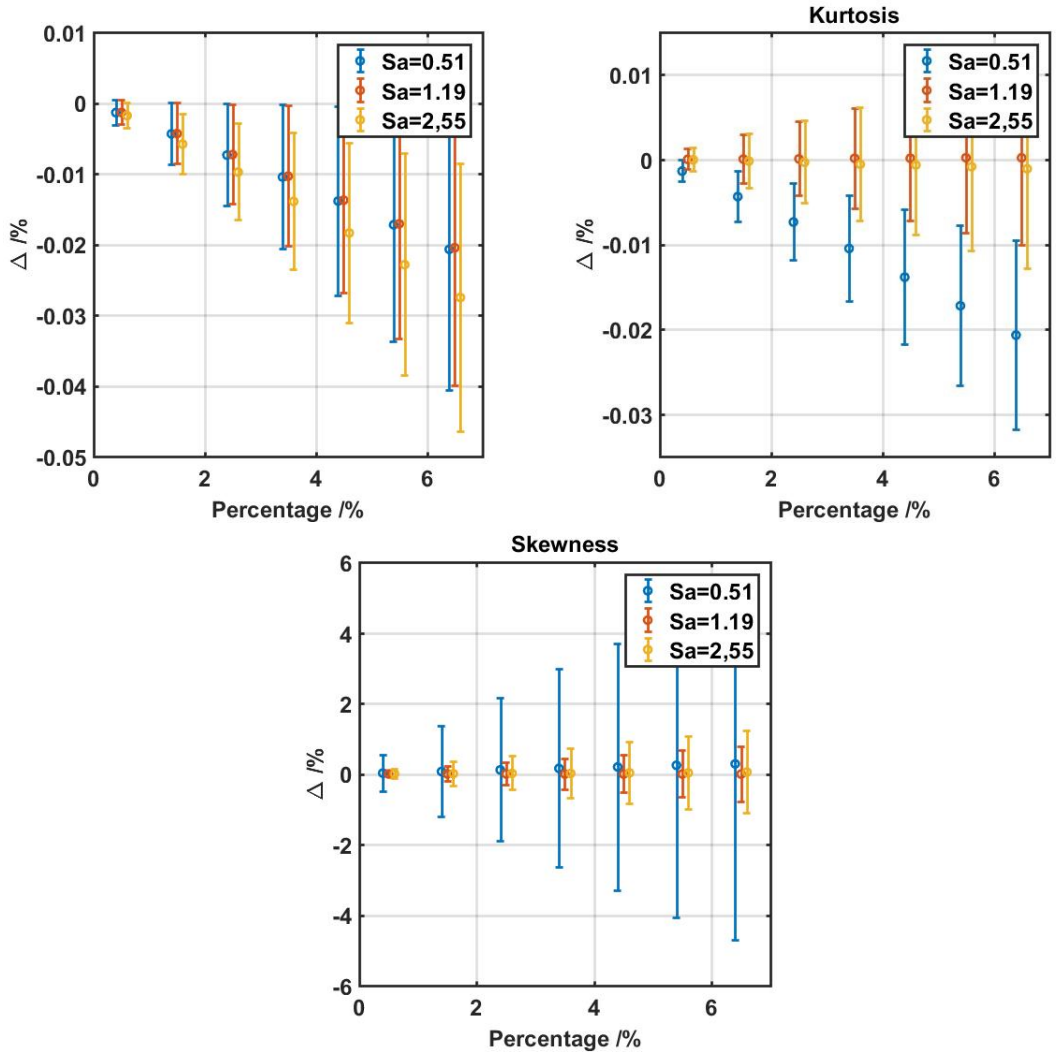

Figure 24 Results for the random distribution of void pixels after reconstruction of void pixels

Figure 24 presents the results for the *Sa*, *Ssk* and *Sku* parameters in the case of random distributed void pixels and with reconstruction of the void pixels before parameters evaluation. Three *Sa* classes are presented, characterized by class mark of 0.51, 1.19 and 2.55 um. The deviation, as previously said, represents the standard deviation inside each class. There is a small increment of the Sa mean deviation with the Sa reference value. But this is confirmed only between the couple of values (0.51, 1.19 μm) and 2.55 μm. Otherwise the trend is not confirmed by for *Sku*. Kurtosis is changing a lot from the set

of values with lower *Sa* and the other two classes. In both *Sa* and *Sku* the dimension of the standard deviation band is pretty equal for the 3 classes. Skewness otherwise is following an inverse relation with the *Sa* parameter. Decreasing the *Sa* parameter seems that the *Ssk* variability is hugely increasing. Moreover, the mean deviation is influenced only in the case of small *Sa* value (Sa=0.51 μm). In the case of *Sa* equal to 1.19 and 2.55 μm the mean value of the Δ is around 0. The entity of the effect of void pixels is completely different for these three parameters. The variability on *Sa* reaches a maximum value of 0.04%, for *Sku* the maximum is reached at 0.02% and finally for *Ssk* is reached at 8%.

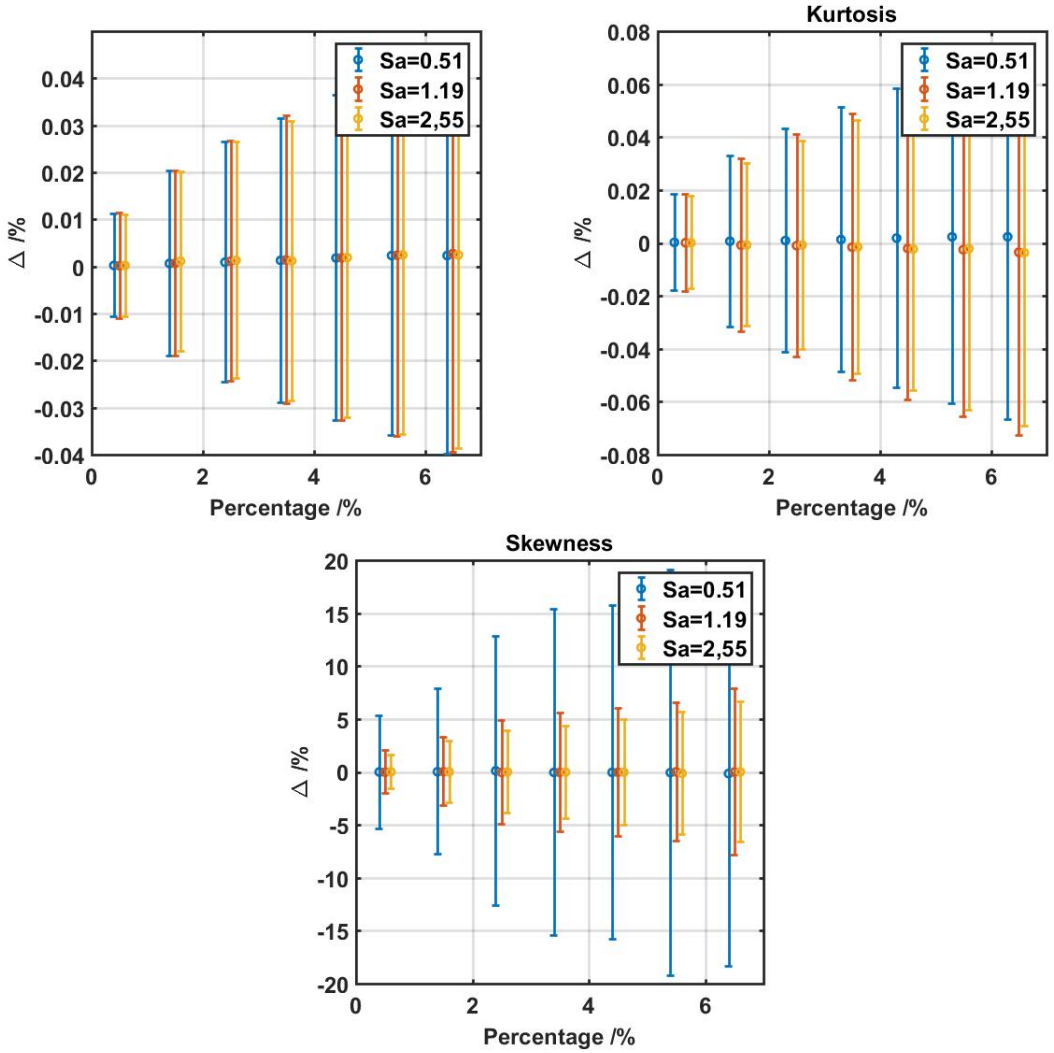

Figure 25 Results for the random distribution of void pixels without reconstruction of void pixels

Similar trend is followed in the case of not reconstructed surfaces. Figure 25 shows the results for the *Sa*, *Ssk* and *Sku* paremters in the case of not reconstructed surfaces. As previously said, three *Sa* classes are presented, same values presented in the reconstructed

case (class mark of *Sa* equal to 0.51, 1.19 and 2.55 µm). In this case, seems that the *Sa* mean deviation increases with the percentage of void pixels and the variability is constant. *Sa* reference value of the surface does not influence the variability of the calculated parameter. Also Kurtosis is pretty constant in the three different classes. Respect to the reconstructed surface there is an increment of the variability: *Sa* variability is 0.8% and the absolute variability of *Sku* is around 1.5%. Skewness otherwise is following also in this case an inverse relation with the *Sa* parameter. Decreasing the *Sa* parameter seem that the *Ssk* variability is hugely increasing. The mean deviation in this case is not influenced by the presence of void pixels. The variability is more than double times the variability obtained on the reconstructed surface and around 36%.

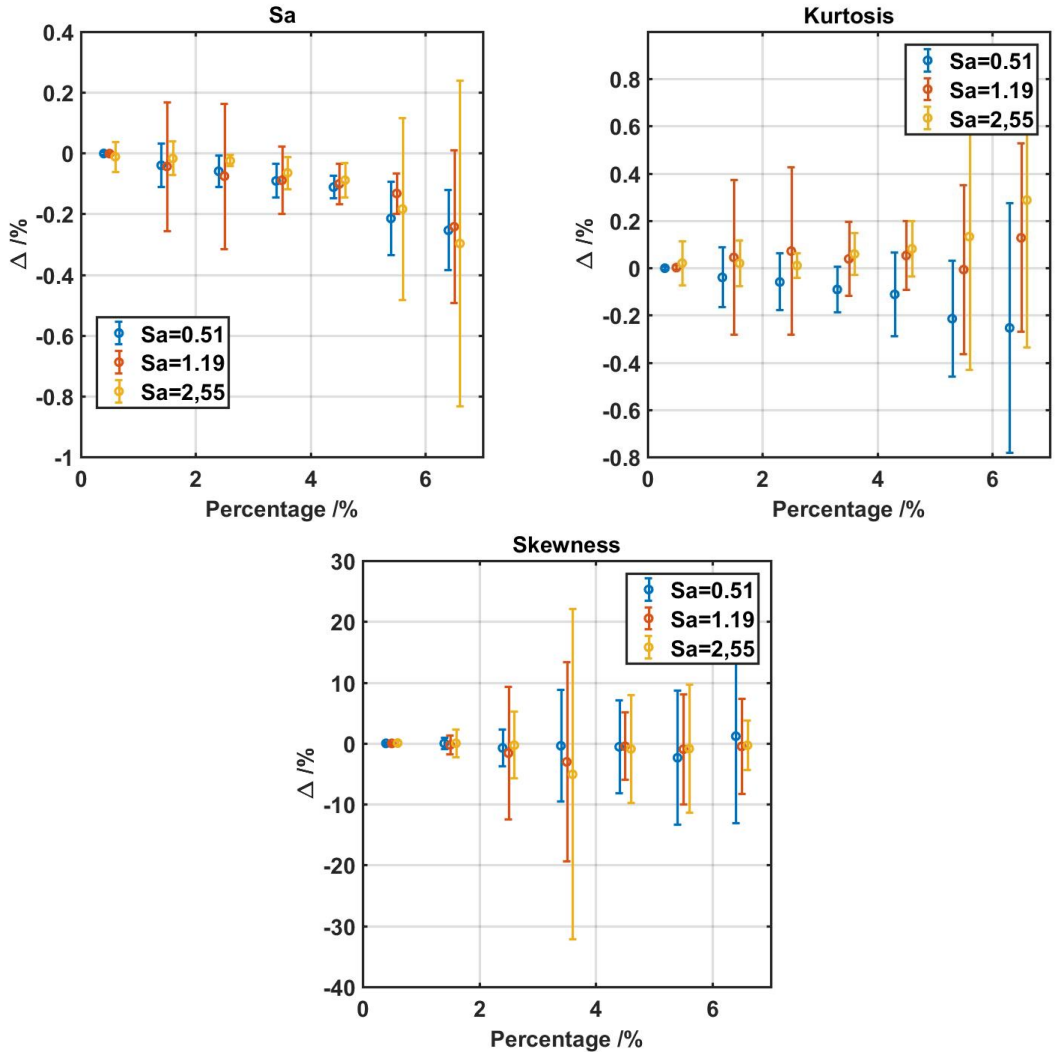

Figure 26 Results for the slope based distribution of void pixels after reconstruction of void pixels

The results presented here above, in Figure 24 and in Figure 25, highlight the relation between the variability and the percentage of void pixels. Moreover, the absolute value

of the variability calculated on the reconstructed surface is smaller than the variability of the not-reconstructed surface. From these results, it is clear that the relation between *Sa* and the other two parameters is missing. For this reason, for the identification of a relation that describes the variability trend function of the percentage, the entire batch of surfaces and parameters will be presented in the next part, after the analysis of the results obtained on the surfaces influenced by the slope based void distribution.

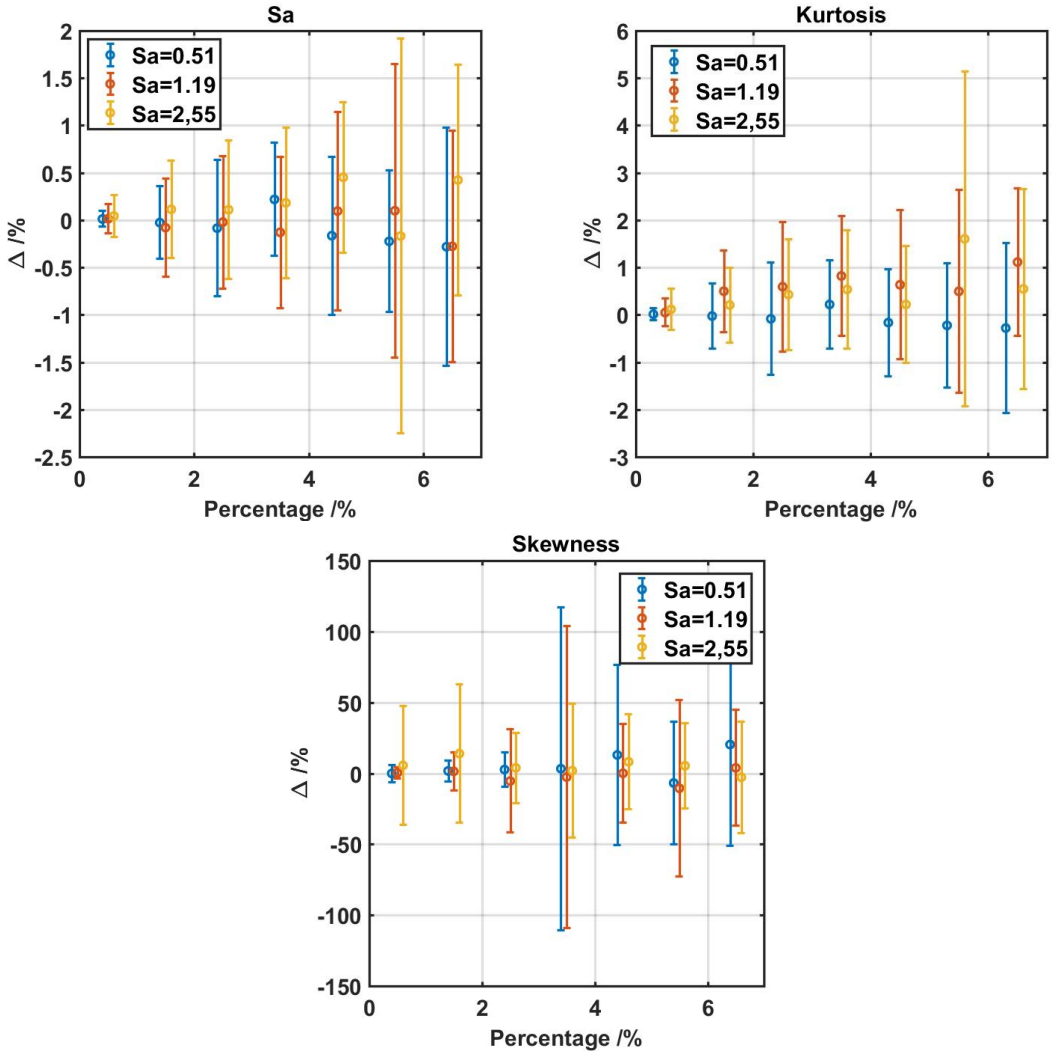

Figure 27 Results for the slope based distribution of void pixels without reconstruction of void pixels

Same considerations as above could be done for the slope based void distribution. The results obtained with the different void generation method, divided in classes considering the *Sa* value, are shown in Figure 26 and in Figure 27. In addition, in this case the plots highlight the relation between the variability and the percentage of void pixels. Moreover, the absolute value of the variability calculated on the reconstructed surface is definitely smaller than the variability of the not-reconstructed surface. Also in this case is clear that

the relation between Sa and the other two parameters is missing. No relation between the Sa and the other parameters is confirmed from the previous results. Reducing the complexity of the relation to a single variable, each single parameter is studied separately. Moreover, form the previous results, it is clear that the variability band is not influenced by the absolute value of the reference parameter. This implies that a general relation that describes the variability only associated with the percentage of void pixels could be identified. For this reason, in the next part the results obtained on the entire batch of surfaces are presented. The complete amount of different simulations (2'070'000 for random distributed void pixels and 2'070'000 for sloped based distribution) are divided in classes only considering the percentage of void pixels. Each single parameter is analysed. *Figure 28* shows the results for the *Sa* parameter: the left side shows the random distribution of void pixels and the right side presents the slope based distribution. As clearly shown, the effect is completely different.

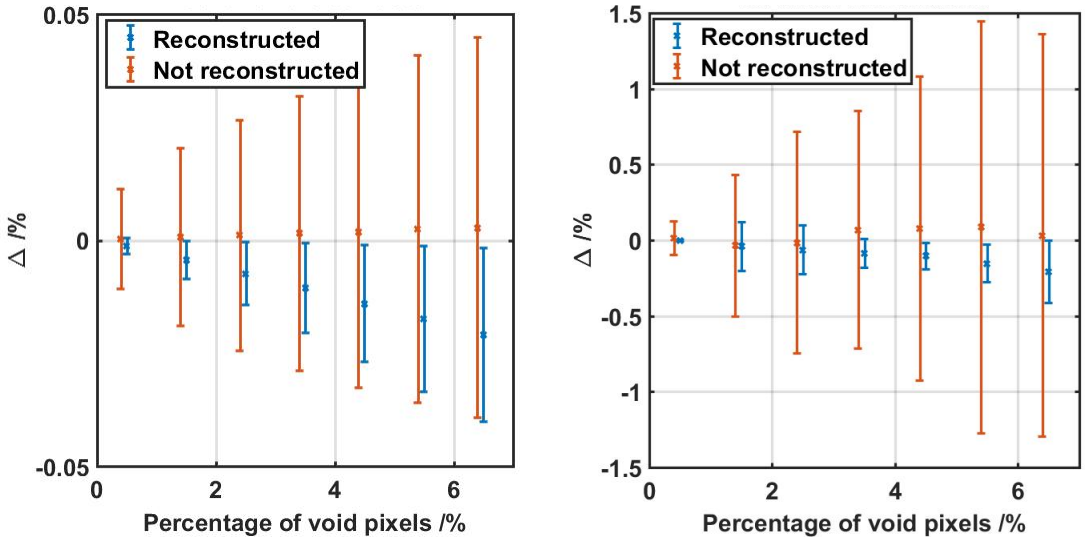

Figure 28 Distribution of the Sa values obtained on the reconstructed and on the not reconstructed surfaces. On the left random distribution, on the right tilt distribution of void pixels

Because of the sensitivity of the surface morphology to the rotations, in the case of the slope based method, the generated void pixels are much more connected then the void generated through the random method. The variability of the *Sa* parameter (associated to the physical interaction between the optical instrument and the surface steepness) is around the 3% in the case of not-reconstructed surfaces and less than 0.5% for the reconstructed one. On the contrary the variability associated with dust and noise is around 0.08% (random distribution) for the not-reconstructed surface and less than 0.04% for the reconstructed one.

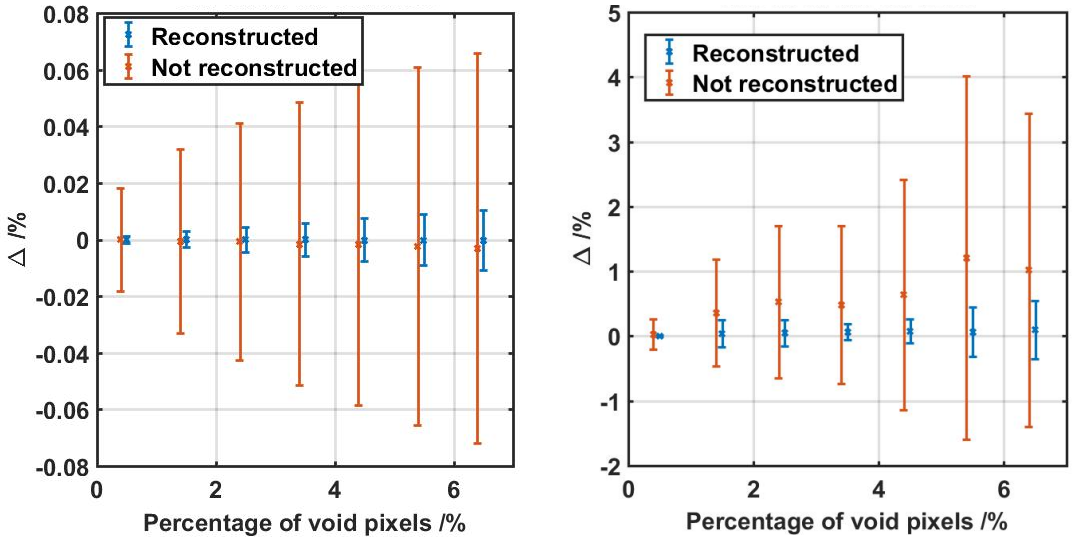

Figure 29 Distribution of the Sku values obtained on the reconstructed and on the not reconstructed surfaces. On the right random distribution, on the left tilt distribution of void pixels

Figure 29 shows the trend of the variability for the *Sku* parameter in the same conditions described before. Also in this case the variability is bigger than in the case of the not-reconstructed surface. The trend and the absolute variability for *Sku* is similar to the variability obtained for *Sa*. Maximum variability obtained is 0.1% for the random distribution, in the case of not-reconstructed surfaces. The reconstruction reduces the variability to a maximum value of 0.03 %. The slope-based distribution is more severe, causing a 4.5% in the case of the not-reconstructed surface and a 1% for the reconstructed ones.

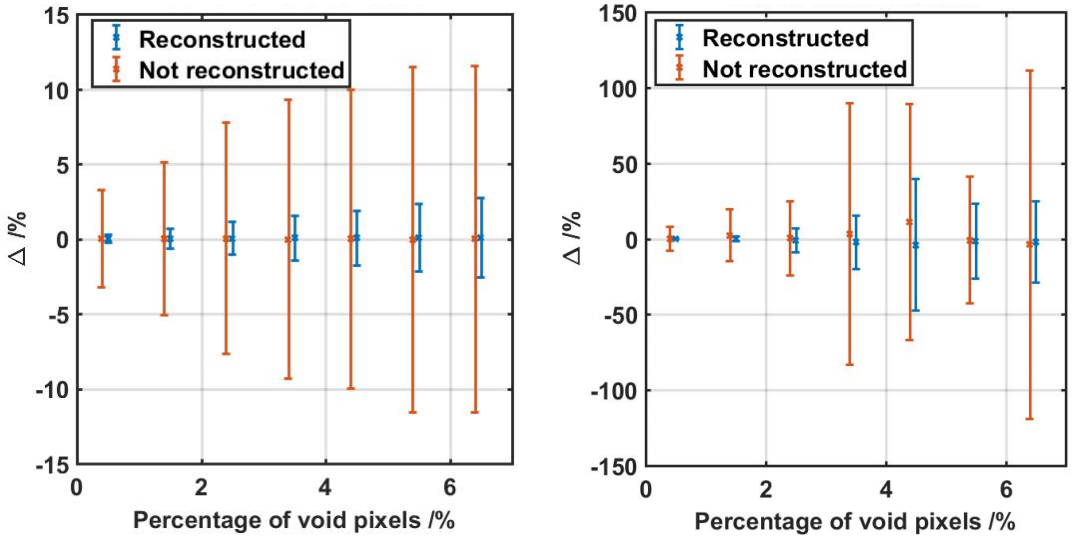

Figure 30 Distribution of the Ssk values obtained on the reconstructed and on the not reconstructed surfaces. On the right random distribution, on the left tilt distribution of void pixels

Finally, Figure 30 shows the variability of the *Ssk* parameter in function of the percentage of void pixels. In both cases the results shows that the voids are hugely influencing the variability. In this case, the reduction of the variability through the reconstruction is really important. The variability is reduced by a factor 10 in both random and slope-based distribution. *Ssk* is particularly sensible to the void pixels, but also in this case is possible to limitate the effect through the interpolation process. The obtained results are finally used for the determination of analytical relations. Through these relations a quantification of the variability respect to the percentage of void pixels is obtained, considering both the effect of the noise and random distributed voids and the slope associated ones.

Figure 31 shows the scatter plot of the variability for *Sa* parameter. The mean deviation is removed from the data, in order to consider it as a systematic effect. The scatter points represent the calculated standard deviations, considering a coverage factor of 2. The red line describes the variability for the not-reconstructed surfaces and the blue line shows the reconstructed trends.

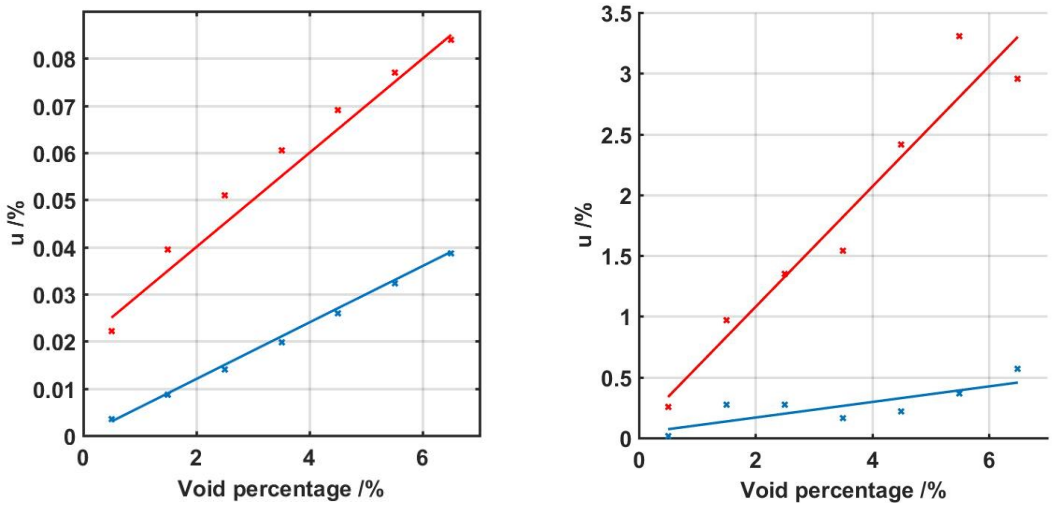

Figure 31 Relation obtained for the Sa parameter. On the left side the random effect, on the right the slope based effect. Red is associated to the not-reconstructed values, blue is associated to the reconstructed ones

From the scattered value a continuous relation was obtained through linear fitting. The obtained relations that describe the variability function of the percentage of void pixels are resumed in Table 4 . In Table 4 are also presented the equations for the correction of the systematic deviation associated with the presence of void pixels.

		Variability	**Systematic**
Random based	Reconstructed	$0.006 * \%Void$	$0{,}0033 * \%Void$

	Not-reconstructed	$0.01 * \%Void + 0.02$	$0{,}0004 * \%Void$
Slope based	Reconstructed	$0.064 * \%Void + 0.04$	$0{,}033 * \%Void$
	Not-reconstructed	$0.494 * \%Void + 0.09$	-

Table 4 Relation between the percentage of void pixels and the variability and systematic error of the Sa parameter

Figure 32 shows the scatter plot of the variability for the *Sku* parameter. The scatter points represents the calculated standard deviations, considering a covering factor of 2. The red line line describes the variability for the not-reconstructed surfaces, on the contrary the blue one is related to the reconstructed surfaces.

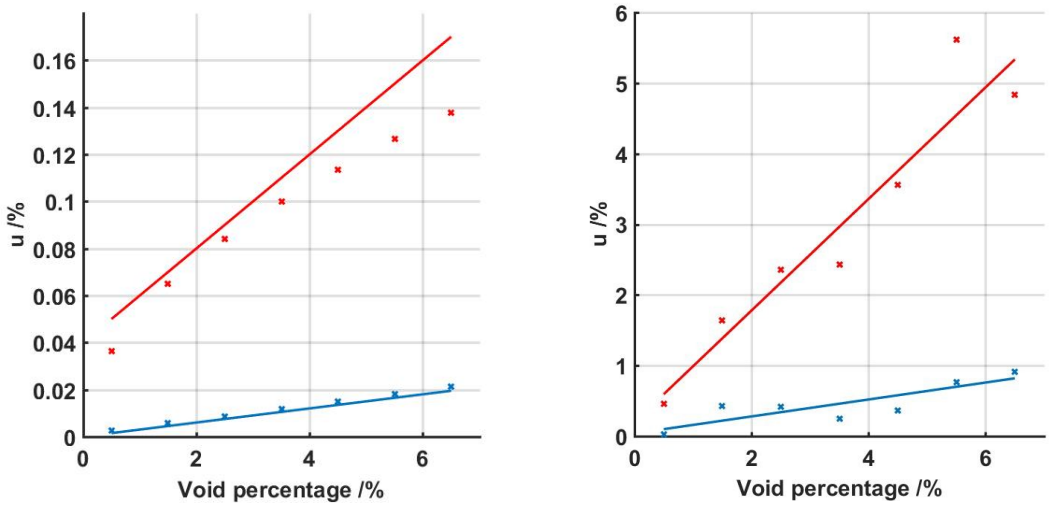

Figure 32 Relation obtained for the Sku parameter. On the left side the random effect, on the right the slope based effect. Red is associated to the not-reconstructed values, blue is associated to the reconstructed ones

The obtained relations that describe the variability function of the percentage of void pixels are resumed in Table 5. In Table 5 are presented both the results for the random based distribution and the slope based distribution.

		Variability
Random based	Reconstructed	$0.003 * \%Void$
	Not-reconstructed	$U = 0.02 * \%Void + 0.04$
Slope based	Reconstructed	$U = 0.12 * \%Void + 0.04$
	Not-reconstructed	$U = 0.79 * \%Void + 0.2$

Table 5 Relation between the percentage of void pixels and the variability and systematic error of the Sku parameter

Sku parameter does not present a systematic error in the case of random based voids.

Finally the relations obtained for the *Ssk* parameter are presented in Figure 33. In this case the absolute variability is much more influenced by the void percentage. Also in this case the reconstructed surfaces ensure a lower variability of the parameter.

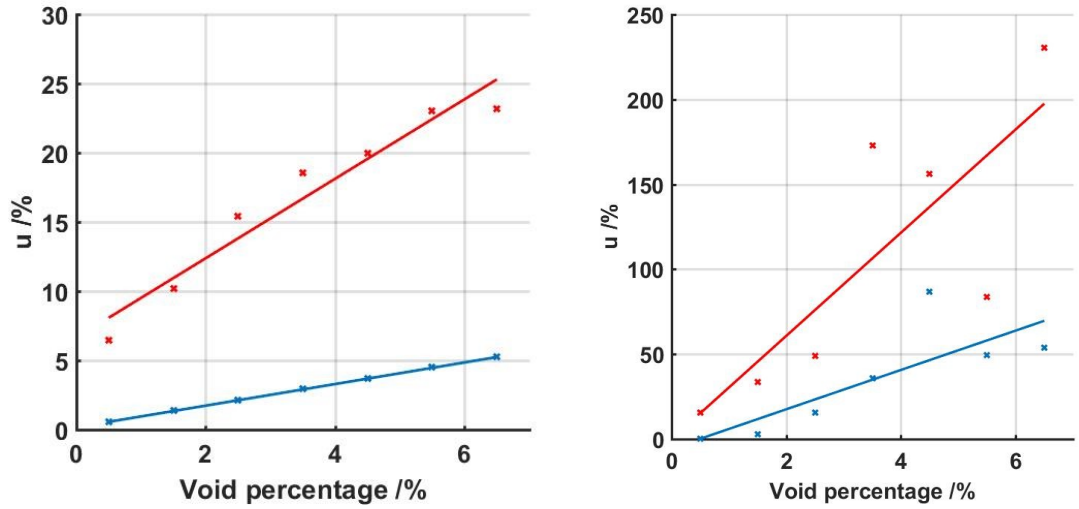

Figure 33 Relation obtained for the Ssk parameter. On the left side the random effect, on the right the slope based effect. Red is associated to the not-reconstructed values, blue is associated to the reconstructed ones

The relations obtained through linear fitting are shown in Table 6. The variability associated with both the random based and slope based is really influenced by the void pixels presence.

		Variability	**Systematic**
Random based	Reconstructed	$0.78 * \%Void + 0.17$	$-0{,}01 * \%Void$
	Not-reconstructed	$2.87 * \%Void + 6.64$	-
Slope based	Reconstructed	$11.58 * \%Void - 5.6$	$-0{,}45 * \%Void$
	Not-reconstructed	$30.39 * \%Void$	-

Table 6 Relation between the percentage of void pixels and the variability and systematic error of the Ssk parameter

Obtained results confirm that the evaluation of the roughness parameters without the reconstruction of the void pixels is characterized by a bigger variability. *Sa* and *Sku* are less influenced by the presence of the void pixels, on the contrary *Ssk* reaches variability bigger than 100%.

The results obtained with the real surfaces and presented in the paper are compared with the final relations obtained through the simulations in terms of *Sa*.

Random-based							
Sa ref (µm):		**1.354**	**1.359**	**1.518**	**1.519**	**3.131**	**3.142**
Not-Reconstructed	Mean	0.002	0.003	0.003	0.004	0.003	0.003
	Std	0.023	0.024	0.020	0.002	0.019	0.019
Recostructed	Mean	-0.001	-0.001	-0.0006	-0.0006	-0.0004	-0.0004
	Std	0.0007	0.0007	0.0005	0.0005	0.0005	0.0004

Table 7 Results obtained from the real surface for 1% of void pixels and random based distribution. Results are expressed in percentage respect to the reference value

Table 7 shows the results obtained for the 6 different surfaces under investigation in case of random distribution of void pixels. From the relations obtained from the simulated surfaces using the random distribution, because of 1% of void pixels the induced variability is below 0.03% of the reference Sa value (in the case of not-reconstructed surface). This value is confirmed by the real surfaces, in which the variability is below that value for all the 6 surfaces. The systematic effect is not perfectly described by the relation, but after correcting the systematic effect through the relation proposed in Table 4, the variability is inside the variability band. The same considerations could be done for the reconstructed surfaces: in that case, the relation gives a value of the variability equal to the 0.006% of the reference parameter and the results obtained from the real surfaces are in below 0.001% of the reference parameter.

Finally, Table *8* shows the results in case of slope based void distribution. Considering the relation presented in Table 4 the variability calculated for the reconstructed surface for *Sa* parameter is equal to 0.14% of the reference value. Real surfaces are inside the variability band with values in between 0.003 and 0.004% of the reference value. Also the not reconstructed ones are compatible, in between 0.1 and 0.03, when the numerical relation gives a variability band of 0.58% of the reference value.

Slope-based							
Sa ref (µm):		**1.354**	**1.359**	**1.518**	**1.519**	**3.131**	**3.142**
Not-Reconstructed	Mean	0.033	0.033	0.200	0.190	0.260	0.026
	Std	0.026	0.026	0.067	0.063	0.087	0.080
Reconstructed	Mean	-0.0055	-0.0055	-0.0065	-0.014	-0.0034	-0.0028
	Std	0.0031	0.0031	0.0030	0.0039	0.0020	0.0038

Table 8 Results obtained from the real surface for 1% of void pixels and slope based distribution. Results are expressed in percentage respect to the reference value

Presented results confirm the power of the reconstruction in terms of variability band, both in case of noise related void pixels and slope related void pixels. Moreover, the

numerical simulations generalize the results and propose a new instrument for the evaluation of the variability of surface parameters.

Conclusions

The correlation between the presence of void pixels and surface roughness parameters are analysed and presented in this chapter. Two different numerical methods were developed for the generation of void pixels: random distribution and slope based distribution of void pixels. These two different methods would simulate the contribution of two physical phenomena that influence the measurement results: presence of random noise in the topography (dust, noise, optical disturbances etc.) and the objective numerical aperture (sample slope and roughness flanks). Through a numerical approach, 4500 different surfaces were analysed and compared. For each surface 460 different cases were simulated: 230 considering random distributed void and 230 considering slope dependant void. Then the parameters calculated on the reconstructed surface (the void pixels are replaced through an interpolation process) and the parameters evaluated on the not-reconstructed surfaces are stored and used for the variability calculation. The solution presented highlights the need of reconstruction in order to minimize the variability of the parameters and ensure an enhancement of the optical measuring process. Moreover, the relations presented in this chapter give the possibility to estimate the variability of the calculated parameter associated with the presence of void pixels. This model was verified on six different real surfaces and results confirm the reliability of the obtained relations. Finally, in this chapter are presented some new tools for the control of surface measurement parameters variability, quantifying the effect of the presence of void pixels.

3. Monitoring of burrs in micro-milling by advanced processing of void pixels

A newly developed method for the control of the micromachining process will be presented in this chapter. The main goal of this research is the enhancement of the capabilities of the confocal microscopy, adding the possibility to evaluate the burrs longitudinal width. In micromachining the dimensions of the machined slots are in the order of tens of microns. In order to control the machining process the geometry, the roughness of the machined surface and moreover the presence of burrs should be checked. Currently confocal microscopy is suitable for in-line measurement, but the capabilities of the instrument are limited from the steepness of the surfaces (in particular the steepness of the burrs). This method, based on a combination of 3D information and image processing techniques, overcomes this limitation and ensures a complete characterization of the machined slot through a single measurement phase.

Introduction

Nowadays, micro-milling is increasingly used in the production of micro-sized components in many different fields, such as automotive, aerospace, biomedical (Bissacco et al. 2006; Kou et al. 2015), thanks to the high performances it assures, in particular high material removal rate, high flexibility, and possibility to machine any metal alloy in any 3D shape. However, micro-milling can produce three-dimensional burrs, which represent one of the major issues of this machining process, as they affect the capability to meet the part desired tolerances (Mian et al. 2010; Câmara et al. 2012; Filiz et al. 2007), being their size of the same magnitude of the cutting tool diameter (Kiswanto et al. 2015), therefore significantly larger than those typical of conventional machining. Furthermore, burrs may be harmful for the operators, which can be injured while handling their sharp edges (J.C. Aurich et al. 2009), and, if not properly removed, they may affect the part functionalities, giving raise to possible difficulties in assembly and damages due to their breaking during the part service life. In addition, the deburring process is in general time-consuming, costly, and does not bring any added value to the process chain. As example, Aurich et al. (J.C. Aurich et al. 2009) estimated that deburring represented more than 9% of the total machining costs in Germany, proving that the deburring process had a large economic impact on the whole machining-based process

chain. The burrs removal in case of micro-milled parts is even more difficult, since to carry out deburring operations on micro-features through traditional methods (brushing, etching, electrolytic or ultrasonic) can be potentially not feasible as it can result in unacceptable damage of the part itself (Câmara et al. 2012; Filiz et al. 2007; Aramcharoen & Mativenga 2009). Therefore, due to their significant impact, the mechanisms of burrs formation in micro-milling have been largely investigated and modelled (Kumar et al. 2017; Vipindas et al. 2016), with the aim of reducing them as much as possible. The main parameters influencing the burrs formation were found to be the cutting speed, undeformed chip thickness, tool sharpness, tool feed, and workpiece material (Jahanmir 2011; Aramcharoen & Mativenga 2009; Thepsonthi & Özel 2012). It was shown that the burrs formation were reduced at low cutting speeds and high feed rates (Filiz et al. 2007; Özel et al. 2011), being the burrs height linearly proportional to the feed per tooth (Lee & Dornfeld 2005). On the other hand, the increase of the tool diameter, number of flutes and depth of cut was shown to decrease the burr height (Câmara et al. 2012). More ductile workpiece materials were found to produce larger burr size (Aramcharoen & Mativenga 2009; Mian et al. 2010; Thepsonthi & Özel 2012), but harder materials favoured the wear occurrence and, thus, also the burrs formation (Aramcharoen & Mativenga 2009; Özel et al. 2011; Thepsonthi & Özel 2012). As regards the milling strategy, down-milling was found to generate larger wavy burrs, whereas up-milling produced smaller ragged-type burrs (Aramcharoen & Mativenga 2009; Mian et al. 2010; Filiz et al. 2007; Câmara et al. 2012). Piquard et al. (Piquard et al. 2014) stated that the cutting strategy was the parameter mostly influencing the burr thickness, finding curly-shaped thinner burrs in up-milling. The aforementioned studies dealing with the sensitivity of the process parameters to the burrs formation may help in reducing them, but since in most micro-milling cases their formation is unavoidable and their removal unfeasible, in-line measuring techniques may be useful for their characterization and may provide a fast feedback on the process, e.g. information about the tool wear evolution.

Non-destructive methods, including mechanical and optical systems, can be suitable for in-line measurements. However, mechanical-based systems have to touch the burrs, potentially destroying them and therefore damaging the part. Optical systems, based on cameras, microscopes, laser and interferometers (Thepsonthi & Özel 2012; Jahanmir 2011), are advantageous in this sense, as they allow preserving the burrs while measuring them. Ko (Ko & Park 2006) proposed different methods, based on triangulation,

conoscopic holography and interferometry, for the measurement of the micro-burrs geometry in micro-drilled parts, but, even if they were suitable for micro-burrs detection, they were not designed for in-line measurements. On the other hand, Tsai (Tsai & Lu 1996) developed a machine vision system based on automatic contour detection for burrs and peripheral defects of casting parts, but limited to macro-sized burrs. Lee (Lee & Dornfeld 2005) uses a profiler in order to quantify the height, without describing the method and the approach developed. However, systems developed exclusively for burrs measurement, either macro or micro, are not flexible enough for a comprehensive quality check of the machined part, since, applying these methods, additional measuring instruments have to be set-up inline for the verification of the geometry and surface roughness quality of the part. Different studies were developed in the past in order to classify the burrs and identify the most important characteristics. Gillespie as cited in (Lee & Dornfeld 2005; J.C. Aurich et al. 2009) is one of the first describing different types of burrs. He mentions four types of machining burrs: Poisson burr, rollover burr, tear burr and cut-off burr. The Poisson burr is a result of the material's tendency to bulge to the sides when it is compressed until permanent plastic deformation occurs. Rollover burr is essentially a chip which is bent rather than sheared resulting in a comparatively large burr. This type of burr is also known as an exit burr because it is usually formed at the end of a cut. The tear burr is the result of material tearing loose from the workpiece rather than shearing clearly. It is similar to the burr formed in punching operations. The cut-off burr is the result of workpiece separation from the raw material before the separation cut is finished. Aurich et al., in (J.C. Aurich et al. 2009) classify the burr measurement methods as:

- one-, two- or three-dimensional,
- destructive or non-destructive,
- with or without contact
- in-process and out of process

Table 9 shows different methods of burr detection techniques and burr measurement.

<table>
<tr><th colspan="5">METHODS OF BURR DETECTION AND BURR MEASUREMENT</th></tr>
<tr><th colspan="4">OUT of PROCESS</th><th rowspan="3">IN-PROCESS</th></tr>
<tr><th rowspan="2">With contact</th><th colspan="3">Contactless</th></tr>
<tr><th colspan="2">Optical</th><th>Electro-mechanical</th></tr>
<tr><td>Stylus methods</td><td>Optical microscope</td><td>Light-slit methods</td><td>Eddy-current sensor</td><td>Process monitoring</td></tr>
<tr><td rowspan="4">Metallographical profiles</td><td>Borescope / endoscope</td><td>Laser triangulation</td><td>Inductive sensor</td><td>Force, moment</td></tr>
<tr><td rowspan="3">Scanning electron microscope</td><td>Fring pattern projection</td><td rowspan="3">Computer tomography</td><td rowspan="3">Sound emission analysis</td></tr>
<tr><td>Autofocus methods</td></tr>
<tr><td>Confocal microscopy</td></tr>
</table>

Table 9 Methods of burr detection and burr measurement

Stylus methods are suitable to measure burr heights. But the real profile can't be measured as the data can be influenced by conical shape of the tracer point. All contact measurement methods are limited by the workpiece stiffness, as the burrs can be destroyed or pushed down because of the contact forces (J.C. Aurich et al. 2009). Destructive method is for example a metallographic cross-section of the burr. This method allows an evaluation of burr values from the cross-sections but also burr hardness and structural changes in the material after the machining. It is the only method capable to measure burr thickness and also burr length especially in the case of rolled and spiral burrs. Nevertheless, the preparation of metallographic samples is very time-consuming and allows only to measure at one specific workpiece position (J.C. Aurich et al. 2009). Because of the importance of burrs, during the years different studies were developed for measurement system and measurement techniques for burrs characterization. A deep analysis and description of the geometrical parameters suitable for burrs evaluation and quantification is developed in Aurich's paper.

That paper (J. C. Aurich et al. 2009) and moreover the research developed in the field of burrs measurement was focused on the common machining strategies. In these cases, the identification of the longitudinal geometry of the burr is not so important and representative, respect other direction (in particular, the most important parameter in the case of big burs is the burr height). Destructive methods are not suitable for in-line evaluation, but are the most accurate ones. The preparation of a metallographic cross-section of the burr ensure a complete characterization of the geometry of the burr and

moreover the characteristics. As well ensured in (J. C. Aurich et al. 2009) this is the only method to measure burr length and burr thickness for rolled back and spiral burrs. Non desctructive methods are surely suitable for in-line measurements but also in this cases are divided in mechanical and optical systems. Mechanical system touch the burr, so causes a distortion and also a destruction of the burr itself (in the case of micromachining). Different optical systems were developed based on cameras, microscopes, laser and interferometers. This paper proposed a method that combines image processing techniques and surface topography in order to obtain important information for deburring process in micromachining. Use of an optical profiler to obtain the topography of the machined slot ensure a complete evaluation of the machined part: high accuracy for the combined evaluation of roughness, surface parameters of the machined slot, depth of the slot and moreover, applying the proposed technique, data for deburring processes. The method described is based on a non-conventional use of the measured data and the evaluation of different parameters for the quantification of the longitudinal width and morphology of burrs. One single measurement ensures an entire evaluation of the quality of the micro-machining process.

A standard optical profiler was used to record the topography of the part. The use of profiler data for the geometrical evaluation is based on the approach proposed by Senin et al. (Senin, L. A. Blunt, et al. 2012), here enhanced thanks to the development of an innovative method for using the void pixels. The use of data acquired through an optical profiler allows a comprehensive geometrical characterization of the machined part, besides the evaluation of its surface topography. The proposed method is based on a non-conventional use of the data measured through an optical profiler and on the evaluation of some significant geometrical parameters for the quantification of the longitudinal width and morphology of the burrs. Thanks to a single measurement the quality of the micro-machining process can be assessed.

Case study

The proposed method was applied to a fundamental micro-machining operation, namely slotting used for the realization of micro geometries and features. In case of machining micro-slots, the parameters that have to be first checked from a functional point of view are the roughness of the machined surface and the actual depth of the slot (see Figure 34). Moreover, the possible presence of top and side burrs that can cause shortcomings in handling and assembly has to be verified. Usually, these geometrical characteristics are

inspected after machining in order to continuously control the process and the quality of the final product.

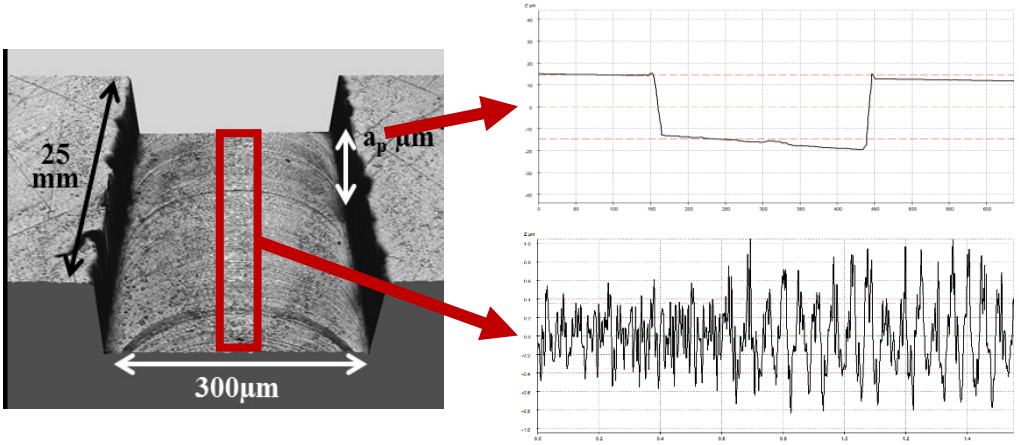

Figure 34 Machined slot, geometry and surface roughness

Table 1 summarizes some measuring systems suitable for the evaluation of the different characteristics of the micro-slots. All the reported methods are clearly not flexible enough for a complete characterization of the micro-slots; moreover, the methods suitable for geometrical characterization are not designed for the roughness and burrs evaluation. On the contrary, the proposed method aims at providing information about all the aforementioned characteristics, enlarging the capabilities of the confocal microscopy technique with a non-conventional use of void pixels.

System	In-line	Slot depth	Slot roughness	Burrs identification
Micro CMM		*V*		
SEM				*V*
Triangulation	*V*			*V*
Interferometry			*V*	*V*
Proposed method	*V*	*V*	*V*	*V*

Table 10 Resume of measurement techniques

Materials and methods

Confocal microscope

Confocal microscopy is not a common technique for the evaluation of burrs. The limit of this technique is related to the numerical aperture of the objective this limitation reduces the collectable information of the burr. Moreover, numerical aperture is proportional to the magnification: bigger magnification means higher numerical aperture of the objective,

smaller magnification means smaller numerical aperture. Numerical aperture of the objective is related to the physical limit of the light to be reflected inside the objective (Yoshizawa 2015; Leach 2011). This is correlated to the steepness of the surfaces: that is the reason why a burr is not completely characterized using a confocal microscope. The approach and method presented in this paper would step forward this limitation trying to collect information from points that are not directly measured.

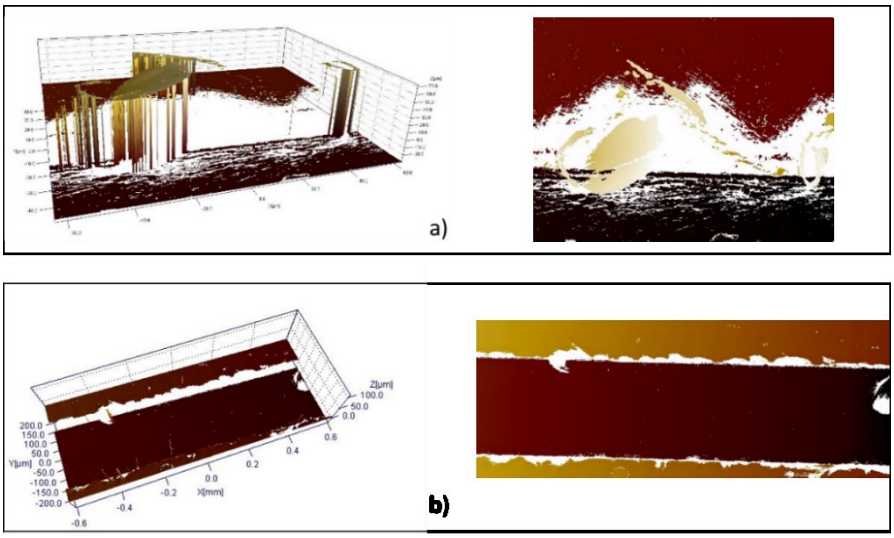

Figure 35 Comparison of different magnification: a) 100x magnification, b) 20x magnification

As previously said, bigger is the magnification higher is the measurable slope, but on the contrary smaller is the field of view. In Figure 35 are presented examples of two topographies: in Figure 35-a the burr is acquired using a 100X magnification (0.98 NA), despite in Figure 35-b the burr was measured with a 20X magnification (0.5 NA). From higher magnification is possible to collect enough information also regarding the height of the burr, but from a statistical viewpoint the measured part is not representative of the entire surface.

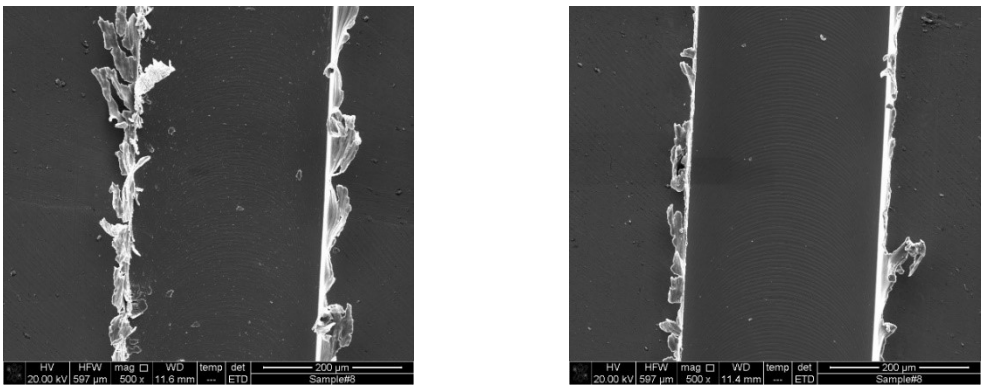

Figure 36 Example of two SEM images of two different machined slots

Considering the two examples reported in figure Figure 36 (SEM images of two slots), it is clear that the distribution of the burrs is changing, moreover using an high magnification objective could be not really representative of the general situation. Moreover, objective with lower magnification are suitable for larger area evaluation and are faster in z scanning: in this way is possible to scan the machined slot once, and collect all the information regarding geometry, surface and burrs. Then, larger area is preferred for geometrical measurement and surface roughness evaluation. The limitation of this approach is that the evaluation could be done only along the longitudinal direction. Moreover, the white areas in the topography (Figure 35) are zones in which the slope is too high to be measured. But in that areas the slope is connected and caused by the presence of the burrs. Using a system like this is necessary to develop particular methods for the transformation of the 3D data in a 2D image, in which the most important information are obtained from not-measured points. Void pixels are linked to the presence of the burrs, overcoming the limitation of the instrument.

Void pixels

All the methods developed in the past are strictly related to a particular instrument. Moreover, every single and different method presents some limitations (type of burr evaluated and different characteristics). The method developed in this paper is based on the use of an optical profiler in order to measure the lateral distribution of the burrs in micromachining. The area of interest is generally characterized by small burrs, so the use of a high accuracy instrument is required. As mentioned above, the limitations of the optical profiler are related mainly to the maximum measurable slope, because of the numerical aperture of the objective. As shown in *Figure 37*, the steep surface of the burr will not be measured by the confocal microscope, enabling the evaluation of the width (considering also a thresholding procedure and filtering).

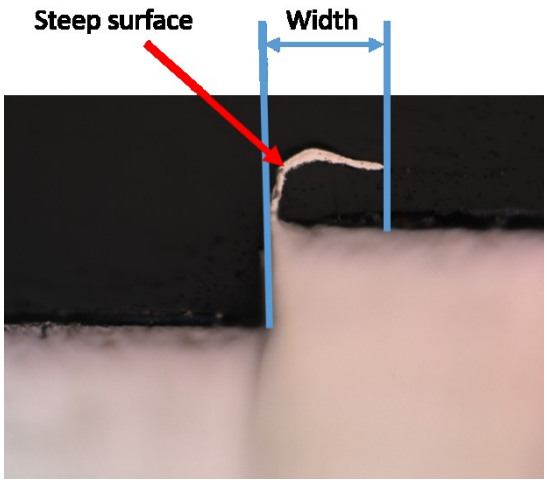

Figure 37 SEM image of a burr section

Moreover, the slopes of the burrs are generally high and not measurable neither with higher magnification. The use of a higher objective magnification means a drastic reduction of the field of view: for burrs evaluation this means an image too focused on a particular part of the machined slot and not statistically representative of all the slot for geometrical measurement and roughness. For these reasons, the method presented here uses the points of the optical profiler that are not measured, so the characteristic of the optical objective to exclude the points that are too sloped.

Functional aspects

The evaluation of the longitudinal width of the burrs is based on the function of the parts obtained by micro-milling processes. Burrs in these cases are thin and generally bended on the external surface, because of this structure they cause problems for subsequent assembly processes. In this case longitudinal characteristics are representative of the quality of the machining process.

As previously described, the evaluation of the burrs with optical instruments (in particular with confocal microscopy) could be used directly in-line at the end of the micromachining stage. In order to choose automatically if a next process is required or not, burrs longitudinal width could be checked. The parameters proposed in this paper are inspired by ISO standard for the evaluation of roughness profiles, considering that the burrs are characterized by completely different morphology and limitations.

It is not directly possible to apply the roughness parameter formulation for the calculation of a mean width because of the undercuts. Undercuts are not considered in the current version of ISO standards for the evaluation of surface roughness. *Figure 38* shows an

example of this effect. The white part represents the burr and it is clearly characterized by undercuts: for the same x value (considering the x axis as the longitudinal axis) the y values are multiple.

Figure 38 Example of a black and white image obtained from the profiler after data process

In order to overcome this problem, is necessary to move to an image approach. The evaluation of the area is done through pixel enumeration. Considering the absolute length of the burr is possible to evaluate the mean width as:

$$Mean\ burr\ width = \frac{A}{L}$$

Where A is the complete area of the burr and L is the longitudinal length of the measured slot. The longitudinal length used for the evaluation has to be taken long enough to ensure that the part is representative of all the burr. Moreover, as described in the next chapter, for the evaluation of the length, alignment and thresholding procedure are required. The mean width has to be considered referred to the edge, used for the alignment and for the evaluation of the longitudinal length.

In order to understand if the burr is uniformly distributed along the machined slot, or is characterized by some isolated peaks, the evaluation of the maximum width of the burr is proposed. To do this, the burr profile has to be considered as a scattered distribution of x,y coordinates, respect the reference line, obtained after alignment of the machined edge. Considering all the points as scattered points is possible to define

$$Max\ width = \max(y_i)$$

Where i goes from 1 to maximum number of elements representing the burr.

With this two different parameters is possible to describe the maximum elongation of the burr and moreover the mean width of the burr. Moreover considering the ratio between the mean width and maximum width is possible to describe the distribution and morphology of the burr.

$$Burr\ ratio = \frac{Mean\ burr\ width}{Max\ width}$$

Burr ratio is useful for the description of the burr segmentation and the continuity of the burr. Burr ratio is 1 if the burr is ideally a rectangle with a width equal to the $Max\ width$, so a continuous burr, with a really low number of peaks is characterized by ratios near 1. On the other side, Burr ratio tend to 0 if the $Mean\ burr\ width$ tent to 0 and the peak is localized (and ideally just a point).

Method description

The procedure applied follows the steps reported in Figure 39. The 3D topography acquired from the instrument is managed in order to exclude alignment problems. Moreover, the height information of the points coming from the topography are used for roughness and surface evaluation (of the machined slot) and also for a thresholding procedure required for the filtration of the points related to the burrs, but measured from the instrument because of a too small slope. All the points in Figure 39 are analysed and developed in the next parts. Shortly, the data acquired from the profiler are managed in order to align and exclude the noise from the height map. After this preliminary step, the data follow two different ways. The 3D map is directly used for the evaluation of the roughness of the machined slot and for the evaluation of the depth of cut. Surface and profile roughness parameters (using multiple profiles in order to compare the results with the reference work) are evaluated on the bottom area of the slot. The geometry of the slot is checked extracting different section for mapping the real depth of cut along the machining direction and moreover the identification of misalignment of the bottom part of the slot. In parallel, the 3D map is managed in order to work on the image for the evaluation of the burrs. As previously said, a deep description of the steps will be presented in the follow.

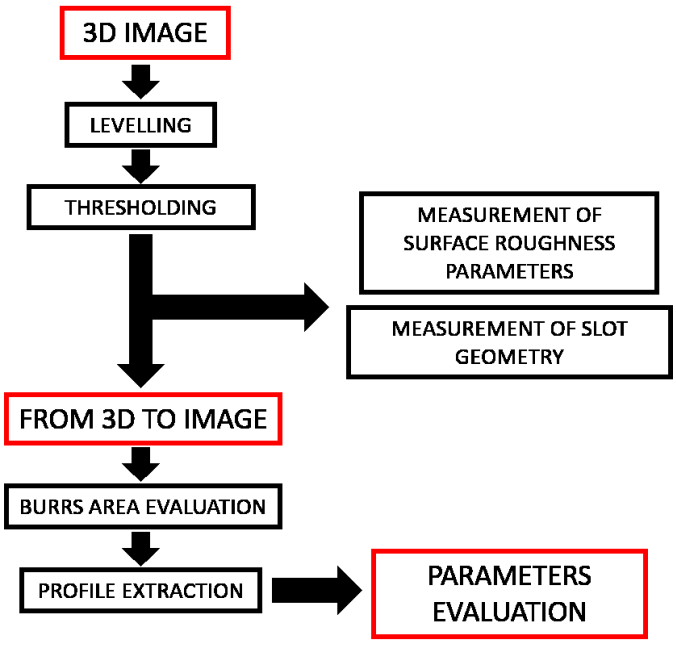

Figure 39 Scheme of the proposed procedure

3D Height map

The image directly obtained from the instrument is an *xyz* point-cloud with all the information regarding the height of the different points. The points that are not measured by the instrument are classified as void pixels, and the height value assumed for these points is fixed at 10000 µm. Figure 40 reported an example of a 3D topography of a machined slot: it is possible to identify two different areas (on which different evaluation are done): machined bottom area (1) and top plane reference area (2).

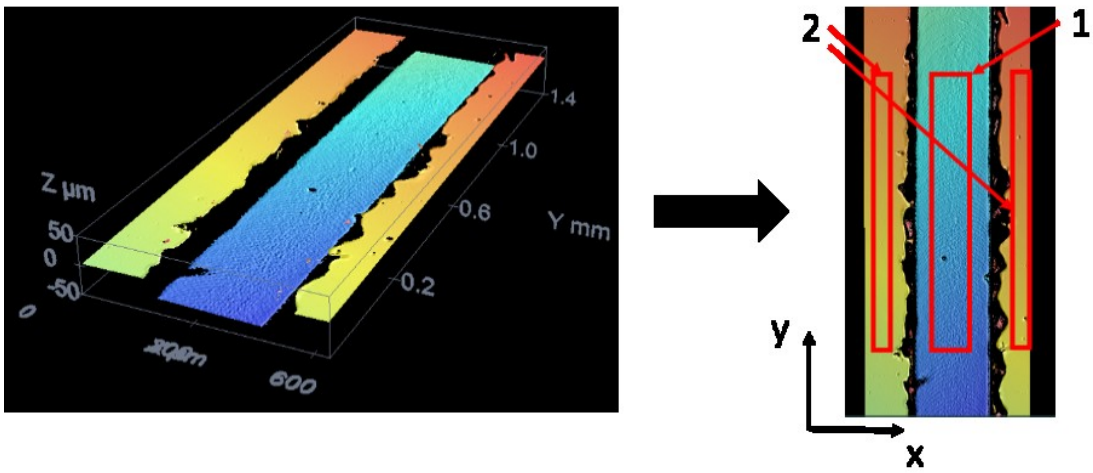

Figure 40 Topography and reference areas

Top area is identified using the histogram of the *z-heights* showed in Figure 41. The higher frequencies of the points are related to the top and bottom areas, the center of mass

of the histogram (represented with the red line in Figure 41) is evaluated and all the points higher than this value are associated to the top plane.

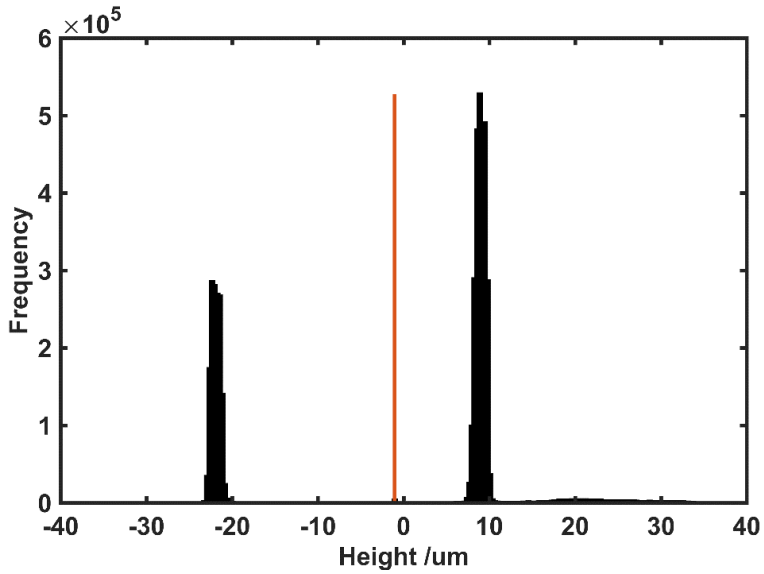

Figure 41 Histogram of the z-heights

After this first evaluation the bottom machined area is extracted from the entire topography in order to evaluate surface roughness parameters: from the 3D topography 10 different roughness profiles are extracted and elaborated according to ISO standards (ISO4287:1997; ISO4288:1996). Profiles are extracted instead of evaluating the surface parameters, only because of the state of the art comparison: machining is mainly controlled and studied through profile roughness parameters. Form correction and filtration of each single profile is automatically developed. The points associated to the top plane are used for the 3D alignment: a plane fitting is applied on the top area and then all the data points are aligned using roto-translation matrices (roto-translation is applied on the *xyz* point cloud). The top plane is aligned with the reference x-y plane, defined as the plane orthogonal to the optical axis. This plane and moreover the evaluation of the height distribution of the points are also used for the thresholding procedure. In this case the problem is related to the definition of the burr: the instrument is not capable to measure surfaces with a slope higher than a certain value, but there are parts of the burrs that are characterized by lower slopes. For this reason, it is necessary to define the top plane and exclude from the entire topography all these points (change the value of these points with the 10000 μm value). Thresholding criteria is based on the distribution of the heights of the points around the fitting plane. For this step, only a smaller area is

considered. As shown in *Figure 42*, the selected areas for the evaluation are smaller than the entire top surface, with a width of 10 µm. The standard deviation of the points around the fitting plane is evaluated in areas that are far from the burrs, in order to exclude the burrs in the evaluation and moreover in order to consider the roughness of the top surface in the calculation of the threshold. The threshold is fixed at a value equal to 2 times the standard deviation calculated inside these two areas.

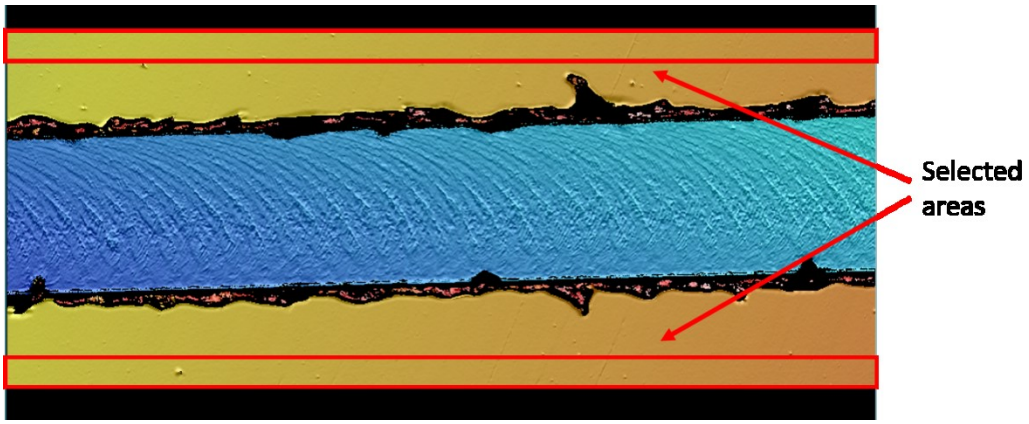

Figure 42 Area used for the thresholding procedure

In this way the pixels related to the burrs are all indexed with the value of 10000 um. Therefore, the information for the next parts of the method are acquired and extracted from the pixels that are generally defined as void pixels, so pixels without information.

At the end of the alignment step, the *xyz* point cloud is no more characterized by equi-spaced x and y values. In order to create the matrix of the height values (for the image creation) is necessary to interpolate the data. The x and y points used for the construction of the matrix are the same generally measured by the instrument (same resolution in x and y), the z matrix is constructed through linear interpolation of the z values of the point cloud. At the end of this step, the z-values are organized in a matrix.

At this point, according to the system of reference used in Figure 43, 10 different equi-spaced sections of the slot are extracted (10 sections on planes parallel to x-z plane). A second fitting is developed considering only the points of the section attached to the top plane: than the depth of the slot is evaluated according to ISO standard (ISO5436-1:2000 n.d.). In this way was possible to map the machining trajectory and check the geometrical quality of the slot. An example is shown in Figure 43, the yellow areas on the red profile are used for the fitting of the top line, then the yellow box on the blue line is used for the fitting of the bottom line. The distance between these two lines is used as an evaluation of the real depth of cut.

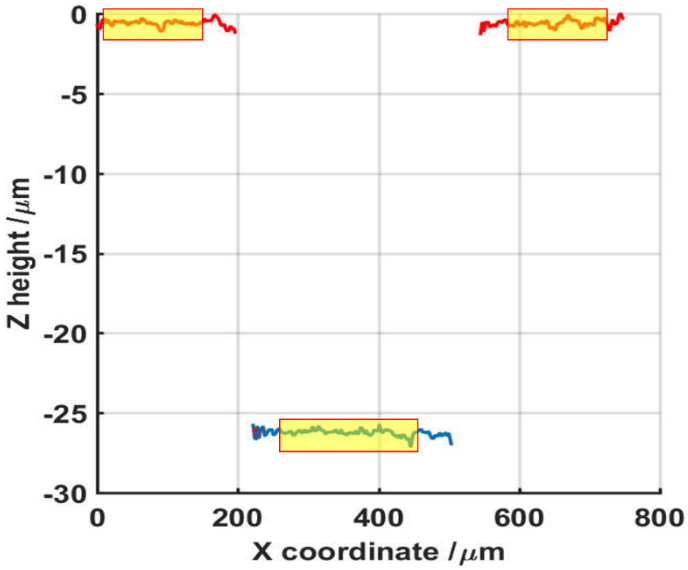

Figure 43 Example of a profile extraction and depth of cut measurement

Moreover, for each section, was also evaluated the inclination of the bottom line respect to the top line. Information on the inclination of the mill or some particular oscillation processes inside the same topography were obtained in this way.

From 3D to image

The topography is managed in order to identify the areas of the "not-measured" points. The points that are out of focus are indexed by the instrument software with high z values (10000 um). Using a Matlab routine the topography is modified in a grayscale image, in which all the not-measured points assume a completely black value and all the others points are classified as white, an example is shown in Figure 44.

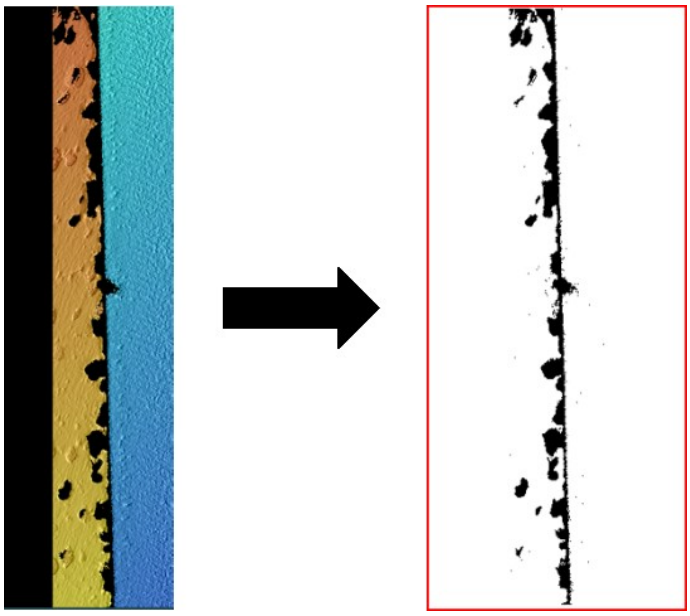

Figure 44 From 3D topography to image

In this way the topography matrix is transformed to a logical black and white image: all the subsequent steps are applied to the 2D image. On the 2D image, after the transformation all the points that are not correlate with the burrs were filtered: if there is no connection this means that the area is not related to a burr. So all the isolated areas are deleted. A preliminary filtering mask of 10x10 pixels is applied and moved on the matrix: if there is no correlation between the filtering matrix and the neighbourhood, the pixels inside the mask are ignored. A black/white conversion is applied at the end of this process. An example of this process is presented in Figure 45.

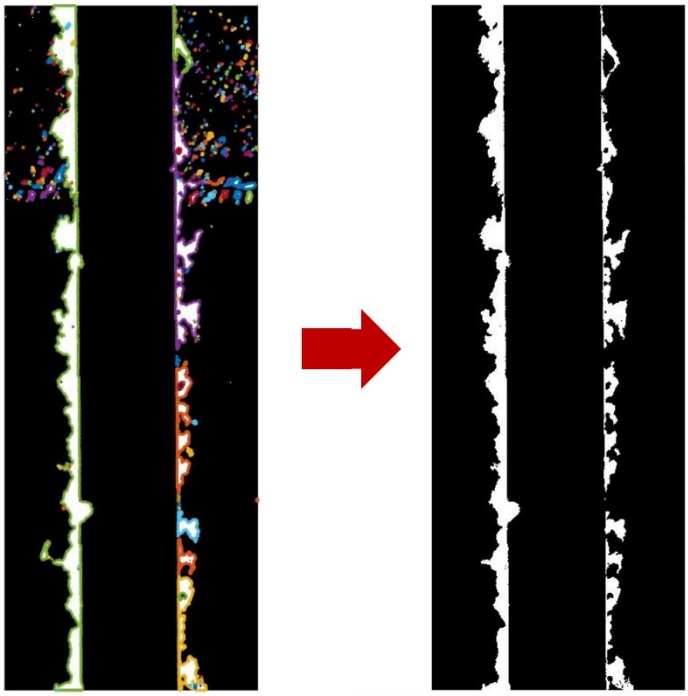

Figure 45 Extraction process: from the image to the boundary of the burr

As shown, the smaller areas that are linked to noise and not correlated to the burrs are deleted and not considered in the next steps. After this first filtering process the analysis is focused on a single burr: two different sides of the machined slot are analysed separately in order to highlight differences and problems connected with the rotation of the tool. Using boundary detection algorithm all the areas are identified: as mentioned above, only continuous area are related to the burr and the burr are identified excluding the smaller and not connected areas. The pixel area of the burr is evaluated at this step, considering the pixels inside the automatic selected boundary. All these steps are resumed in Figure 45.

The longitudinal length of the burr should also be evaluated for the computation of the burr mean area. In a rough evaluation, this length could be assumed equal to the length of the topography. But considering misalignment problem and the necessity of flexibility, an alignment of the profile is necessary, moreover for a correct evaluation of the burr longitudinal length. For these reasons is necessary to align the edge and then measure the length. Through a Canny edge detection algorithm, the boundary of the burr is identified and extracted from the image. At this point the first need is to split the two different profile, the one related to the burr and the one related to the machined edge (profile used for the alignment), result of this thresholding procedure is presented in Figure 46.

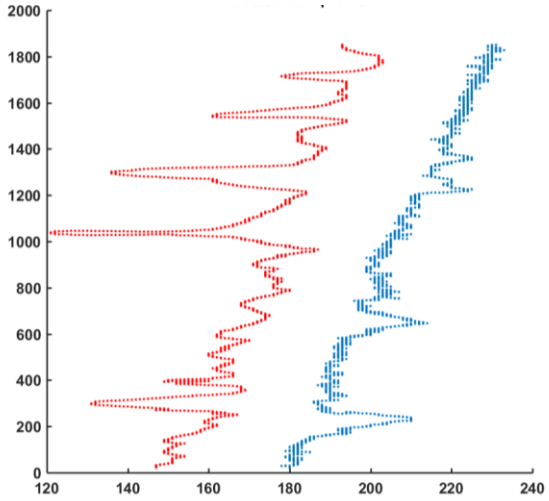

Figure 46 Profile splitting

Using this method is possible to analyze directly the burr that is curved inside the slot and moreover and mainly the burr that is outside the machined slot.

From this point all the post process is applied to the profiles, considering them as 1D profiles. The first step is based on a preliminary alignment based on a least square polynomial fitting on the reference profile. The roto-translation matrix is constructed starting from this fit (considering the rotation associated to the angular coefficient and the translation). The first fit is based on all the data point of the reference line (the blue line in Figure 47).

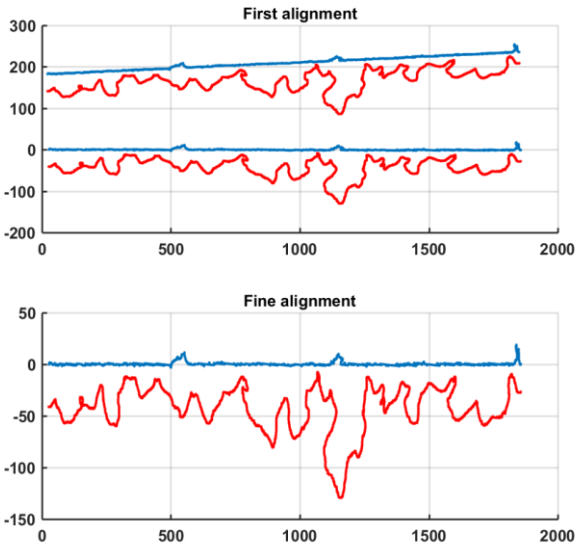

Figure 47 Burr profile alignment

After the first rough alignment a second fine alignment is applied. In this case only a selected number of points is used for the alignment of the reference line: a threshold is applied in order to exclude the points of the reference that are part of the internal burr. A threshold based on the standard deviation of the points around the polynomial fitting line is applied using a factor 2. Only the points inside the band ±2s are considered.

A second polynomial fitting on this selected number of points is applied and the roto-translation matrix is evaluated and used for the fine alignment. After the fine alignment the burr profile and the reference profile are used for the evaluation of the length (burr profile in the bottom part of Figure 47).

Application to a test case

The micro-milling experiments were carried out on a high-precision 5-axis micro-milling centre Kugler™. The machine is equipped with air-bearing spindle that can reach up to 180000 RPM. The thermal extension of the spindle axis is measured by built-in eddy current sensor and is compensated in real time.

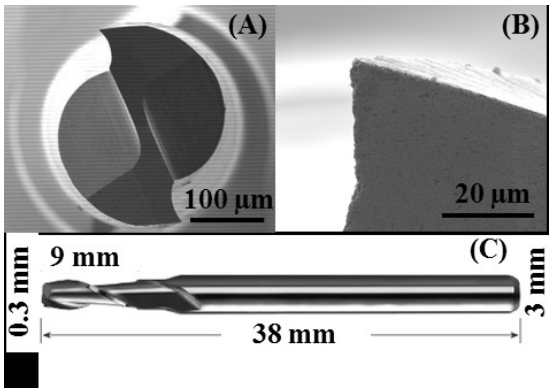

Figure 48 Tool geometry

Two fluted flat-end-square, uncoated, tungsten carbide tools (Kyocera – solid round – square end mill – series 1610) were used for all the experiments (*Figure 48* shows the geometry of the tool). Each tool was checked through SEM observations before machining to evaluate any possible imperfection. In order to highlight the sensitivity of the method to the different machining processes, 2 different studies were developed. A first preliminary study (published in 2017 (Medeossi et al. 2017)) on four different slots was developed to verify the sensitivity of the process to the cutting speed and feed per tooth parameter, the cutting speed and the feed, maintaining constant the depth of cut. For the experiments rough Titanium was chosen.

This preliminary study was developed acquiring one single image for each machined slot.

A second and more extensive campaign was developed considering 27 different slots, combining all the machining parameters, adding the effect of the depth of cut on the burrs evaluation. The last study was developed in order to map the trend of the burrs during the wear of the tool. In this last campaign, the machining process was stopped only at the broken phase of the tool. The first preliminary study was used in order to qualitatively understand if the new approach was sensitive enough to the burr changings, on the contrary in the second campaign the results obtained from the confocal instrument were compared with the SEM images, in order to qualitatively understand if the absolute values of the newly developed method are good enough. In the last campaign, the study was developed in order to map the wear of the tool, and try to verify if the burr could be used as an indicator of the wear of the tool. Every different experiment will be discussed in the following part.

In the first campaign the full immersion slotting was applied as machining strategy; the radial depth of cut corresponded to the tool diameter and the axial depth of the cut was set constant for all the experiments and equal to 30 μm, which is a suitable value for semi-finishing/finishing cutting. The machining was carried out under dry cutting conditions, and compressed air was sprayed on the tool and into the slot to facilitate the chips removal. The cutting parameters are listed in Table 11: different cutting speed and different feed per tooth were applied to obtain different burr morphology.

Sample number	Cutting speed [m/min]	Feed per tooth [μm/tooth]	Depth of cut [μm]
4	60	0.5	30
3	150	0.5	30
1	60	1.5	30
2	150	3	30

Table 11 Cutting parameters of the analyzed slots

To verify the sensitivity of the method an experimental campaign was developed in order to analyse the area of the burrs obtained in micro milling. Different cutting conditions were applied and different burrs profiles were obtained. A Sensofar Confocal microscopy was used for the evaluation with a 20x objective magnification. To evaluate the burrs on a representative area, and both the sides of the slot, a 4x1 topography stitching matrix was evaluated. Stitching algorithm is based on a x, y and z distance minimization. The method was applied on 4 different slots.

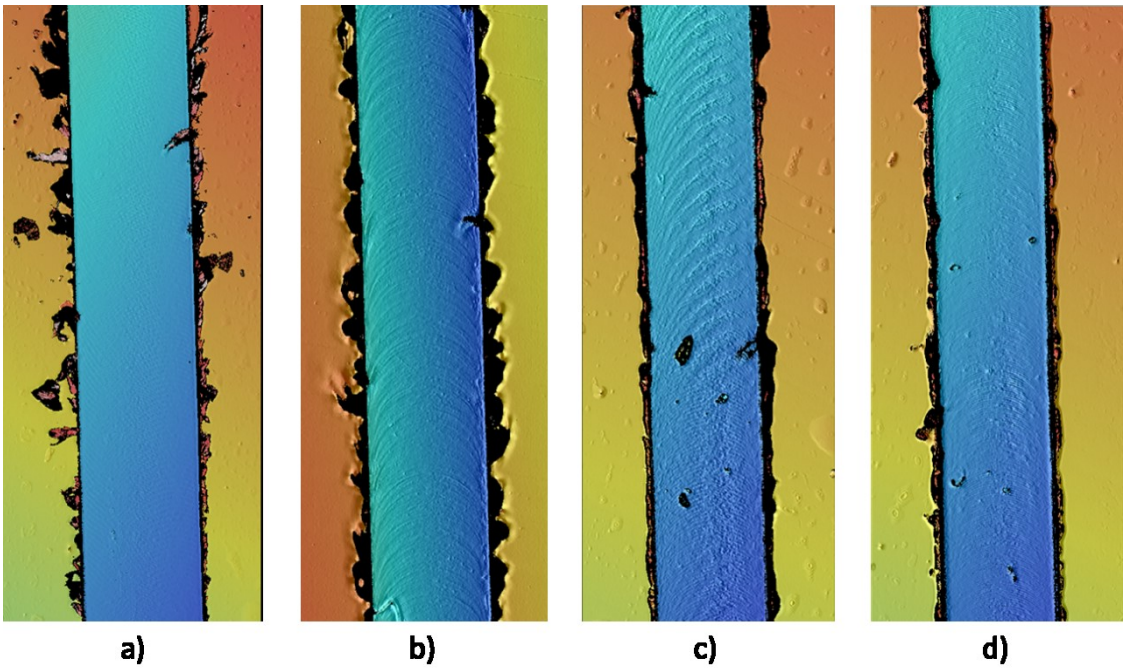

Figure 49 Acquisition results: a) sample 1, b) sample 2, c) sample 3 and d) sample 4

The topography gives to the user all the information regarding the bottom surface and top surface, nevertheless on the burrs the measured points are not enough for any kind of evaluation. Figure 49 shows the 2D view of the topographies in order to highlight the differences in terms of morphology between all the machined slots. The 3D data are then used in a Matlab script for topography alignment (as described in the previous part) and then transformed in images. After the run of the previously described procedure the obtained left-burrs profiles are compared in Figure 50. All the profiles are aligned using the internal profile (0 reference in Figure 47 is the fitting line used for alignment).

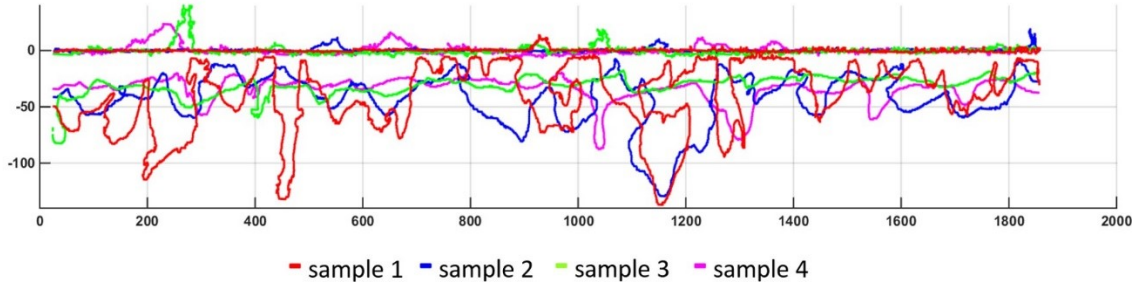

Figure 50 Comparison of the four different burr profiles

After the isolation of the burr profile is clear that the morphology in these four cases is slightly different. Sample number 3 is characterized by a distributed burr, no isolated peaks and no segmentation. Sample number 4 is more segmented and presents three high peaks. Moreover samples 2 and 1 are strongly characterized by huge peaks and a clear

segmentation. All the qualitative evaluations done are confirmed by the numerical evaluation. Table 12 shows the results: all the information are obtained automatically, applying the previously presented procedure.

	Burrs				**Roughness**	**Geometry**
Sample	Mean width [µm]	Maximum external peak [µm]	Ratio [%]	Maximum internal peak [µm]	Ra [µm]	Depth [µm]
1	43	137	31	14	0.117	25.6
2	46	129	35.2	19	0.051	22.0
3	33	82	40	40	0.234	29.6
4	37	87	42.6	24	0.162	29.5

Table 12 Parameters evaluation

Difference between sample 1 and sample 2 in terms of segmentation are confirmed by the numbers reported in table 3: the maximum external peak of the sample number 1 is higher than sample number 2, but on the contrary the mean width is lower and moreover is lower the ratio. This is a confirmation of the higher segmentation of the burrs of sample number 1 respect sample number 2. In these cases the mean burr width is not changing drastically, because of the cutting parameters. As a preliminary study, depth of cut was not changed. In order to generate a variation in the width of the burrs, the depth of cut is also changed in the second experimental campaign. In this first campaign not clear correlation between the machining parameters and the parameters were find, and this is qualitatively confirmed by the topography images.

In the second study, different combinations of machining parameters were analysed. The machining parameters used in this case are resumed in table Table 13. For each machining condition, three different slots were machined in order to verify the repeatability and the reliability of the burrs evaluation method.

Group	Cutting speed (m/min)	Feed per tooth (µm/th)	Depth of cut (µm)
1	50	1	30
2	50	1,5	60
3	100	1	60
4	50	2	90
5	100	1,5	90
6	100	2	30
7	150	1	90
8	150	1,5	30
9	150	2	60

Table 13 Cutting parameters for the second experimental campaign

Every single slot was measured in 5 different fixed positions, in order to verify the evaluation of the burrs and moreover the reliability of the method. Therefore, this means that for each group a total of 3 slots and 5 different positions for each slots are analysed. In the next part every single group will be analysed separately, then the entire results will be compared and verified. Only one single slot per group is presented completely, with the topographies and SEM images. Separately are analysed the down and up milling burrs (see Figure 51 as example). Taking as an example the images of the 3 slots of the group 1 (shown in Figure 52), the left image of the SEM is the down milling side and the correspondent side in the confocal image is the top one. The SEM sections were taken in an area as close as possible to the final side of the topographies (in Figure 52 the right edge of the topography images).

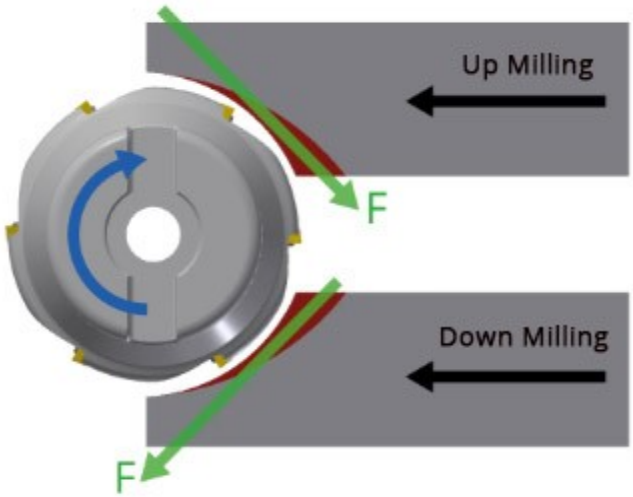

Figure 51 Up and Down milling side of the machined sample

In Table 14, Table 15, Table 16 are resumed the results for the group 1: roughness, burrs and real depth of cut. The roughness values shown in Table 16 were obtained as a mean on 3 different profiles for each different section. Only the average value are shown in the next tables.

Table 14 shows the burrs mean width for the 5 different sections and for both up and down milling sides.

	Section 1		Section 2		Section 3		Section 4		Section 5	
	UP	DOWN	UP	DOWN	UP	DOWN	UP	DOWN	UP	DOWN
1	24,7	41,5	17,5	36,4	16,7	45,2	18,4	53,9	20,5	53,5
2	15,3	30,1	13,0	38,4	15	57,4	14,6	44,6	25,5	46,8
3	24,6	29,4	18,7	44,2	16,8	43,1	13,9	37,5	23,1	46,2

Table 14 Burr mean width results obtained for group 1

Table 15 shows the depth of cut for the 5 different sections. Values reported in table are the average of the 10 different profiles extracted from each topography.

Sample	Section 1	Section 2	Section 3	Section 4	Section 5
1	26,2	30,4	30,9	31,3	30,7
2	24,9	28,9	29,4	29,9	30,3
3	24,3	28,3	28,7	28,8	29,6

Table 15 Real depth of cut results obtained for group 1

The images obtained through the SEM and the Confocal microscope are shown in Figure 52. In order to qualitatively compare the results of the newly developed method and the SEM only one section is reported (section number 1)

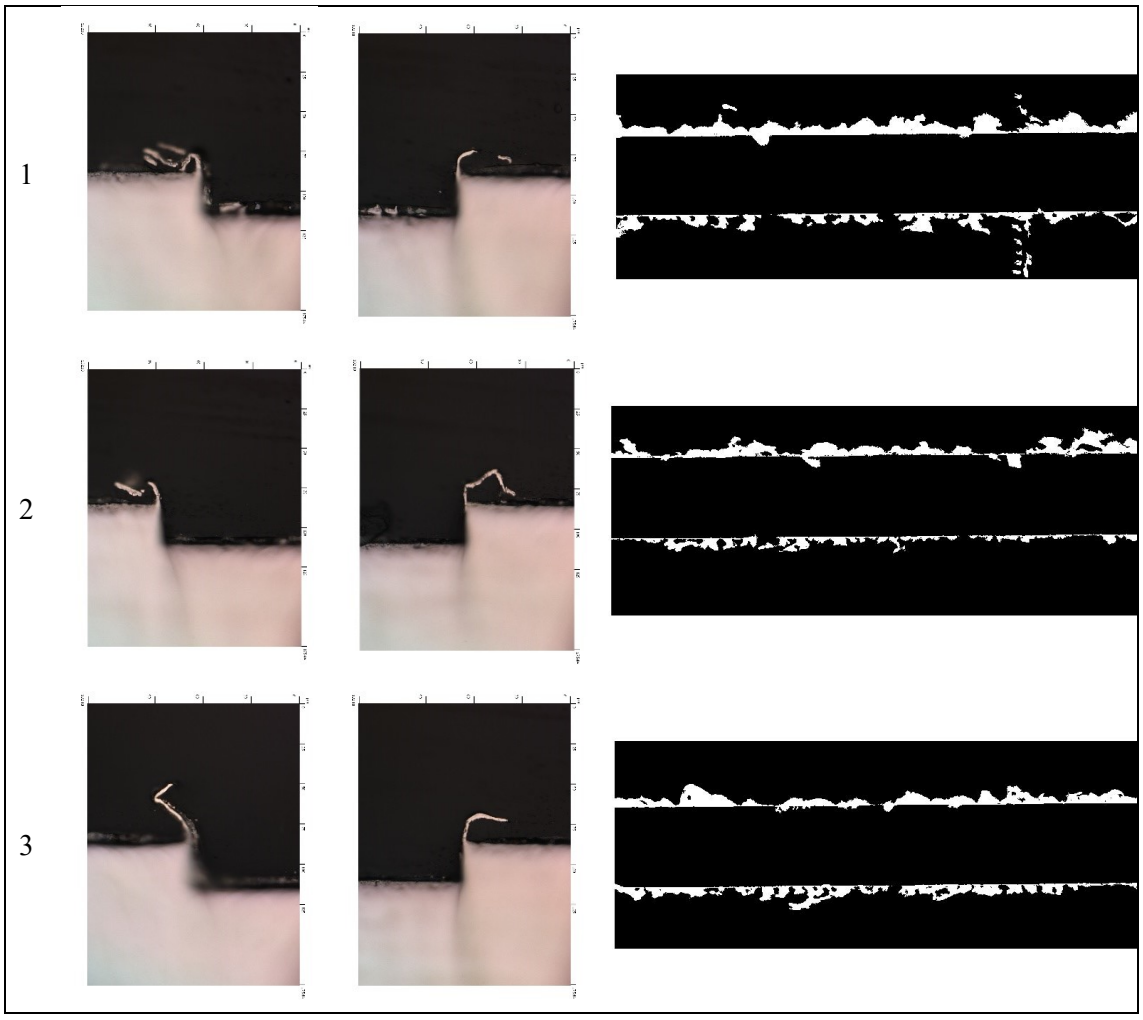

Figure 52 Sem images and topography images of group 1

Finally, for group 1, the surface parameters are shown in Table 16.

Parameters	Sample 1		Sample 2		Sample 3	
	Avg [um]	Standard dev [um]	Avg [um]	Standard dev [um]	Avg [um]	Standard dev [um]
Rz	0,7136	0,399	0,6847	0,193	0,5590	0,038
Ra	0,1013	0,004	0,1076	0,003	0,1521	0,077
Rq	0,1377	0,012	0,1380	0,006	0,1176	0,002

Table 16 Roughness results obtained for group 1

Considering the results obtained for the quantification of the burrs, and a qualitatively evaluation of the trend in the images, it is clear that the values are coherent both with the images and with the SEM measurements. The burrs on the Down milling side are constantly bigger than the up-milling ones. The depth of cut is variable, because of the effect of the first section, exit section of the mill.

The group 2 is characterized by a different feed per tooth and a different nominal depth of cut (go to *Table 13*). The results for burrs mean width are shown in *Table 17*. *Table 18* shows the real depth of cut.

	Section 1		Section 2		Section 3		Section 4		Section 5	
	UP	DOWN	UP	DOWN	UP	DOWN	UP	DOWN	UP	DOWN
4	27,8	43,6	48,8	55,3	44,0	63,9	39,8	60,8	28,0	49,7
5	22,7	32,3	30,5	33,8	35,1	40,3	33,3	39,4	41,4	45,9
6	32,9	31,7	42,6	25,2	38,9	30,5	24,2	37,8	39,0	34,1

Table 17 Burr mean width results obtained for group 2

Sample	Section 1	Section 2	Section 3	Section 4	Section 5
4	56,7	60,6	60,9	60,7	61,5
5	56,7	60,6	60,8	60,7	61,4
6	56,5	60,2	60,5	60,5	60,9

Table 18 Real depth of cut results obtained for group 2

The SEM images and the topography images after image creation are shown in Figure 53.

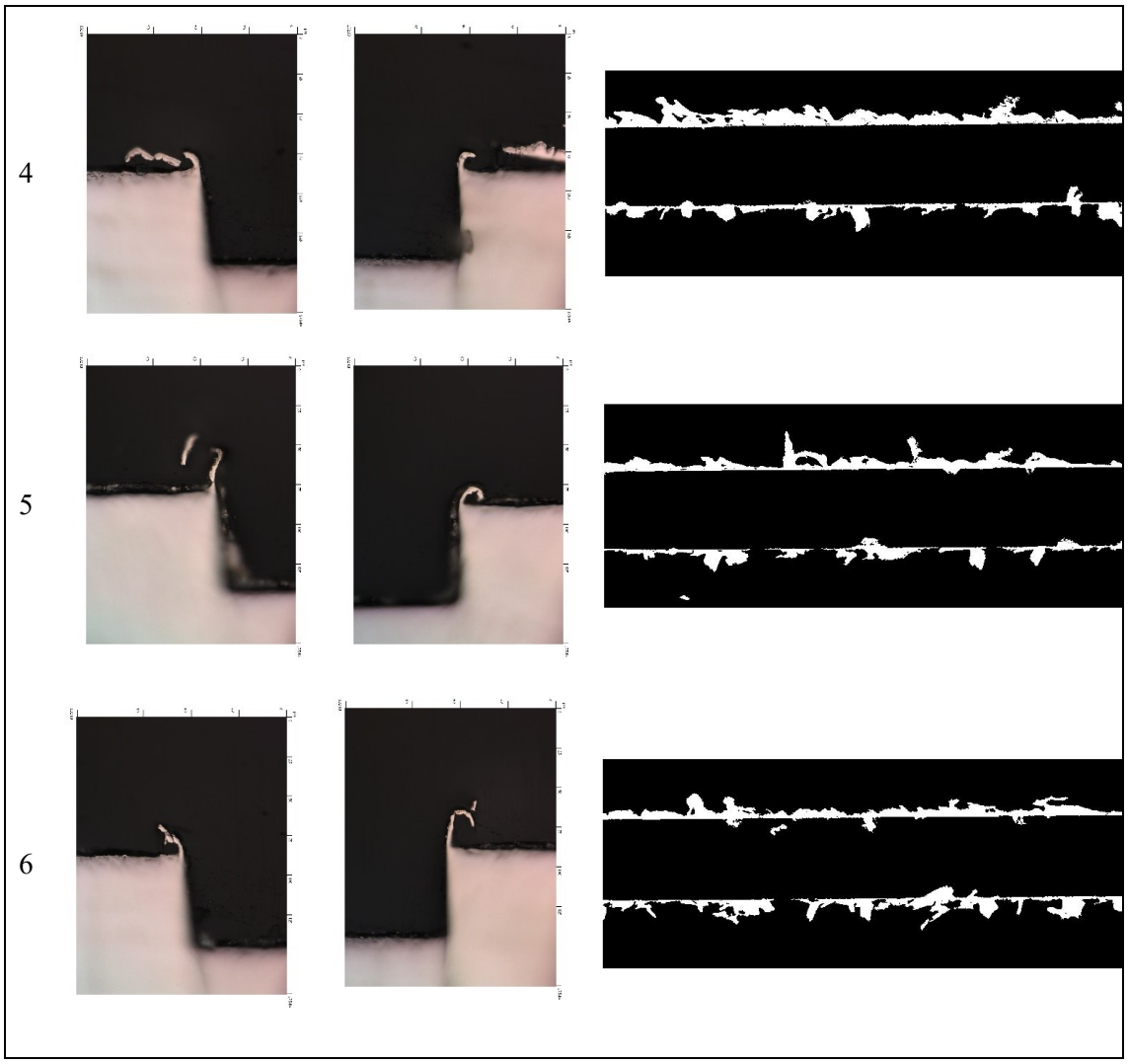

Figure 53 Sem images and topography images of group 2

The surface roughness of the bottom surface of the group 2, characterized by a feed per tooth of 1,5 and a depth of cut of 60 is reported in Table 19

Parameters	Sample 4		Sample 5		Sample 6	
	Avg [um]	Standard dev [um]	Avg [um]	Standard dev [um]	Avg [um]	Standard dev [um]
Rz	0,836	0,501	0,766	0,112	0,773	0,164
Ra	0,136	0,010	0,129	0,002	0,130	0,004
Rq	0,175	0,018	0,165	0,004	0,165	0,007

Table 19 Roughness analysis results obtained for group 2

The third group is characterized by an increment in the cutting speed (100 m/min). Depth of cut and feed per tooth are maintained constant and equal to group 2.

	Section 1		Section 2		Section 3		Section 4		Section 5	
	UP	DOWN	UP	DOWN	UP		UP	DOWN	UP	DOWN
1			34,3	136,7	30,6	149,8	23,8	114,5	31,8	102,9
2	34,5	64,3	22,8	65,0	36,8	70,4	32,3	89,5	40,5	63,6
3	37,7	69,0	29,5	73,7	29,9	75,9	29,0	75,3	33,0	72,2

Table 20 Burr mean width results obtained for group 3

Sample	Section 1	Section 2	Section 3	Section 4	Section 5
1		61	60,9	61	61,7
2	55,6	59,1	59,1	58,7	59,3
3	56,6	58,9	58,8	58,6	59

Table 21 Real depth of cut results obtained for group 3

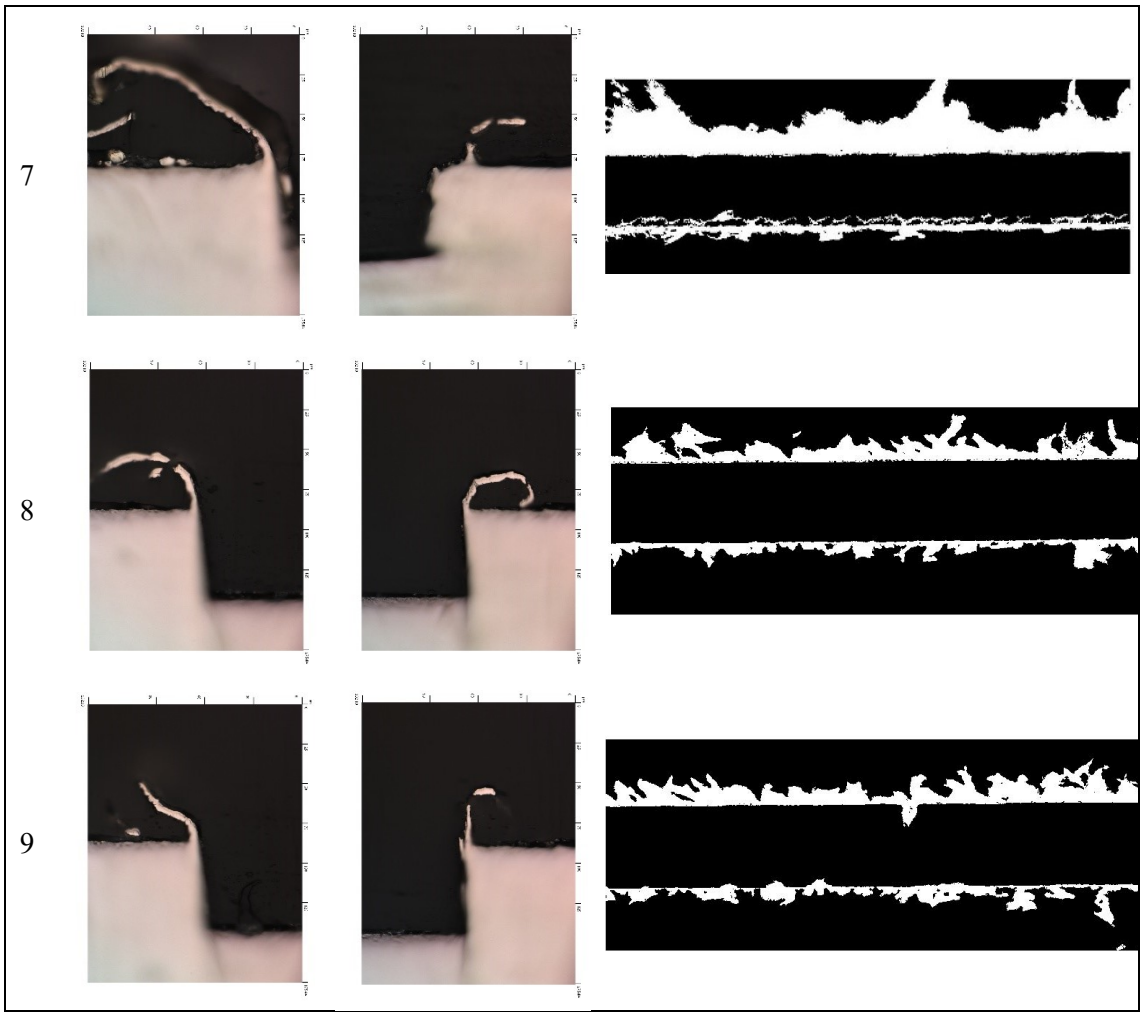

Figure 54 Sem images and topography images of group 3

Parameters	Sample 7		Sample 8		Sample 9	
	Avg [um]	Standard dev [um]	Avg [um]	Standard dev [um]	Avg [um]	Standard dev [um]
Rz	0,533	0,386	0,611	0,034	0,690	0,067
Ra	0,108	0,018	0,103	0,001	0,115	0,002
Rq	0,131	0,025	0,132	0,001	0,148	0,003

Table 22 Roughness analysis results obtained for group 3

The fourth group is different for each parameter: feed per tooth is 2, cutting speed is reduced to 50 and depth of cut is the maximum one (90µm).

	Section 1		Section 2		Section 3		Section 4		Section 5	
	UP	DOWN	UP	DOWN	UP		UP	DOWN	UP	DOWN
1	56,7	75,0	79,2	87,9	68,6	89,4	81,1	89,1	72,7	91,8
2	56,9	76,2	70,6	86,7	61,5	81,3	43,9	100,1	70,7	99,7
3	19,6	84,9	44,2	88,0	45,0	97,5	53,3	98,4	70,7	84,7

Table 23 Burr mean width results obtained for group 4

Sample	Section 1	Section 2	Section 3	Section 4	Section 5
1	87,2	90,7	90,3	90,7	91
2	87,0	90,5	90,1	90,3	90,9
3	87,2	91,1	90	90,5	90,4

Table 24 Real depth of cut results obtained for group 4

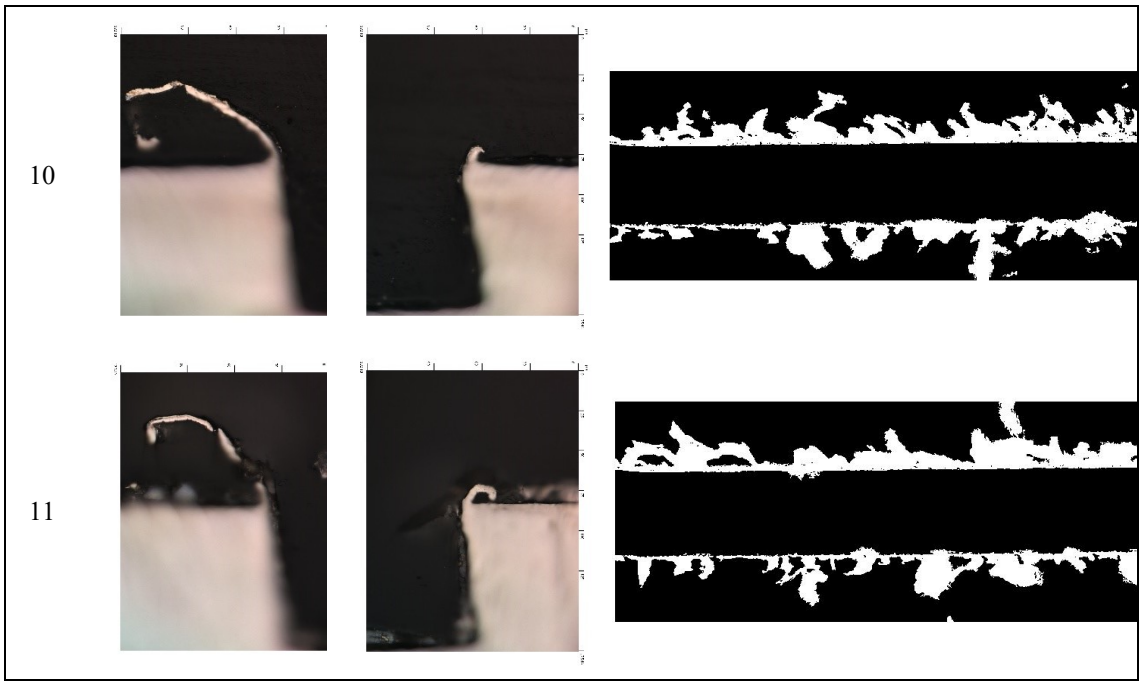

12

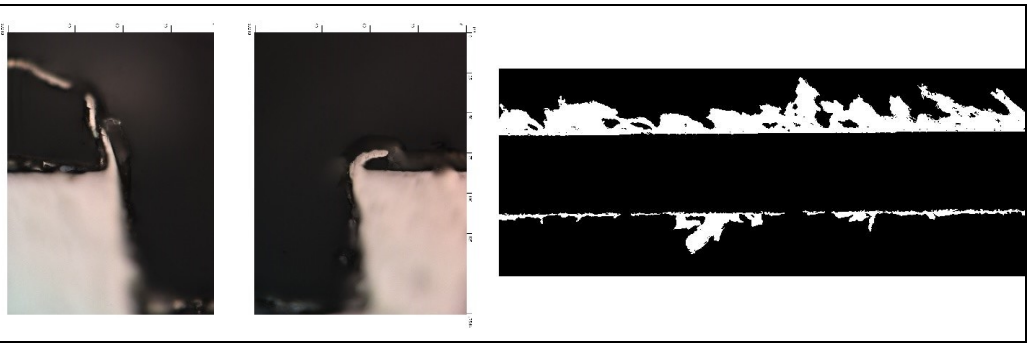

Figure 55 Sem images and topography images of group 4

As clearly described from the last image, the burrs are qualitatively bigger then the previous machining conditions. Because of the depth of cut down milling burrs are increasing a lot. The most interesting image is the one representing the sample number 3 of this group. In this case the up-milling burrs are really small, and it's clearly confirmed by the SEM image and moreover the confocal image and the mean width calculated (19,6 μm).

Parameters	Sample 10		Sample 11		Sample 12	
	Avg [um]	Standard dev [um]	Avg [um]	Standard dev [um]	Avg [um]	Standard dev [um]
Rz	0,888	0,142	0,862	0,057	0,810	0,043
Ra	0,155	0,004	0,156	0,001	0,143	0,002
Rq	0,196	0,006	0,194	0,002	0,178	0,002

Table 25 Roughness analysis results obtained for group 4

The fifth group is characterized by a feed per tooth of 1,5 and a cutting speed of 50. The depth is maintained constant at a value of 90 μm.

	Section 1		Section 2		Section 3		Section 4		Section 5	
	UP	DOWN	UP	DOWN	UP		UP	DOWN	UP	DOWN
1	60,7	71,0	74,6	67,3	60,6	70,2	56,8	80,4	69,7	71,4
2	48,7	68,4	78,6	82,9	80,2	70,3	51,9	77,1	94,6	63,9
3	54,1	70,6	71,4	69,7	82,7	72,2	93,6	78,8	43,8	104,0

Table 26 Burr mean width results obtained for group 5

Sample	Section 1	Section 2	Section 3	Section 4	Section 5
1	87,3	90,7	90,1	90,2	90,1
2	87,2	90,5	90,1	90,2	90,1
3	87,8	89,8	89,9	90,2	90,2

Table 27 Real depth of cut results obtained for group 5

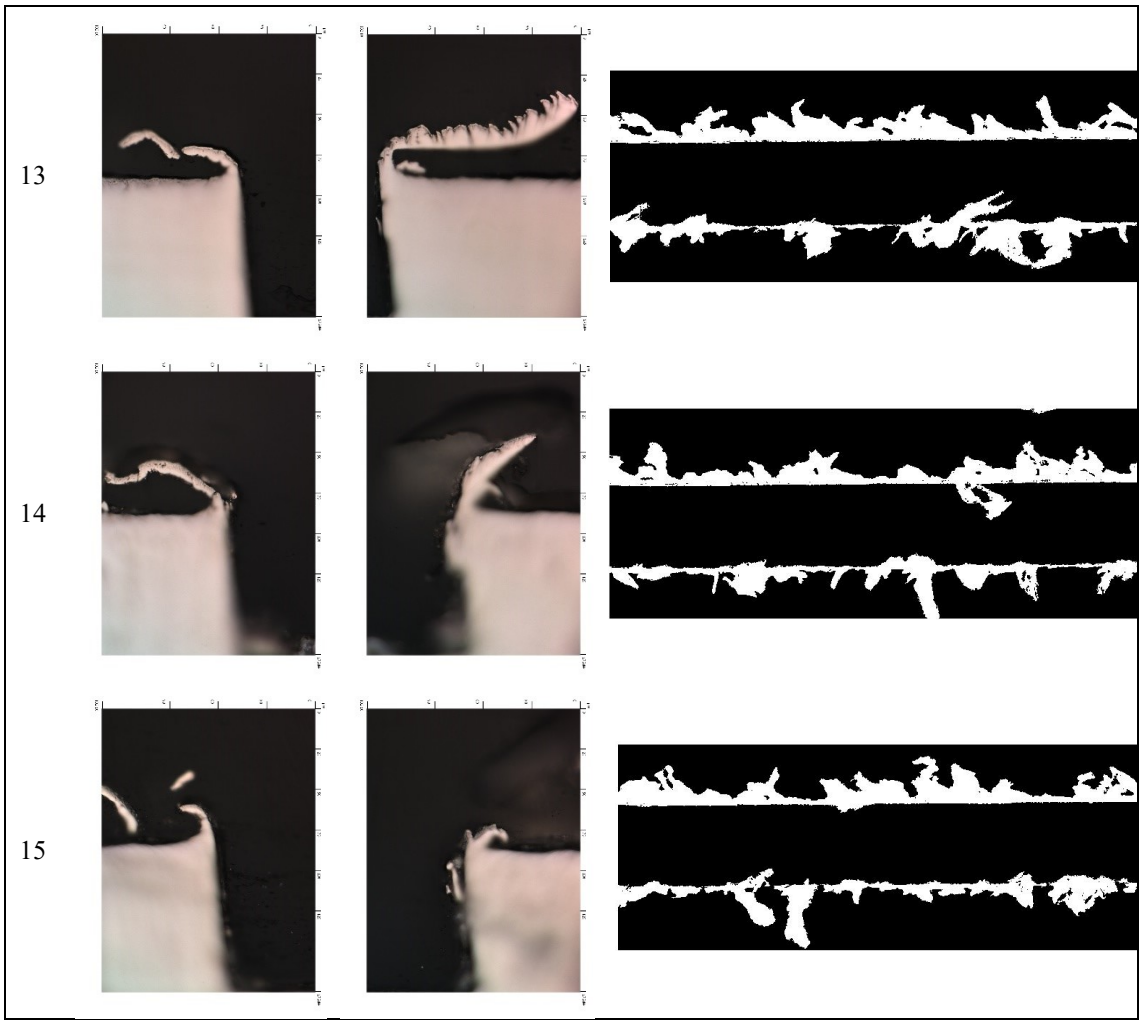

Figure 56 Sem images and topography images of group 5

In this case the values of the burr width are more similar for up and down milling edge. This is described by the images and moreover from the burr width parameter.

Parameters	Sample 13		Sample 14		Sample 15	
	Avg [um]	Standard dev [um]	Avg [um]	Standard dev [um]	Avg [um]	Standard dev [um]
Rz	0,758	0,062	0,782	0,140	0,768	0,079
Ra	0,152	0,002	0,159	0,005	0,153	0,002
Rq	0,181	0,003	0,189	0,007	0,184	0,003

Table 28 Roughness analysis results obtained for group 5

In the group number 6 the depth of cut is reduced to 30 μm. Feed per tooth is changed to 2.

	Section 1		Section 2		Section 3		Section 4		Section 5	
	UP	DOWN	UP	DOWN	UP		UP	DOWN	UP	DOWN
1	17,1	34,2	19,0	34,2	20,9	49,3	20,8	31,6	18,5	45,2
2	18,4	35,4	24,0	32,9	20,3	28,5	30,2	35,9	22,9	41,1
3	21,6	27,2	27,0	28,4	28,8	34,9	27,9	35,5	24,7	43,1

Table 29 Burr mean width results obtained for group 6

Sample	Section 1	Section 2	Section 3	Section 4	Section 5
1	25,5	28,3	28,2	28,4	28,9
2	24,5	27,3	27	27,1	27,8
3	23,9	26,8	26,7	26,5	26,9

Table 30 Real depth of cut results obtained for group 6

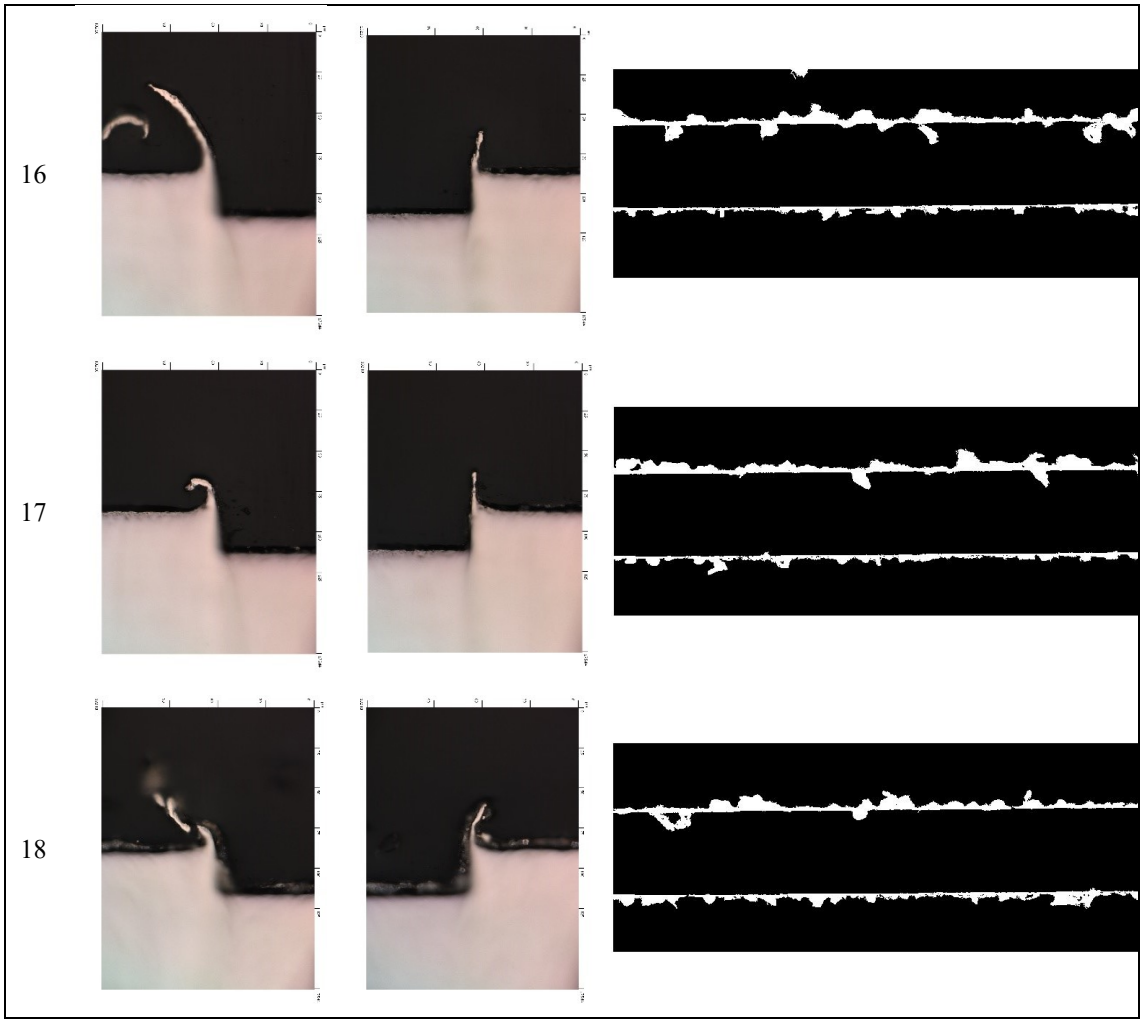

Figure 57 Sem images and topography images of group 6

Back to small values of depth of cut cause small down milling burrs respect to the up milling.

Parameters	Sample 16		Sample 17		Sample 18	
	Avg [um]	Standard dev [um]	Avg [um]	Standard dev [um]	Avg [um]	Standard dev [um]
Rz	0,793	0,186	0,828	0,147	0,902	0,135
Ra	0,186	0,079	0,147	0,007	0,152	0,003
Rq	0,162	0,004	0,181	0,009	0,191	0,005

Table 31 Roughness analysis results obtained for group 6

The seventh group is characterized by a cutting speed of 150, a feed per tooth of 1 and a depth of cut of 90um. As described in table, the values obtained for the burrs are bigger than the previous machining conditions.

	Section 1		Section 2		Section 3		Section 4		Section 5	
	UP	DOWN	UP	DOWN	UP		UP	DOWN	UP	DOWN
1	118	61	161	62,4	128	73	124	73	122	62
2	104	119	142	107,1	125	85	139	100	157	74
3	106	106	130	124,4	130	84	154	121	141	121

Table 32 Burr mean width results obtained for group 7

Sample	Section 1	Section 2	Section 3	Section 4	Section 5
1	86,9	89,8	89,8	89,7	89,9
2	87	90,0	89,3	90	89,9
3	86,5	89,2	89,2	89,5	89,6

Table 33 Real depth of cut results obtained for group 7

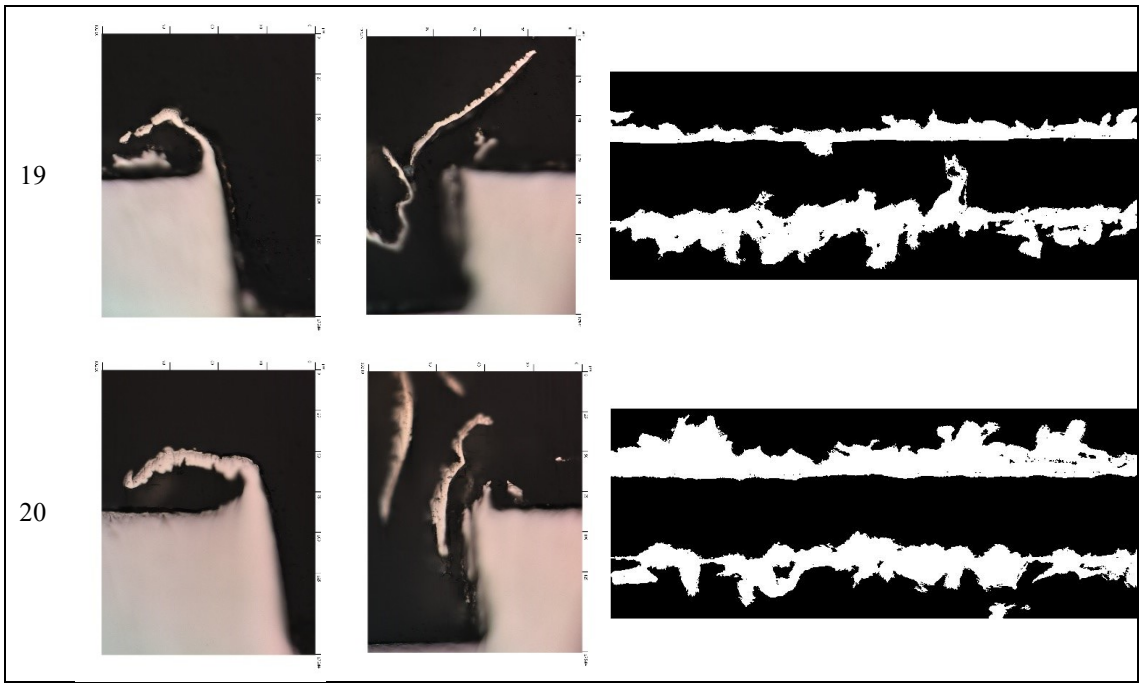

21

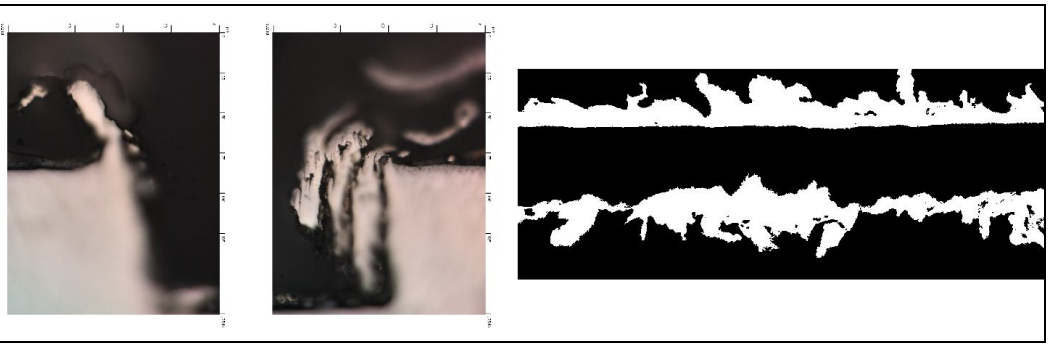

Figure 58 Sem images and topography images of group 7

This combination of parameters causes the bigger burrs. The combination of high cutting speed and high depth of cut causes burrs both in the up and down milling side.

Parameters	Sample 19		Sample 20		Sample 21	
	Avg [um]	Standard dev [um]	Avg [um]	Standard dev [um]	Avg [um]	Standard dev [um]
Rz	0,733	0,057	0,790	0,124	0,803	0,249
Ra	0,119	0,001	0,129	0,001	0,130	0,004
Rq	0,157	0,002	0,172	0,001	0,172	0,009

Table 34 Roughness analysis results obtained for group 7

The eight group is reducing the depth of cut and also the feed per tooth.

	Section 1		Section 2		Section 3		Section 4		Section 5	
	UP	DOWN	UP	DOWN	UP		UP	DOWN	UP	DOWN
1	24,5	33,3	21,0	56,5	16,1	34,5	21,7	41,1	24,1	43,4
2	22,8	36,3	21,0	42,5	53,6	39,9	46,5	45,6	39,6	43,8
3	21,3	42,3	37,8	41,3	36,3	45,3	24,9	44,1	38,1	43,7

Table 35 Burr mean width results obtained for group 8

Sample	Section 1	Section 2	Section 3	Section 4	Section 5
1	26,8	29,4	28,7	28,8	29,4
2	26,5	28,9	28,4	28,6	28,6
3	26,5	28,6	28,1	28,2	28,8

Table 36 Real depth of cut results obtained for group 8

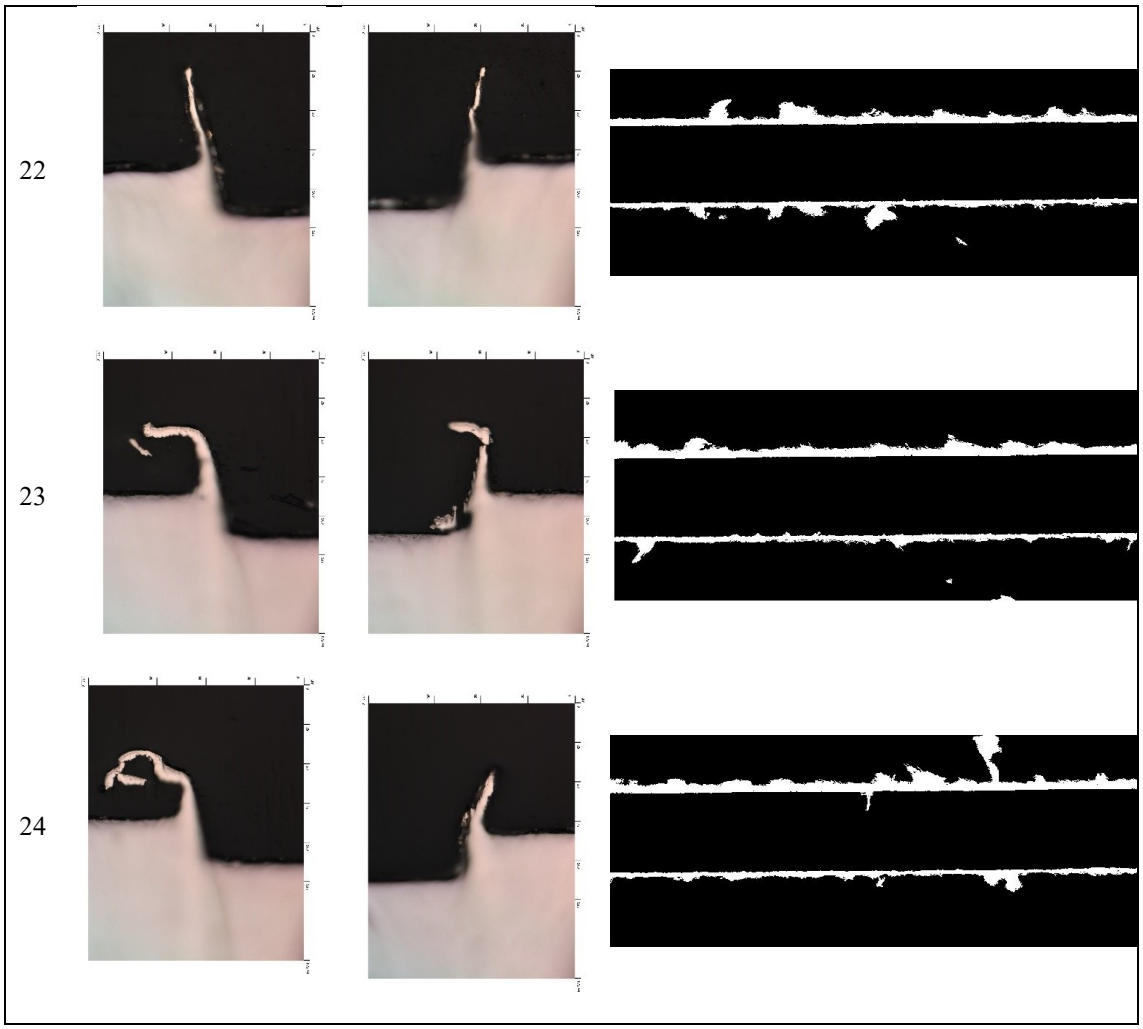

Figure 59 Sem images and topography images of group 8

Reducing the depth of cut causes a reduction of the burrs width.

Parameters	Sample 22		Sample 23		Sample 24	
	Avg [um]	Standard dev [um]	Avg [um]	Standard dev [um]	Avg [um]	Standard dev [um]
Rz	0,462	0,052	0,484	0,024	0,437	0,041
Ra	0,073	0,001	0,080	0,001	0,072	0,001
Rq	0,095	0,002	0,103	0,001	0,092	0,001

Table 37 Roughness analysis results obtained for group 8

The ninth group is changing the depth of cut to 60 um and the feed per tooth to 2.

	Section 1		Section 2		Section 3		Section 4		Section 5	
	UP	DOWN	UP	DOWN	UP		UP	DOWN	UP	DOWN
1	65,3	54,4	72,9	62,8	69,8	60,3	38,4	67,6	35,8	36,2
2	89,1	90,4	110,9	104,4	81,8	77,0	73,3	69,8	92,8	66,8
3	81,7	80,3	118,5	80,0	103,4	83,6	101,8	63,2	97,9	93,6

Table 38 Burr mean width results obtained for group 9

Sample	Section 1	Section 2	Section 3	Section 4	Section 5
1	57,8	60,4	59,7	59,8	60,6
2	58,2	60,8	59,6	60	60,3
3	58,3	60,9	59,7	60,2	60,1

Table 39 Real depth of cut results obtained for group 9

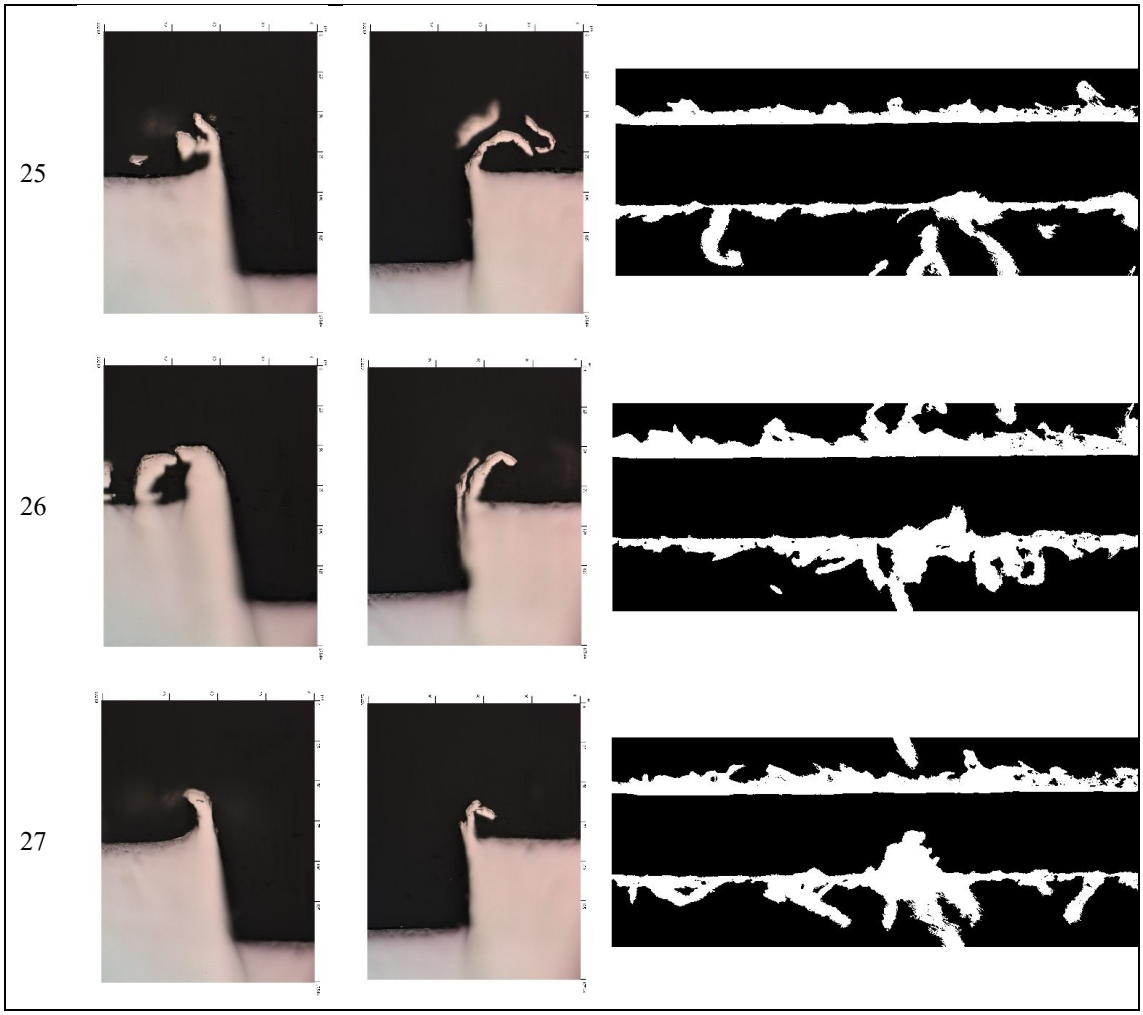

Figure 60 Sem images and topography images of group 9

Parameters	Sample 22		Sample 23		Sample 24	
	Avg [um]	Standard dev [um]	Avg [um]	Standard dev [um]	Avg [um]	Standard dev [um]
Rz	0,473	0,087	0,410	0,107	0,501	0,094
Ra	0,077	0,002	0,070	0,002	0,084	0,002
Rq	0,098	0,003	0,087	0,004	0,106	0,004

Table 40 Roughness analysis results obtained for group 9

In order to compare the final results, the mean value were considered in each group. Inside each group and moreover considering the 5 different section, the values of the burrs width are pretty constant and correlated with the machining conditions. In order to highlight the relations between the cutting parameters and the burrs width, the scater plot of the results

are presented in the next figures. On the left side of each figure is reported the up-milling edge, then on the right side is presented the down milling side of the slot.

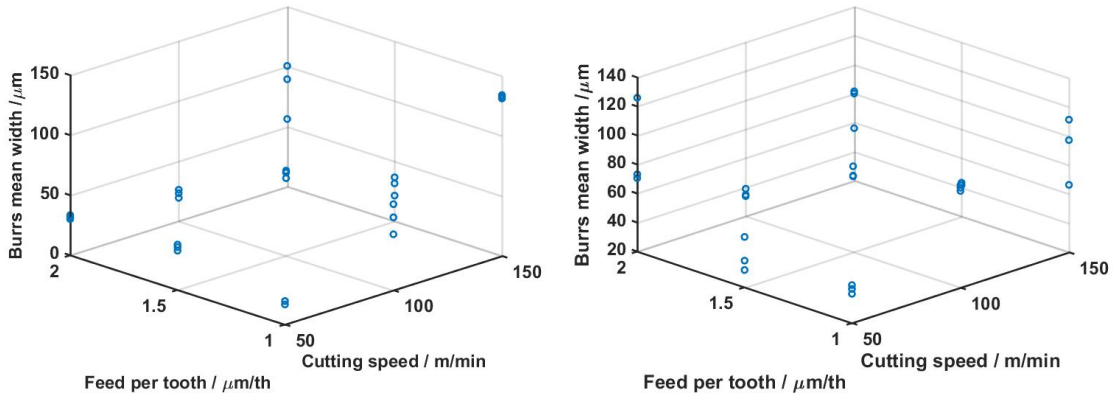

Figure 61 Variation of the burrs mean width in function of the feed per tooth and cutting speed. On the left side the up-milling edge and on the right side the down-milling edge

Figure 61 shows the correlation between the cutting speed and the feed per tooth for both the up-milling and down-milling edges. From these scatter plots is evident that there is no clear relation between the mean burr width and these cutting parameters.

An unclear correlation is also shown in Figure 62: the relation between feed per tooth, depth of cut and mean burr width is not clearly shown. With small feed per tooth, in both cases, up-milling and down-milling, the depth of cut is influencing the burr mean width. This effect is not confirmed increasing the feed per tooth.

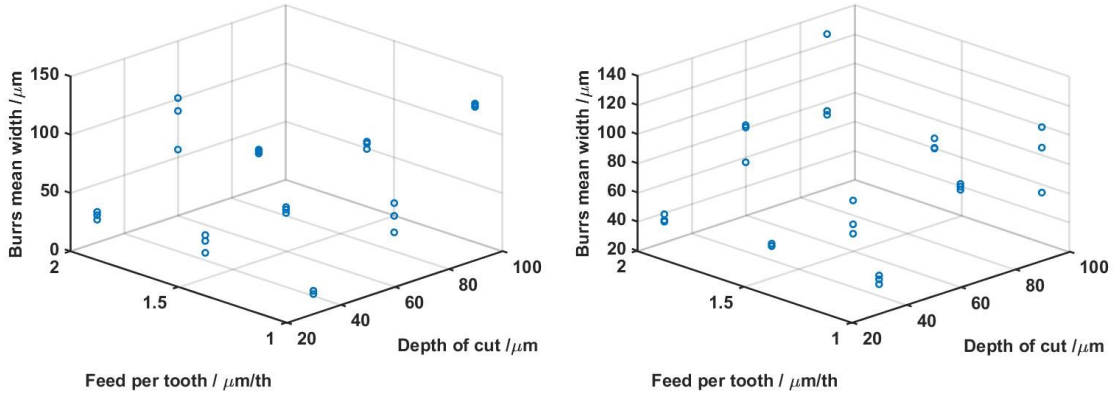

Figure 62 Variation of the burrs mean width in function of the feed per tooth and depth of cut. On the left side the up-milling edge and on the right side the down-milling edge

Finally Figure 63 shows the relation between the cutting speed, depth of cut and mean burr width. The down-milling edge is also influenced by these two parameters. Mean burr width is following the depth of cut increase in the case of high cutting speed (150m/min). In both cases the depth of cut is influencing the burr width. Increasing the depth of cut

cause an increment of the burr width. Moreover the same effect is produced by the increase of the cutting speed. The combination of cutting speed and depth of cut is clearly causing a huge increment of burrs width.

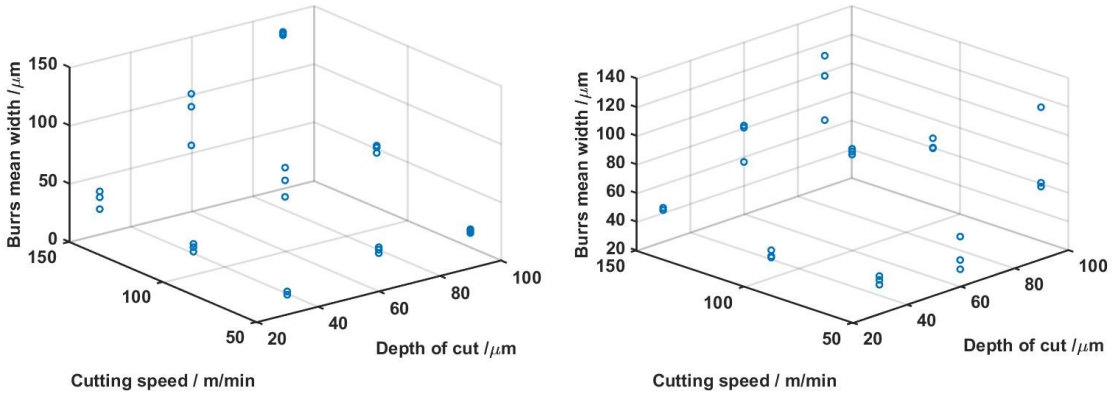

Figure 63 Variation of the burrs mean width in function of the cutting speed and depth of cut. On the left side the up-milling edge and on the right side the down-milling edge

Considering the 3D plot presented in figure Figure 61, Figure 62 and Figure 63 , the relation between burrs and depth of cut, changing the cutting speed is highlighted. From Figure 64 is possible to understand that the cutting speed has an effect on the burrs, for both up and down milling edges. On the other side, the feed per tooth is not effecting the burrs.

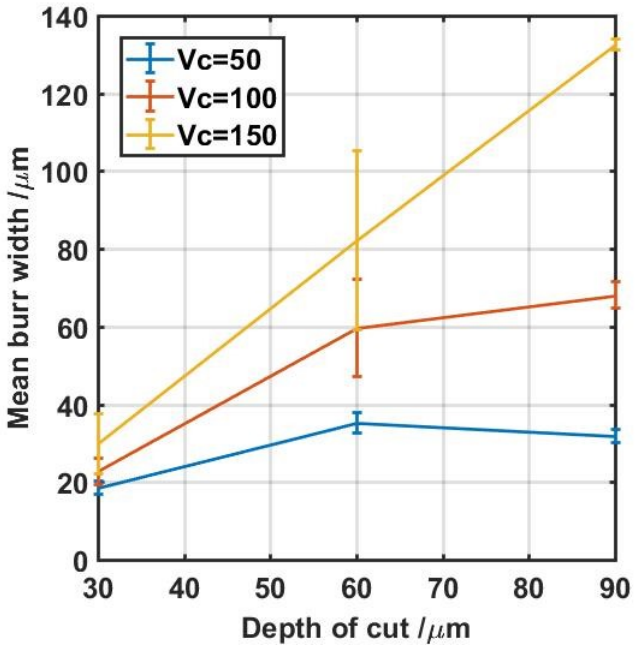

Figure 65 Correlation between mean burr width and depth of cut parametrized on the cutting speed

The combination cutting speed and depth of cut is really influencing the burrs: both cause a huge increment of the burrs for the up-milling side and down milling side. In order to highlight this effect, only this combination of parameters is analysed in deep. Mean values of the burrs inside the groups are considered and shown in Figure 65. The trend is clearly highlighted, the increase of depth of cut in the case of low cutting speed is not so important, moreover the increase of the speed, maintaining a constant and minimum depth of cut, maintains a constant burrs width. This effect is coherent with the state of the art and perfectly coherent with the qualitative evaluation obtained through SEM images and comparison of the topographies. From the results presented, it is evident how this method describes the variations in burrs dimensions. A fast and quantitative comparison between different machining strategies could be done using a single measurement step.

Conclusions

The method developed and presented in this chapter is a fast and flexible method that is suitable for micro-milled component, in which it is absolutely necessary to check all the machined parts and make the decision if burrs are dangerous or not for the next production steps. The method was developed in order to be suitable for topographies obtained from a standard confocal microscope, designed for topography evaluation but not powerful enough for sloped surfaces (like burrs). Optical limitations are against burrs measurement, but on the contrary speed, flexibility and in-line implementation are good points and characteristics to consider. Moreover, the use of an instrument designed for surface topographies evaluation and updated with this burr evaluation method, permits collection of all the information for a complete quality control of the machined sample (depth of the slot, roughness of the surface and burrs presence). Parameters for a better characterization of the burrs in longitudinal direction are presented, the maximum peak is fundamental to understand if there are isolated and dangerous parts (for assembly), mean width and moreover the percentage ratio gives all the quantitative information for decision making regarding after-machining processes. The limit has to be fixed in function of the process and quality requirements: in this way an automatic, non-destructive and fast measurement ensures constant quality check in machining process. The method was applied on different samples, correlating the mean burr width with machining parameters. The correlation with the cutting speed and the depth of cut is highlighted and clear from the measurements. Moreover a qualitative comparison with SEM images ensures the power of the method in burrs description. Burr width is

coherently described and measured through the proposed method, ensuring a fast and complete quality check of the micromachining.

4. Enhancing optical thread measurement through shadow correction

In this chapter a method and a relative algorithm for the improvement of the thread measurement with optical systems will be proposed. Such method is the subject matter of Italian patent application n. 102017000116818 jointly owned by Marposs S.p.A. and the University of Padova. Common methods for thread measurements are based on contact-systems, slow and difficult to be applied in industrial contexts. An optical system is surely more flexible and fast, moreover suitable for in line evaluation of the geometrical quality of the threads. The helicoidal shape of a thread and moreover the optical distortion induced by its form influences the quality of the measurement. The shadow generated by an optical system is not representative of the real geometry of the thread, because of the induced distortions. In this work, the correlation between the shadow and the real geometry is studied and a solution is proposed and verified. A post-process correction is presented and discussed. Different methods were developed in the past, considering the numerical shadow generation but mainly using a thread model. In this method, the thread model is not necessary and the correction is created directly from the shadow, without the need of user-defined parameters. Flexibility is the main characteristic taken into account for the development: different threads (not only ISO metric) should be automatically corrected without the need of preliminary information.

The chapter will be organized as follow: an introduction in which all the currently applied solutions are described and analysed, a subsequent section in which all the problems related to the measurements are analysed. Sensitivity analysis on different influencing factors are presented and discussed and finally the correction model is described. Preliminary numerical validation and experimental analysis are presented in this chapter. Finally, in the last section the experimental validation of the correction model is presented and the obtained results are compared with the reference values.

Introduction

Generally the thread measurements are developed using contact systems (e.g. three wire method), but these methods are really suffering speed of the process and in particular difficulties in in-line implementation. On the contrary, non-contact methods (and in

particular methods based on the image processing techniques) are suitable for in-line implementation, are really fast in application and moreover ensure a collection of a huge amount of information. However, there is a problem correlated with the optical systems: image methods and optical techniques are influenced by the geometry of the thread. Optical methods create a projection of the thread instead of a section of the thread on the central axis. Helicoidal geometry of the thread generates a shadow that is not representative of the section of the thread. Moreover, this projection is not suitable for the evaluation of the thread parameters and introduces different errors and uncertainties. The reference profile of the thread is defined on a plane containing the axis of the thread; the shadow obtained with the optical system is not comparable with this profile.

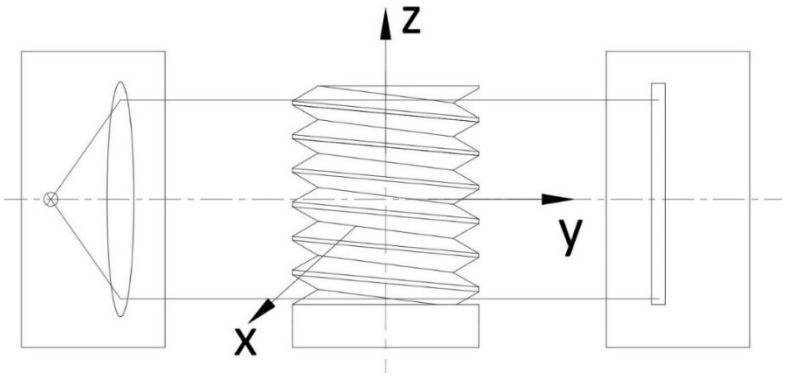

Figure 66 Example of an optical system for thread measurement

Figure 66 shows a general scheme of an optical system for the measurement of the threads. The problem related to the shadow is clearly described in Figure 67. The system of reference used for the description of the problem is depicted in Figure 66 and left side of Figure 67 describes the section of the thread. This section is obtained cutting the thread with the *z-x* plane. Nevertheless, on the right side is presented the thread from the point of view of the camera: the difference between these two images is clearly caused by the helicoidal geometry. Different profiles are obtained from these two different situations.

The two profiles obtained in the two different cases are presented in Figure 68: the thread profile (depicted in black) is the profile on the *z-x* section plane, the projected profile (depicted in red) is the profile obtained with an optical system looking to the thread along *y* direction (referring to Figure 66).

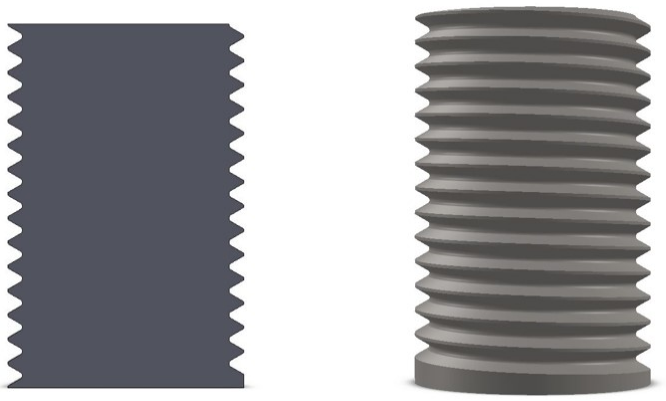

Figure 67 Example of the section of the thread on the left and view from the camera on the right

The difference between the two profiles presented in Figure 68 should be corrected in order to make geometrical considerations and measurements on the shadow image. In literature the most used approaches are based on a mathematical description of the shadow projection. Starting from the thread model it is possible to extract the correction matrix that has to be applied on the shadow profile.

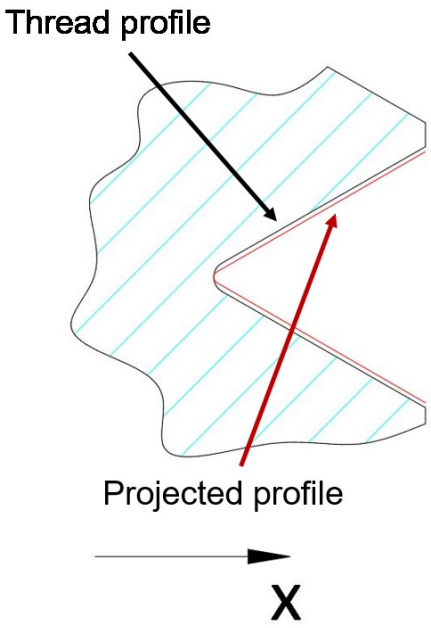

Figure 68 Difference between the thread profile and the projection caused by the helicoidal geometry

In order to solve this problem, different approaches were developed. The most important works in this field are the subsequent patents:

- Method for optoelectronic determination of screw thread parameters, whereby a shadow image of the thread is generated and a correction value determined by comparison

of measured thread pitch and diameter values with known values, registered by Kratsch Nora for Hommelwerke GmbH [1];

- Metodo di derminazione optoelettronica di parametri di filettatura, registered by Andreini Stefano for Vici & C. S.r.l. [2].

Both the patents are referring to the Lotze publication (Lotze & Will 1991), the baseline publication for all the other researches in this field. This article is extracted from the ph.D. thesis of Xiaomei that will be fully and in deep described in the next section.

The article of Shchurov published in 2011 (Shchurov 2011) describes a new procedure for the evaluation of the "virtual pitch diameter", starting from the point cloud obtained with a CMM. The extraction of the parameter from the point cloud is the focus of this publication, nevertheless there is no correction of the points and no correction model that could be used in a system that is completely different from the one under investigation. Publications that try to solve the problem of the measurement of the threads using optical systems are in particular the one from Jiang (Jiang & Zhang 2012) and Hunsiker (Hunsicker et al. 1994). In (Jiang & Zhang 2012) different method for the correction is developed and presented: all the coordinates related to the optical axis of the points that describe the thread are projected on the 0 reference position. In this way could be obtained the shadow projection of the model, moreover in the work a huge investigation was done on the "edge detection" algorithms needed for the identification of the thread profile starting from the shadow. But this paper does not describe particular corrections or algorithms, moreover there it is not proposed by the authors an alghorithm for the generalization of the method for each type of threads (the analysis is based only on a 20 mm external diameter and 2 mm pitch thread).

In (Hunsicker et al. 1994) all the technical choices and considerations developed for the development of a measuring system suitable for the thread measurements are presented. Different technical solutions were studied for ensuring the orthogonality between the axis of the thread and the optical axis of the measuring instrument, but also in this case there are no corrections for the errors directly associated with the geometry of the thread itself.

Regarding the uncertainty analysis, the most valuable publications are releated to Kosarevsky's (Kosarevsky 2010) and Sheng's (Sheng et al. 2014) work .

All the previously mentioned articles are based on contact measurement, so they are not strictly related with the measuring system under evaluation. Different methods for the correction of some systematic errors for the evaluation of the uncertainty are presented and could be applicable also for optical systems. These methods are useful for some considerations on the effect of the angle between the optical axis and the thread axis on the thread parameters. In (Kosarevsky 2010) the alignment problem between the thread and the profilometer is analysed: the authors develop an uncertainty analysis associated to this effect for the most common thread parameters. The Sheng's (Sheng et al. 2014) article is focused on the compensation of the misalignment between the profiler and the thread axis: a compensation procedure for systematic errors is presented and discussed. Also in this case, the compensation procedure is mainly a physical correction of the system, from this point of view it is not flexible and applicable in line and to different types and dimensions of threads.

The most relevant guides and references (for standardized definition of thread parameters) are mainly the Euramet guide (EURAMET 2007) and moreover ISO standards (ISO261:1998 n.d.; ISO724:1993 n.d.; ISO965-1:2013 n.d.; ISO5408:2009 n.d.). In the Euramet publication are also presented all the formulations and procedures for the calculation of the parameters. All the definitions and moreover, information on the parameters are collected from (ISO5408:2009 n.d.) and EURAMET (EURAMET 2007) guide are shortly resumed in the following.

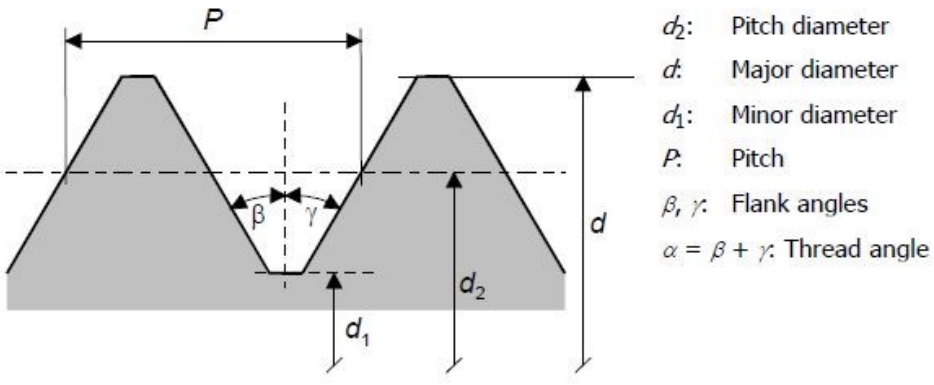

Figure 69 Representation of the thread parameters (EURAMET 2007)

In order to understand the most important parameters a short description is presented, dividing the parameters in two groups. The first group collects the parameters not influenced by the shadow projection (this means that the parameters could be calculated

directly on the shadow profile) and the second one describes the parameters influenced by the shadow. Figure 69 (taken directly from (EURAMET 2007)) shows the most important parameters and it is used as reference for the abbreviations.

The parameters that are not influenced by the shadow projection are:

- *Major diameter*, *d*: The diameter of an imaginary cylinder (termed the major cylinder) that would bound the crests of an external thread or the roots of an internal thread;

- *Minor diameter*, *d1*: The diameter of an imaginary cylinder (termed the minor cylinder) that would bound the roots of an external thread or the crests of an internal thread;
- *Pitch*, *P*: the distance, measured parallel to the axis, between corresponding points on adjacent thread forms in the same axial plane and on the same side of the axis.

The parameters previously defined are measurable directly on the shadow image. Nevertheless, the parameter influenced by the shadow are:

- *Pitch diameter*, *d2*: The diameter of an imaginary cylinder (termed the pitch cylinder), the surface of which intersects the thread profile in such a manner as to make the width of the thread ridge and the thread groove equal;
- *Flank angle*, β e γ: The angles between the individual flanks (leading and trailing flank) and the perpendicular to the axis of the thread, measured in an axial plane section;
- *Thread angle*, α: Sum of the two flank angles;

These last parameters are influenced by the shadow. Because of the shrinkage of the profile the angle between the two profile extracted from the shadow projection and measured on the projection is smaller than the angle on the section plane cointaining the thread axis (on an axial plane). The pitch diameter is influenced by the shadow because of the distortion of the projected flanks. An evaluation of the pitch diameter directly on the shadow causes an overestimation of the value as well as being not in accordance with the definition.

Going back to the publication on this topic, the most important reference is the Lotze's article (Lotze & Will 1991) and in particular the Ph.D. thesis from Xiaomei (Xiaomei 1989). In that thesis, two different methods for the mathematical description of the shadow of a cylindrical thread are presented. The author demonstrates that both the

methods are bringing to the same final result, and uses these mathematical formulations for the creation of some correction tables. Through these tables, the profile obtained from the optical system could be corrected and compared with the reference one. The correction tables are obtained through a mathematical reconstruction of the projection knowing the mathematical model of the thread. The nominal thread is described by a mathematical formulation: starting from this one is obtained the shadow projection. Therefore, an important and common part between the two methods presented by the author is the mathematical description of the thread. Only the external surface is described (helicoidal revolution of the nominal profile), using the polar coordinates, dividing between the upper and lower flanks. The approach is divided in:

- Assumption of some fundamental parameters from the ideal geometry (thread model)
- Creation of the surface that represents the thread
- Mathematical calculation of the shadow (through the two different methods described below)
- Creation of the correction table from the comparison between the mathematical projection and the nominal profile

As previously said, the author presents two different methods for the creation of the shadow: one method is based on the evaluation of the normal vectors of the surface, the second method is based on the use of section planes.

In the first method the external surface of the thread is described by a vector r and two parameters: t and φ. Knowing the vector, by making the partial derivation respect t and φ are obtained the components of the normal vector n, function of t and φ. The system of reference fixed by the author is aligned in this way: *x axis* aligned with the thread axis, *z-axis* parallel to the optical axis (the shadow of the thread is generated on a plane parallel to the *x-y* plane, ignoring errors related to the orthogonality between the detector and the *z-axis*). In this way, the shadow is defined by the extreme points respect the *x-y* plane. The author demonstrates that all the extreme points are characterized by a z-component of the normal vector equal to zero: the extreme points, in order to create the shadow in the *x-y* plane present a normal vector that is normal to the *x-y* plane itself. This means that the z component of the normal vector should be equal to zero. For each radius r (function of t and φ) should be found $nz=0$ (finding the extreme points that generate the shadow in

the *x-y* plane).

On the other side, the second method is based on a sectioning process of the thread using planes parallel to *x-z* reference plane: for each plane it is possible to identify the maximum (or the minimum for the bottom profile), comparing the x coordinate of the found points. This new profile is obtained fixing the *y* value (using a constant) and finding *r* as a function of the rotation angle of the helix. With this method, for each section plane it is possible to find the extreme points on both the bottom and top profile.

The author demonstrates that the two different solutions are bringing to the same last result, moreover are provided the tables for the correction of the effect associated with an optical system. From the shadow, for a particular diameter, Δx and Δy that are needed for the correction are then calculated. The important assumption made by the author for the development of this model is related to the thread angle: this angle should be assumed equal to the nominal one for the creation of the correction tables because of the impossibility to measure it from the shadow. This means that the thread model should be fixed *a priori*.

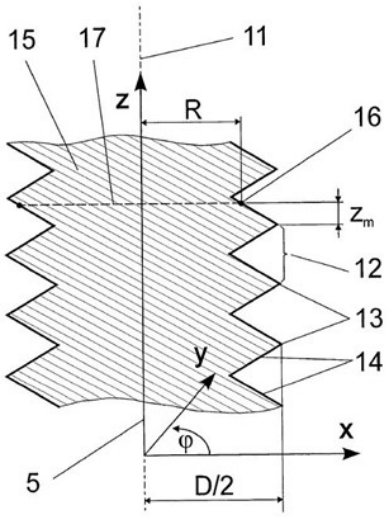

Figure 70 Parameters for the evaluation of the correction (Kratsch 2008)

In another patent registered by Hommelwerke GmbH (Kratsch 2008) there is a proposal of a different method for the evaluation of the thread parameters obtained with optical systems. In addition, in this case the author is trying to solve the problem of the difference between the shadow and the nominal profile. This difference is linked to the geometry of the thread itself. The optical system and the system of reference used in this work are

equal to the ones presented in Figure 66. The optical axis is parallel to the *y-axis*, this means that the shadow is in the plane *x-z*, and *z*-axis is aligned with the axis of the thread. In this case, through the presented method, the correction is equal to a Δx quantity, function of the *zm* variable, as depicted in Figure 70 (as previously said *z* is the thread axis).

In this case the correction is applied on each single point of the profile and depends on the pitch and the external diameter (evaluated directly form the shadow). In this case the shadow is obtained with a different mathematical formulation respect to the Jiang proposal (Jiang & Zhang 2012). The thread is sectioned using planes parallel to the *x-y* reference plane, obtaining different circumferences not centred to the axis of the thread. The main problem at this point is how to calculate the extreme point (e.g. *P1*) that generates the shadow, obtained from the intersection between a plane (e.g. Sxy) and the thread surface. If the circumferences are centred on the thread axis, the point P1 should be centred on the *x-axis*. In this case, because of the misalignment between the center and the axis, the point *P1* is characterized by *y* component (this is the reason why the shadow and the nominal profile are different). This point is identified by maximizing the x coordinate of the generated profile.

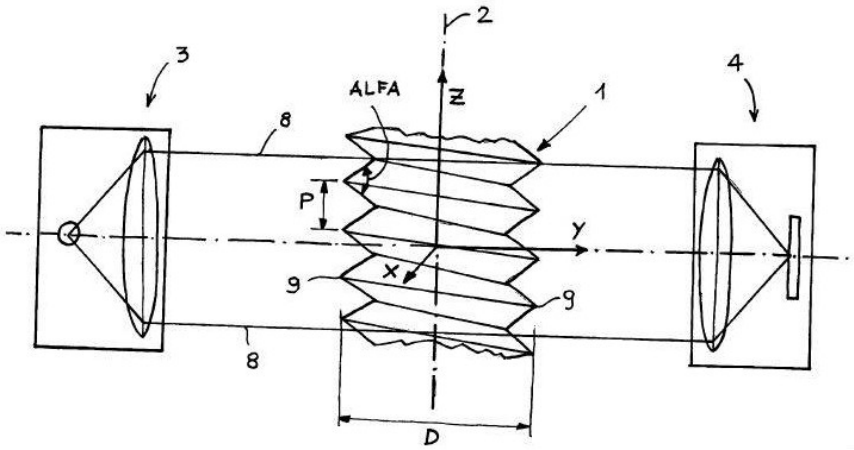

Figure 71 Scheme of the optical system developed by Vici (Andreini S. 2012)

The external surface of the thread is described using the Lotze formulation (Lotze & Will 1991) and this surface depends on the thread model. So, the most important difference between these two solutions is releated to the way in which the point that generates the

shadow is calculated: in this patent the sectioning planes are parallel to *x-y* plane and moreover the correction is function of *zm*.

The patent registered by Vici & C. S.r.l. (Andreini S. 2012) proposed another solution for this problem. As well described in Figure 71, also in this case the optical axis is aligned with the *y-axis*. The shadow is depicted in a plane parallel to the *x-z* plane. This is the first solution that doesn't require to know the model of the thread for the development of the correction (neither the model nor the thread angle). From the shadow is calculated the angle of the thread (named *ALFA_1* in Figure 72). In order to easily understand the procedure, Figure 72 and Figure 73 are directly taken from the patent.

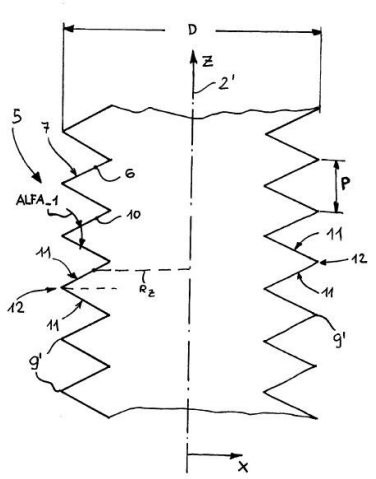

Figure 72 Section of the thread and principal parameters (Andreini S. 2012)

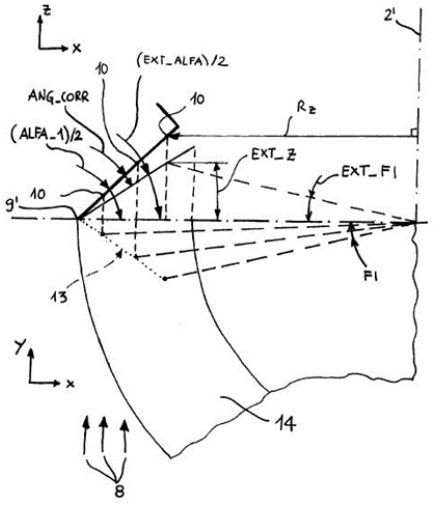

Figure 73 Procedure for the evaluation of the correction (Andreini S. 2012)

The angle *ALFA_1* is corrected using an angle named *ANG_CORR* in Figure 73 equal to the helix angle of the thread. This angle could be evaluated directly from the pitch *P* and the external diameter *D* (directly obtained from the shadow). Subtracting the correction *ANG_CORR* from the angle *ALFA_1* (previously measured) it is possible to obtain an estimation of the thread angle *EXT_ALFA*. For a random point of the measured profile is calculated the theoretical coordinate *z*, named *EXT_z*. This should be the coordinate of the measured point on the *x-z* plane using the distance *rz* from the thread axis and using the first value of *EXT_ALFA*. From this first estimation of the theoretical coordinate *EXT_z*, could be estimated the angle *EXT_Fi*, rotation angle on the *x-y* plane that should connect the shadow point with the correspondent theoretical profile point. The correction *SHIFT_Z* is equal to the increment of the coordinate of the thread, equal to a rotation angle *EXT_FI* (estimated value).

The main differences between this model and the previous ones is the need of an assumption: in this case the model of the thread is not necessary for the development of the correction.

There are moreover others two patents in which a correction is presented. The U.S. patent (Stanley & Lawrence 2011) is basically correcting the thread diameter, without considering the entire profile. In this case the correction is function of the flank angle. In a different patent (Junhua et al. 2011) an iterative procedure is presented and developed. Starting from two assumed values of the pitch and the thread angle (from a nominal profile, described through a mathematical function) the correction is obtained by changing the model and iteratively calculating the shadow.

Considering all the previously developed methods, the most important limitation identified is the common use of a model. This a priori information is restrictive, moreover it is not flexible and no one is applying different correction for each different flank.
This work presents a newly developed method for the correction of the thread shadow. The most important difference with respect to the previous one is related to the self-application, no a priori information is needed and moreover a different correction for each flank is calculated and applied. Thanks to this method, the evaluation of the threads parameters could developed using the optical system also for asymmetrical and non-cylindrical threads.

In the first part the mathematical formulation used for the development of the method will be described. After that, different influencing factors are studied and the effect is quantified through numerical simulations. Limitations of the preliminary method are studied and presented in order to justify and understand the subsequent extensions. After this first part the final correction procedure is presented and verified using numerical simulation. After an optimization and extension to a complete variety of threads, the final correction model is applied to an industrial case and verified using calibrated measurements. All the results are finally presented and discussed.

Materials and methods

In this chapter the mathematical aspects of the numerical shadow creation are firstly presented. After this first description the most important aspects of the previous publication are analysed and used for the development of the correction method. Influencing factors and assumptions are verified through numerical simulations, moreover the sensitivity of the correction method to the real thread parameters are developed and presented. Finally, the general correction method is presented and numerically verified.

Mathematical description of the shadow

From the analysis of the work of Xiaomei (Xiaomei 1989) it is possible to develop a first preliminary correction model. The model presented in the previous work is shortly based on:

- Preliminary knowledge of the nominal parameters of the thread
- Thread angle equal to the nominal one (for ISO threads the angle, generally called α, is equal to 60°)
- Calculation of the shadow through two different methods
- Comparison between the shadow projection an the nominal model and calculation of the correction that has to be applied to the measured data

The two methods described in the thesis are based on two different approaches. Shortly the use of normal vector or section planes parallel to the plane generated by the thread axis and the optical axis. Thanks to the second method it is possible to find the minimum and maximum of the profiles obtained through the sectioning process. The parameters used for the creation of the model are the distance from the thread axis r and the angle φ,

defined as the angle between the vector pointing each point of the profile and fixed in the origin and the *x-axis*. The reference system is centred with the *z-axis* aligned with the thread axis, *y* along the optical axis and *x-axis* completing the right-hand reference system. Derivation respect *z* allows to evaluate the minimum and maximum, so the points that generates the shadow.

The equation that describes the profiles is reported in equation *4.1*.

$$\begin{cases} x = r\cos\varphi \\ y = r\sin\varphi \\ z = z_0 + \dfrac{\varphi}{2\pi}P \end{cases} \quad 4.1$$

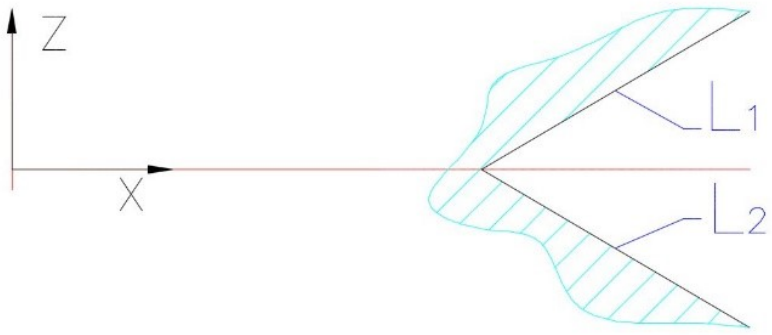

Figure 74 Flanks of the threads

With reference to Figure 74 the equation that describes the upper and lower flanks (considering the *z-axis* vertical) are:

$$L_1: \begin{cases} x' = r \\ z' = z_{01} - r\tan\beta \end{cases} \quad 4.2$$

$$L_2: \begin{cases} x' = r \\ z' = z_{02} + r\tan\gamma \end{cases} \quad 4.3$$

Equations 4.2 and 4.3 are defining the profile in a section plane (*x'* and *z'* are referring to a reference system rotating with the helix, in the case of Figure 74 the two reference systems are overlapped). Finally, the helicoidal rotation of the section plane (rotation of an angle *φ,* considering the reference system *O'* with *z'* aligned with *z)* around the *z-axis* of the absolute reference system *O* is described through the equations reported in 4.4 and 4.5.

$$L_1: \begin{cases} x = r\cos\varphi \\ y = r\sin\varphi \\ z = z_{01} - r\tan\beta + \dfrac{\varphi}{2\pi}P \end{cases} \quad 4.4$$

$$L_2: \begin{cases} x = r\cos\varphi \\ y = r\sin\varphi \\ z = z_{02} + r\tan\gamma + \dfrac{\varphi}{2\pi}P \end{cases} \quad 4.5$$

In order to develop the shadow projection using the method proposed in Xiamoei's dissertation (Xiaomei 1989), planes parallel to *z-y* are used. Varying the *x* coordinate, maintained fixed for each different section, the coordinates of the obtained profile are expressed in equation 4.6 (for the flank L_1, referring to Figure 74).

$$\begin{cases} r = \dfrac{x_{cost}}{\cos\varphi} \\ y = x_{cost}\tan\varphi \\ z = z_{01} - \dfrac{x_{cost}}{\cos\varphi}\tan\beta + \dfrac{\varphi}{2\pi}P \end{cases} \quad 4.6$$

At this point, it is possible to find the minimum point that generates the shadow making the derivation respect to the *y* variable, this means finding the solutions of the equation $\frac{\partial z}{\partial y} = 0$. The solution is function of the angle φ and is shown in equation *4.7*.

$$-\sin^2\varphi - 2\left(\frac{\pi x}{p}\right)\tan\beta\sin\varphi + 1 = 0 \quad 4.7$$

For the profile L_1 (referring *to* Figure 74) it is possible to obtain the solution respect to φ:

$$\varphi = \arcsin(-D_1 + \sqrt{{D_1}^2 + 1}) \quad 4.8$$

The solution reported in equation 4.8 is obtained for $x > 0$ and $D_1 = \frac{\pi x}{p}\tan\beta$.

With the same analytical steps is obtained the solution for the flank L_2:

$$\varphi = \arcsin(D_2 - \sqrt{{D_2}^2 + 1}) \quad 4.9$$

Also in this case it is valid for $x > 0$ and $D_2 = \frac{\pi x}{p}\tan\gamma$.

Considering a point on the profile L_1, characterized by an x coordinate $x = x_{Lm}$, it is possible to evaluate the corresponding z value of the shadow projection:

$$L_1: z_{1m} = z_{01} - \frac{x_{Lm}}{cos\varphi_{Lm}} tan\beta + \frac{\varphi_{Lm}}{2\pi} P \quad 4.10$$

Considering the differences between the correspondent points (fixing the x coordinate), the correction could be obtained as the difference between the projected profile and the nominal profile in the x-z plane:

$$\Delta Z_1 = z_{rif1} - z_{1m} = x_{Lm} \tan\beta \left(\frac{1}{cos\varphi_{Lm}} - 1\right) - \frac{\varphi_{Lm}}{2\pi} P \quad 4.11$$

For the profile L_1 the correction is reported in equation 4.11. Analogously to the previously described steps, for the profile L_2 the equations are reported in 4.12 and finally in 4.13.

$$L_2: z_{2m} = z_{02} + \frac{x_{Lm}}{cos\varphi_{Lm}} tan\gamma + \frac{\varphi_{Lm}}{2\pi} P \quad 4.12$$

$$\Delta Z_2 = z_{rif2} - z_{2m} = x_{Lm} \tan\gamma \left(\frac{1}{cos\varphi_{Lm}} + 1\right) + \frac{\varphi_{Lm}}{2\pi} P. \quad 4.13$$

The corrections obtained at constant x coordinate are used in this approach. If the corrections are calculated considering a fixed value of r instead of a fixed value of x, the obtained differences are expressed by equation 4.14.

$$\Delta Z_{r=cost} = z_{rif1} - z_{1m} = -P \frac{\varphi_{Lm}}{2\pi} \quad 4.14$$

The difference in the approach is described in *Figure 75*. Considering the second method, maintaining constant the r value, the correction is obtained subtracting the z coordinate of A^* to the z coordinate of $x1$. In this case it is necessary to consider also a correction along the x direction. On the contrary, fixing the x coordinate, the correction is obtained considering the subtraction between the z coordinate of the projection A and the z coordinate of the point $x1$, considered both at the same x coordinate.

For a distorted thread angle of 55° the differences between these two approaches are reported in Figure 75 and Figure 76. In these cases the value of the coordinate x_0 is constant (discussion regarding this parameter in the following) and the values of the external diameter and pitch are calculated on the reference profile obtained with the thread angle of 55° (not considering the parameters obtained on a reference of 60°).

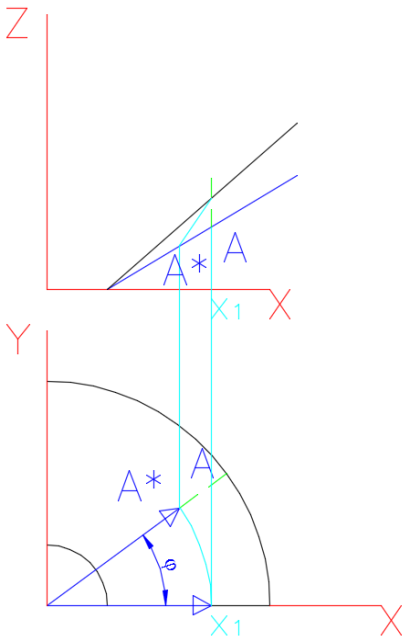

Figure 75 Comparison of the different approaches

The approach based on a fixed value of the x is mostly suitable for optical measuring systems. In the case of the shadow, a point (that is characterized by the same x coordinate) obscures the correspondent point of the thread section profile.

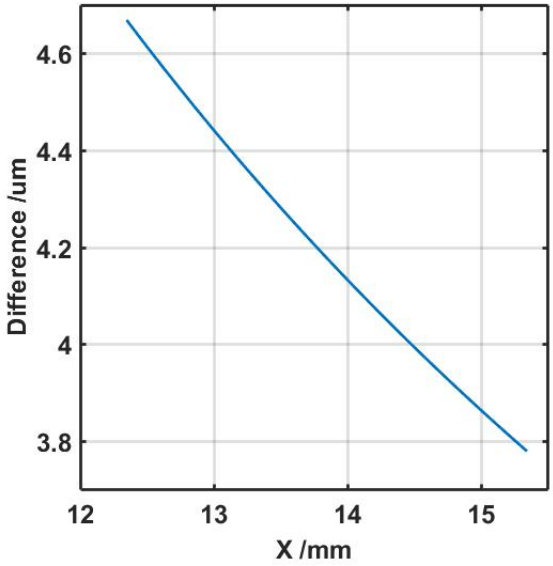

Figure 76 Differences obtained with a constant radius

Going back to the equations, it is possible to create an a-dimensional correction, using the pitch p. This formulation was proposed in previous works and used for correction of the thread profile.

$$\frac{\Delta z}{p} = -\frac{1}{2\pi}\text{asin}(\pi\frac{x}{p}\tan(\alpha) - \sqrt{(\pi\frac{x}{p}tan\alpha)^2 + 1} \quad 4.15$$

The trend of the correction is presented in *Figure 78*, this equation was obtained directly from the publication of Lotze (Lotze & Will 1991), changing the reference system.

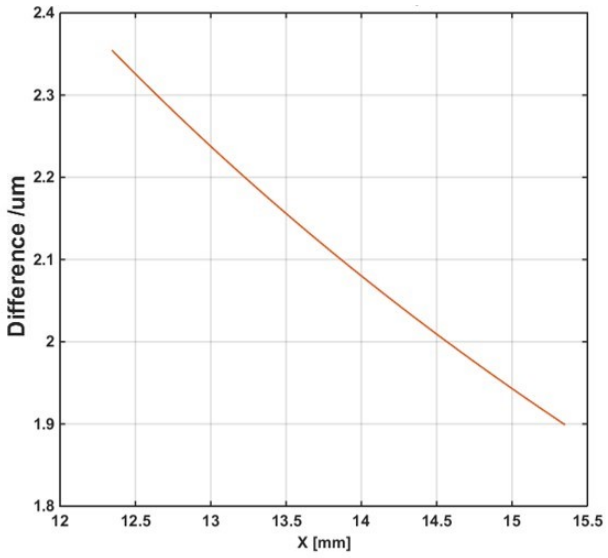

Figure 77 Differences obtained with a constant x coordinate

From the previously described procedure and equations seems the determination of the correction could appear easy. Nevertheless, the application of the correction model and the calculation of the correction quantities is possible only if the nominal profile of the thread is well known. This means that the previously described procedure starts from the nominal profile, and from that calculates the correction that has to be applied on the real profile, instead of starting from the real profile. The problem at this point is related to the differences between the projection of the model and the real projection. These differences are related to the thread angle, moreover to the symmetry of the two flanks (differences between the angles β and γ).

The procedure developed in this thesis would overcome the limitations and increase the flexibility of the correction model, in order to be easily applied to a random thread profile, without the need of preliminary information. The next chapters analyses all the influencing parameters and their effect is quantify through numerical simulations.

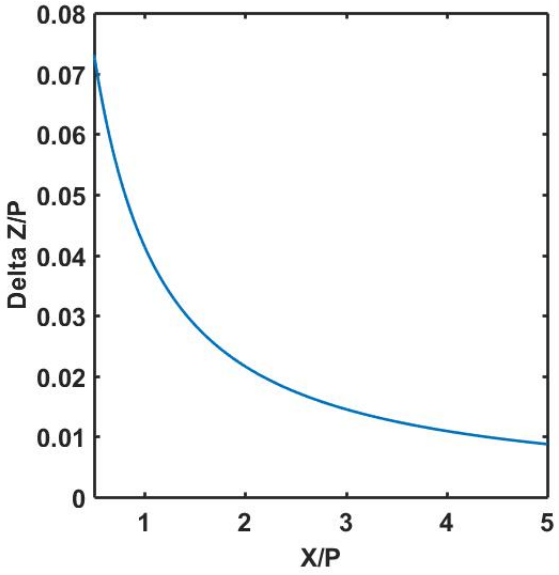

Figure 78 Trend of the correction proposed by Xiaomei

Effect of the real thread angle on the correction

The sensitivity of the correction model to the real thread angle was analysed through the implementation of the alghorithms in Matlab environment. A preliminary evaluation was done considering as reference the ideal model of an M30 thread with coarse pitch, but characterized by a thread angle α equal to 55° (instead of the standard metric 60°). All the parameters of this ideal thread are known (pitch and external diameter are equal to the reference ones and the angle α equal to 55°) and in the following this thread will be indexed as "reference thread". The reference thread, highlighted in red in *Figure 79*, is mathematically projected in order to obtain the shadow (green profile in *Figure 79*). This projection is subsequently corrected using a nominal model based on a thread angle α equal to 60° (named "Nominal profile"). The final corrected profile is highlighted in yellow in *Figure 79* (named "Corrected profile"). The profile used for the correction, the "nominal profile" is the blue one, representing a M30 thread with a nominal angle α equal to 60°.

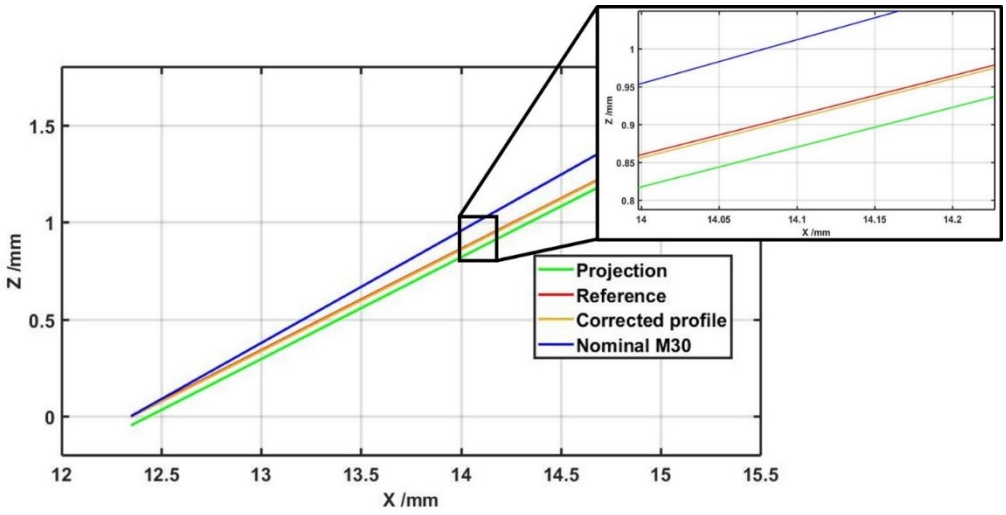

Figure 79 Comparison between the reference profile with an angle of 55° (Reference) and the projection (Projection) and the corrected profile obtained with a nominal model based on a thread angle of 60°

The difference between the yellow curve (*Corrected profile*) and the red one (representing the *Reference profile* in the section plane) is shown in *Figure 80*.

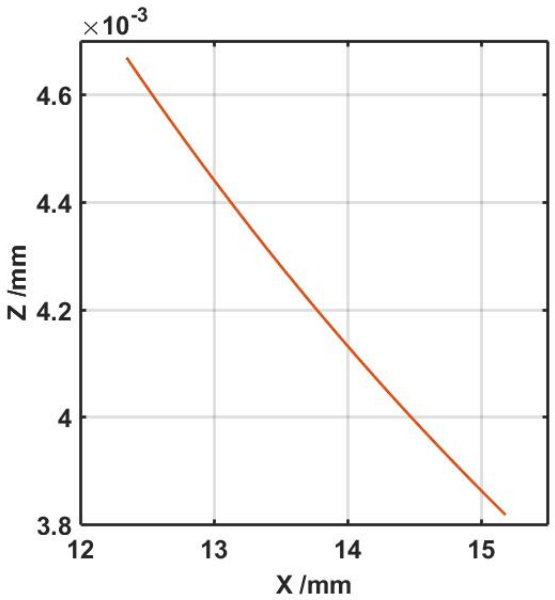

Figure 80 Difference between reference profile and corrected profile for an M33 with a thread angle of 55°

After the preliminary evaluation of the difference between the two profiles (*reference profile* and *corrected profile*), was quantified the effect of the correction on the pitch diameter. The sensitivity was understood by simulating different angles. A selection of these angles and a selection of different threads is presented in *Figure 81*. Y axis describes the difference between the pitch diameter calculated on the *corrected profile* (using the correction based on a nominal thread with an angle α equal to 60°) and the pitch diameter

calculated on the *reference profile*, varying the thread angle (from 55° to 65°). Moreover, *Figure 81* highlights the effect of the absolute dimension of the thread (from M1 to M30).

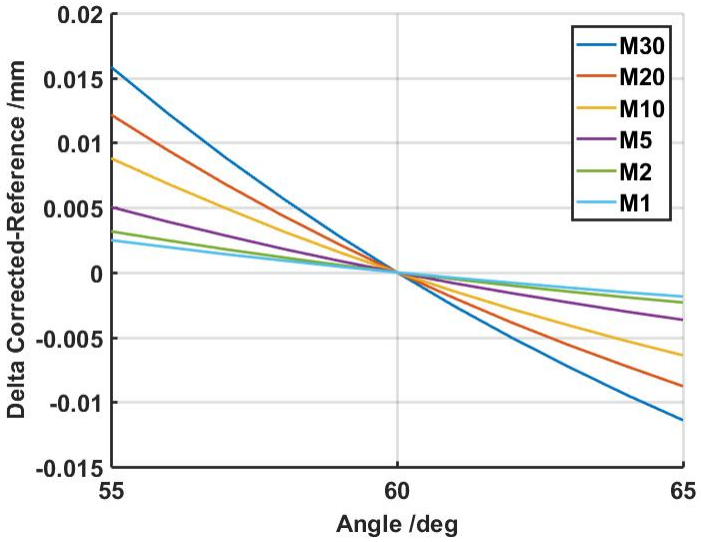

Figure 81 Differences between pitch diameter evaluated on the corrected profile (corrected with a nominal thread with an angle α = 60°) and the pitch diameter evaluated on the reference profile. Both the diameters are evaluated changing the thread angle.

The sensitivity analysis and the obtained results demonstrate that the correction method based on the nominal profile (with an angle α equal to 60°) could introduce errors that in some cases are relevant. For these reasons the correction method should use a profile (for the creation of the mathematical shadow) as similar as possible to the reference one, and this could be done only considering the real profile as a starting profile for the correction.

Effect of the correction Δx_0

Δx_0 is the difference between the coordinate *x0* of the intersection of the shadow profile and the ideal intersection of the reference profile (on the section plane). For clearly understand this effect, a representation of this intersection is reported in *Figure 82*.

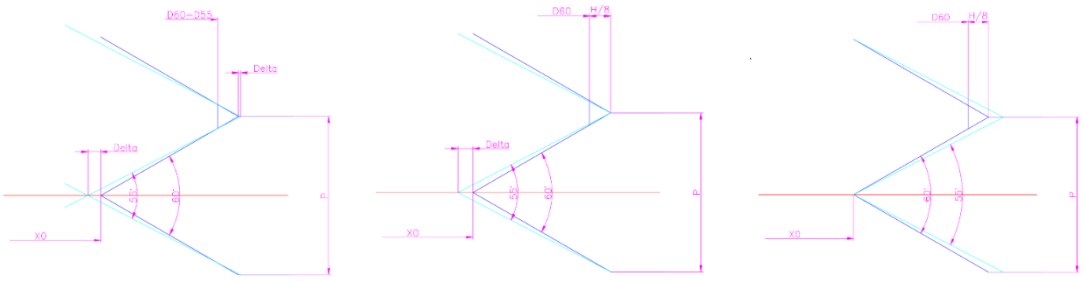

a *b* *c*

Figure 82 Different possible alignments between the distorted profile and the thread model

Δx_0 varies with the alignment between the *reference profile* and the real profile. Three different cases are presented in *Figure 82*. In *Figure 82*a the two profiles are aligned fixing the intersection of the profiles on the external diameter, in Figure 82b the profiles are aligned on the external intersection between two consecutive reference flanks and in *Figure 82*c the alignment is based on the internal intersection between reference flanks of the same thread. The cases presented in Figure 82 are useful because highlights the need of a correction strictly linked to the real profile.

Moreover, the need to evaluate Δx_0 is strictly connected with the flexibility of the correction, in order to be as general as possible. The variation of the coordinate x_0 is associated with the difference between the angle of the real thread and the model. So, referring to *Figure 82*, it is necessary to find the coordinate x_0^* starting from the measured value $x_{0_p}^*$.

Assuming that the variation Δx_0 calculated on the reference is constant also on the measured profile, the procedure that was developed for the evaluation follows the subsequent steps:

- Calculation of Δx_0 on the reference: $\Delta x_0 = x_{0_p} - x_0$ (in this case x_0 is known because it depends from the thread angle of the reference, the external diameter and the pitch);
- Assuming $\Delta x_0^* = \Delta x_0 = x_{0_p} - x_0$, valid for $x > 0$ (where $\Delta x_0^* = x_{0_p}^* - x_0^*$);
- Could be calculated $x_0^* = x_{0_p}^* - \Delta x_0$.

This translation is caused by the variation of the thread angle maintaining constant the external diameter and the pitch. In *Figure 83* the effect is highlighted (the figure is focused on a small part of the thread) using a M30 coarse pitch thread. The effect of different thread angles (between 0° and -2° respect the standard value of 60°) was analysed and presented in *Figure 83*. The continuous line represents the shadow profile and the dot line is the *reference profile*, evaluated on the section plane.

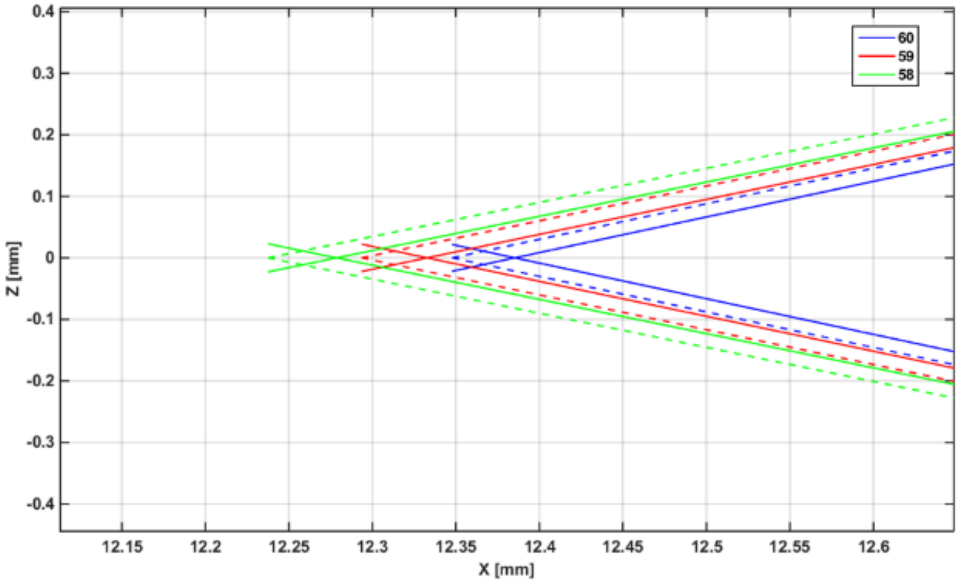

Figure 83 Example of the variation of x0 varying the thread angle for an ISO M30

In order to verify that the previous assumption is acceptable, the trend of the difference Δx_0 was evaluated for different threads in between 0° and -2° respect to the nominal value (60° for the ISO metric threads).

The results are shortly reported in Table 41: the Δx_0 obtained for the threads with an angle equal to 60° and the distorted ones are comparable (maximum difference of 4 µm for a thread with an angle of 58° and diameter 30 mm). Considering these differences the assumption is accepted and used in the future development of the method.

Thread	M10 coarse pitch			M20 coarse pitch			M30 coarse pitch		
α	60	59	58	60	59	58	60	59	58
x_0	3.863	3.840	3.816	8.106	8.067	8.027	12.348	12.294	12.238
x_{0p}	3.885	3.863	3.840	8.135	8.097	8.058	12.385	12.333	12.278
Δx_0	0.021	0.023	0.024	0.029	0.030	0.032	0.037	0.039	0.041

Table 41 Differences between references and shadows (values expressed in mm and angles in degrees)

Moreover, as clearly shown in Table 41, if the correction on the coordinate x_{0p} was not developed, the obtained errors are in the order of tens of microns.

Proposal of a correction method

Resuming the previous considerations, the method for the correction of the shadow should be based on the real shadow, instead of using an a-priori thread model. The preliminary method proposed for the metric threads is basically inspired to a scale factor on the thread angle (scale factor that amplifies the real angle in order to create a suitable model).

A scheme of the proposed correction method is presented in Figure 84. The pitch and the external diameter of the thread could be measured from the shadow projection of the *actual profile* (the actual profile is obtained directly from the shadow coming from the measuring system). Thank to these two parameters the *reference model* of the thread is created and used for the comparison. In this preliminary proposal, the angle of the reference model is assumed to be equal to 60° and the external diameter and the pitch used for the evaluation are assumed to be equal to the nominal one (next section deals with the use of the actual external diameter and pitch for the evaluation of the correction). So, knowing the thread model (a profile with a thread angle α equal to 60° and named *"nominal profile"*), is possible to mathematically describe the shadow of the ideal thread (named "*nominal projected profile*"). On the *actual profile* is possible to calculate the angle α_P^*(different from the thread angle), while on the *nominal profile* is calculated the angle α_P.

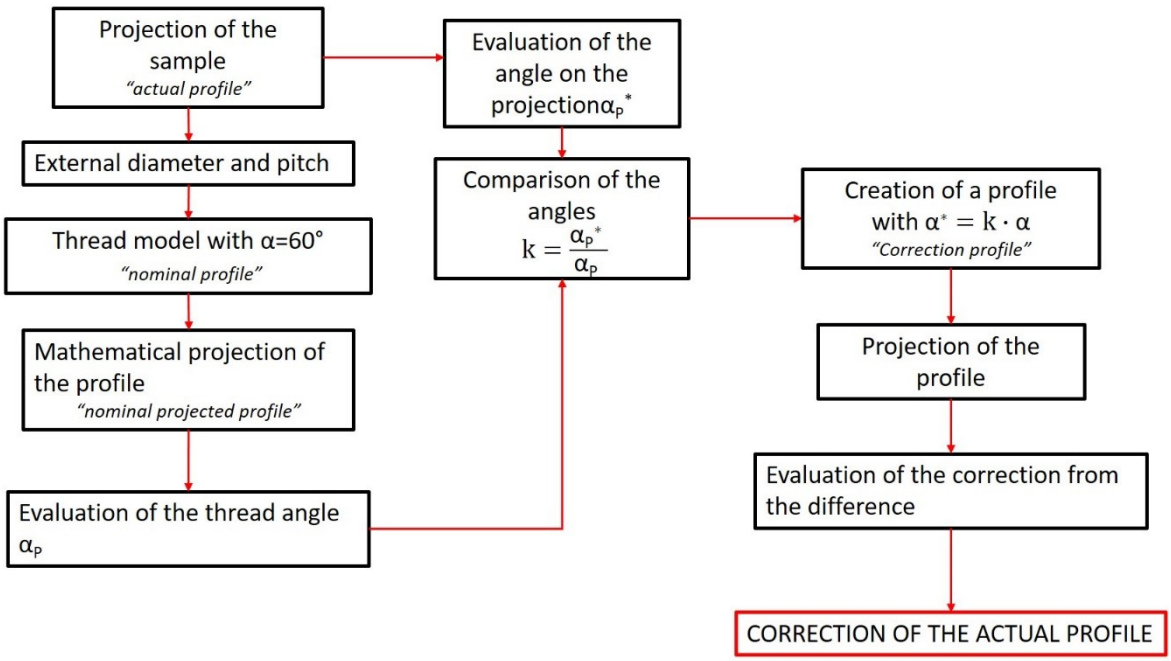

Figure 84 Flux diagram of the proposed correction

From the comparison between these two angles is possible to calculate the correction factor $k = {\alpha_P^*}/{\alpha_P}$.

The initial phase assumes the relation $k = {\alpha_P^*}/{\alpha_P} = {\alpha^*}/{\alpha}$, where α is the angle of the *nominal profile*, while α^* is the angle evaluated on the *"correction profile"* (profile obtained from the *actual profile* after a correction in order to project it on an axial plane). The angle α is well known, because it is preliminary assumed from the thread model, while the angle α^* is obtained from α through the correction factor k. After the calculation of the angle α^*, the correction profile is created, mathematically projected and the correction is obtained from the comparison of these two profiles. Finally, this correction should be applied on the *actual profile*.

In order to preliminary validate the proposed method a numerical approach was applied. The subsequent steps were followed:

- Mathematical creation of the thread profile with an arbitrary thread angle (this profile will be named *"reference profile"* and the angle will be α_{ref}^*),
- Projection of this profile in order to obtain the *actual profile*,
- Calculation of the angle α_P^*,
- Known α_P from the projection of the thread model with α equal to 60°, calculation of the factor k,
- Calculation of α^* from α and k,
- Projection of the correction profile and calculation of the correction for the actual profile
- Final profile obtained from the correction of the actual profile.

Figure 85 shows a comparison between the differences obtained applying two different correction methods: the blue line is obtained with the proposed correction method, while the red line is referred to the correction using a correction with a fixed thread model using an angle equal to 60°. In this preliminary evaluation is taken into account a M30 thread with an α_{ref}^* equal to 55°. It is clear that the final corrected profile will be much more distorted and far from the real one (on the section plane) if the correction follows a model largely different from the reference profile.

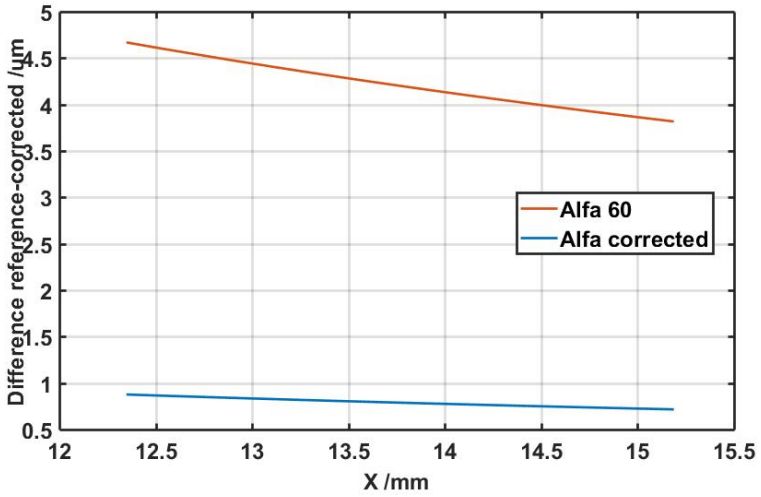

Figure 85 Comparison between different correction methods.

Subsequently isnecessary to verify the difference between the angle α^* and α_{ref}^* in order to understand how reliable is the proposed correction method and in particular how the angle obtained using the coefficient k is comparable with the reference angle. This phase proceeds with this numerical verification thanks to the numerical approach developed. The profile is mathematically generated and this implies that the angle α_{ref}^* is well known. In *Figure 86* the trend of the difference $\alpha_{ref}^* - \alpha^*$ is presented as a function of the angle α_{ref}^* (thread angle used for the creation of the profile) and parametrized on the external diameter of the thread. As shown, the differences became significant only for thread angles different from the nominal angle, therefore for distorted threads.

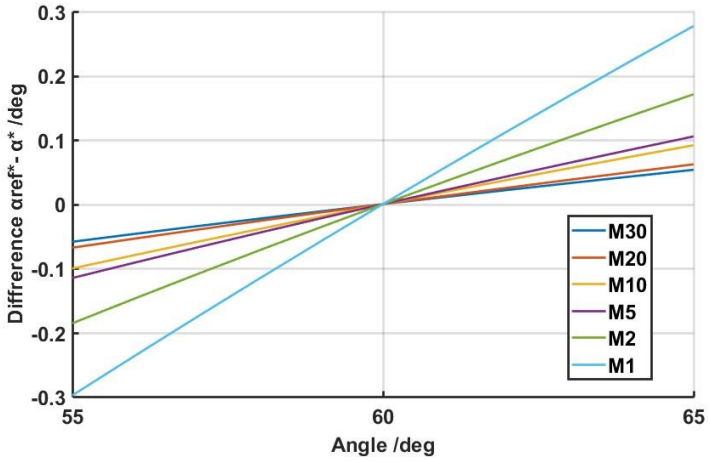

Figure 86 Difference between the reference angle and the angle obtained with the correction method.

In order to quantify the effect of the difference α_{ref}^{*}- α^{*}, in Table 42 the pitch diameter are calculated on two examples of threads (M30 and M1) with a thread angle α_{ref}^{*} equal to 55°.

Type of thread	**Reference pitch diameter [mm]**	**Pitch diameter after correction [mm]**	**Difference between the diameters [µm]**
M30 passo grosso	28.0572	28.0574	0.2
M1 passo grosso	0.8612	0.8613	0.1

Table 42: Effect of the difference between the angles on the notch diameter

The difference between the reference diameter and the diameter calculated after the correction demonstrates that the assumption $k = {\alpha_P^*}/{\alpha_P} = {\alpha^*}/{\alpha}$ is acceptable in this preliminary phase. In fact, even for thread angles largely different from the nominal one (α_{ref}^{*}- α^{*} = 5°), the errors reach maximum values of 0,1 or 0,2 µm.

Extension of the correction method to non-symmetric threads

After the preliminary evaluation for the symmetric profiles (the evaluation were done on the thread angle α, assuming $\beta = \gamma = \alpha/2$), the method was extended to the non symmetrical threads. Moreover, the need to apply a different correction on each flank, is strictly releated to the non ideal symmetry of the real profile: each flank is characterized by a different angle therefore requires a different and proportional correction. Moreover, for a preliminary validation, the method is applied to real images, and then are developed also the algorithms for parameters calculation and extraction. The measurement procedure follows the subsequent steps:

- Acquisition of the thread image;
- Calculation of external diameter and pitch;
- Extraction of the separated flanks of the thread;
- Linear fitting (1st degree) on the points of the flanks and evaluation of the angles β^{*}_{p}, γ^{*}_{p} and calculation of the distance $x_0{}^{*}_{p}$ (see *Figure 87* for the notation);
- Using the external diameter and pitch found in the previous step, calculation of the projection of a reference profile (characterized by α equal to 60°, β and γ equal to 30°);

- From the projected reference profile is extracted through linear fitting, the angles β_p and γ_p and the distace Δx_0;
- Obtained the angles β_p, γ_p, β^*_p and γ^*_p is possible to calculate the parameters $k_\beta = {\beta^*_p}/{\beta_p}$ e $k_\gamma = {\gamma^*_p}/{\gamma_p}$;
- Accepted the relation $k_\beta = {\beta^*_p}/{\beta_p} = {\beta^*}/{\beta}$ (consequently $k_\gamma = {\gamma^*_p}/{\gamma_p} = {\gamma^*}/{\gamma}$) is possible to calculate β^* and γ^*;
- Calculation of $x_0^* = x_0^*{}_p - \Delta x_0$;
- Calculation of the projection of the profile obtained with the previously calculated parameters;
- Calculation of the correction;
- Calculation of the thread parameters.

All steps will be analysed in the next sections, in order to clarify and explain the processes developed for the correction of the image.

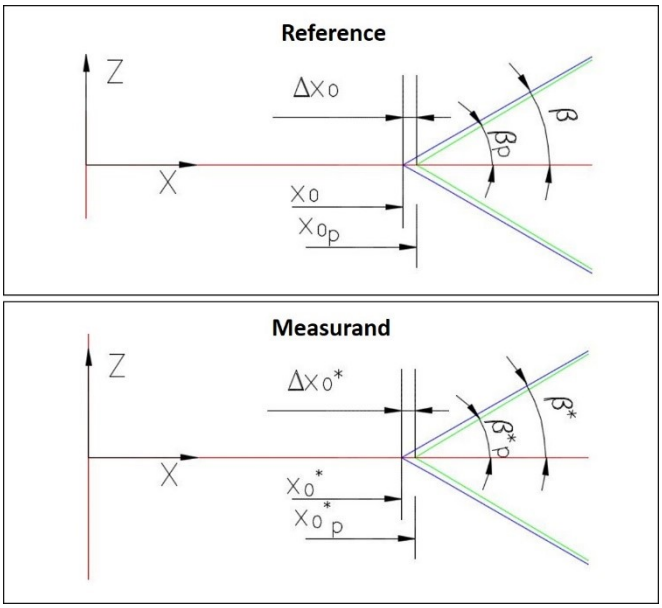

Figure 87 Notation used for the description of the geometry for the reference threat (on top) and for the acquired thread (on bottom). Green lines are related to the shadow or projected profiles, blue lines represent the profiles on a axial plane

Acquisition of the thread image

Figure 88 shows an example of the image obtained from the optical measuring system. Through common image-processing algorithms, the edge is recognized and the points are transformed in Cartesian coordinates.

Figure 88 Example of an image obtained from the optical system

The result of these procedures is presented in *Figure 89*. The image-processing techniques are not presented because are not available and property of the optical system producer.

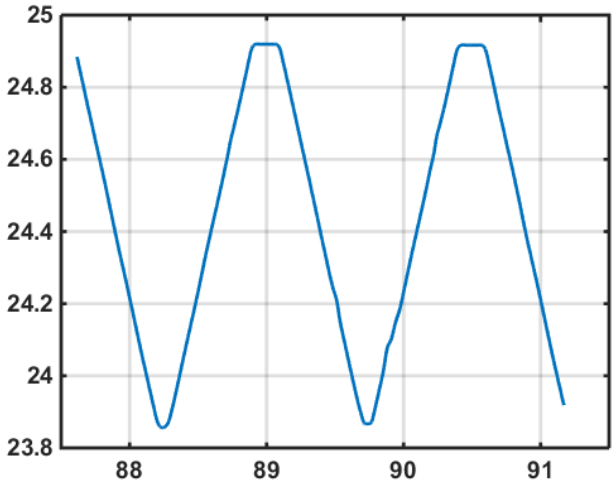

Figure 89 Example of an acquired profile

Directly from the data shown in *Figure 89*, the threads parameters not influenced by the shadow are calculated. As presented in *Figure 90*, pitch and external diameter are calculated as mean value of all the values calculated on all the different threads.

After the evaluation of the external diameter and pitch, the process proceeds in parallel with two different elaborations: calculation of the shadow of the *reference profile* (projection of a thread with pitch and external diameter equal to the measured ones but thread angle and geometry equal to the reference) and preliminary operations for the calculation of the angles β^*_p e γ^*_p and the coordinate $x_0{}^*_p$ on the acquired profile.

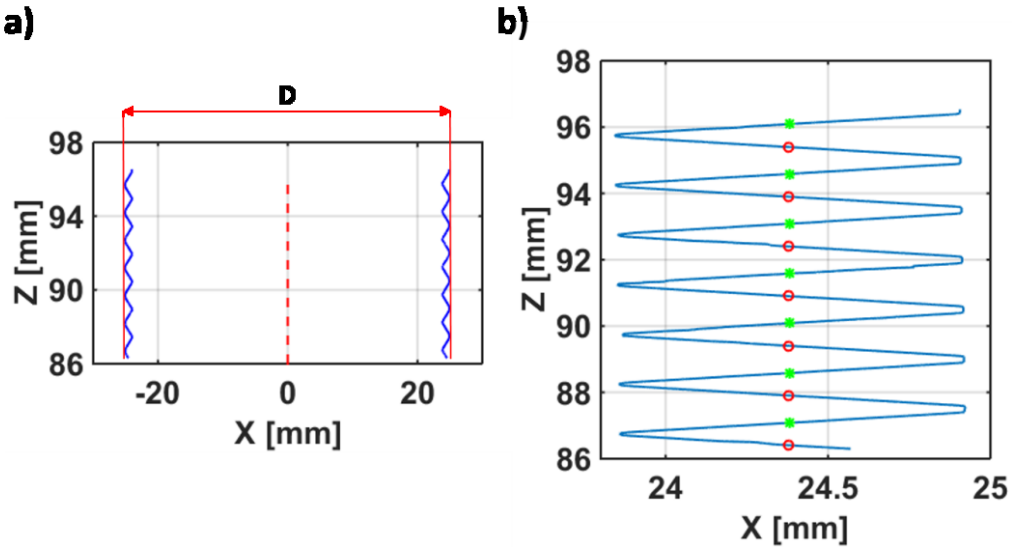

Figure 90 Determination of the external diameter (a) and pitch (b).

Projection of the reference

The projection is obtained using the mathematical description of the shadow described in the previous part with the pitch and the external diameters acquired from the image and the angles β e γ *equal to 30°*. Each single flank is singularly projected; after the projection, applying a linear fitting, are calculated the angular coefficient of the projection (in order to calculate the angles β_p e γ_p) and the coordinate x_{0p} as the intersection of the two fitted lines (see *Figure 87*). At the end of this phase the angles β_p and γ_p and the coordinate x_{0p} (used for the evaluation of $\Delta x_0 = x_0 - x_{0p}$) are obtained.

Elaboration of the acquired profile

In order to calculate the angles of the flanks, is necessary to isolate every single flank of the thread. Thus, is necessary a preliminary phase in which the points are indexed and the flanks are cut. The result of this phase is shown in *Figure 91*. All the subsequent steps are applied on a single flank, separately.

Referring to the example reported in *Figure 91* (in particular the zoom shown in the small window on the right), a linear fitting is applied on the different flanks, the red and the blue one, and the angles β^*_p e γ^*_p are calculated. Moreover, from the intersection of the two lines could be calculated $x_0{}^*_p$.

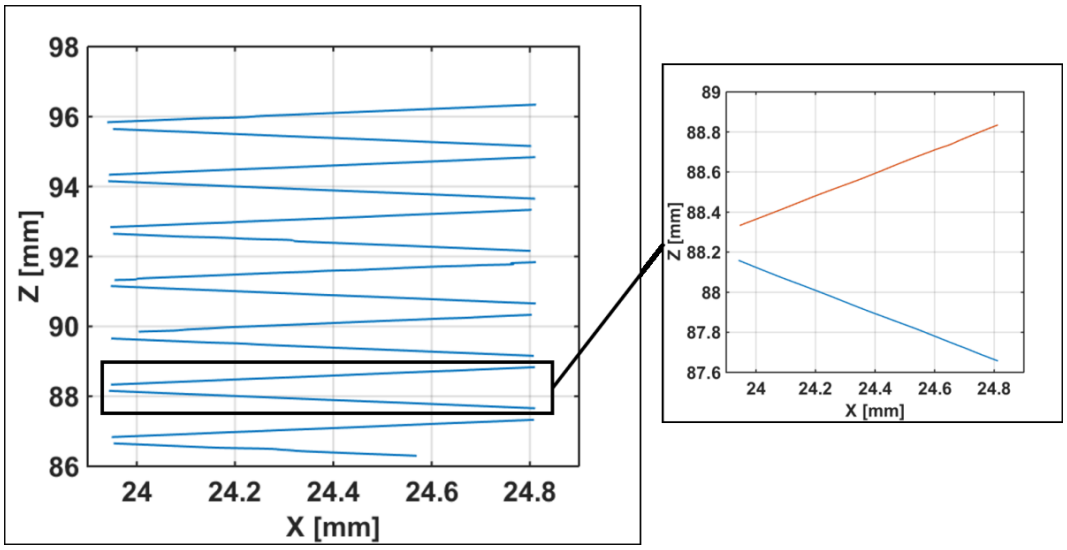

Figure 91 Elaboration of the acquired profile

Calculation of the correction factor

After the evaluation of the angles β_p and γ_p for the reference and after the measurement of the angles β^*_p and γ^*_p for the acquired thread, the factors k_β and k_γ could be calculated.

The relations $k_\beta = {\beta_p^*}/{\beta_p} = {\beta^*}/{\beta}$ and $k_\gamma = {\gamma_p^*}/{\gamma_p} = {\gamma^*}/{\gamma}$ gives the values of angles β^* e γ^*. This procedure should be developed for each flank of the image. Moreover, assuming $\Delta x_0^* = \Delta x_0 = x_{0_p} - x_0$, and extracting $x_0{}^*{}_p$ from the profiles, $x_0{}^*$ ($x_0^* = x_{0_p}^* - \Delta x_0$) is obatained

Shadow creation and correction

At this point the calculation of the projection of the profile created from β^*, γ^* and $x_0{}^*$ is developed and the correction for the correspondent profile is finally obtained. *Figure 92* shows the results get after the correction, in which the not-corrected profile and the corrected one are both represented.

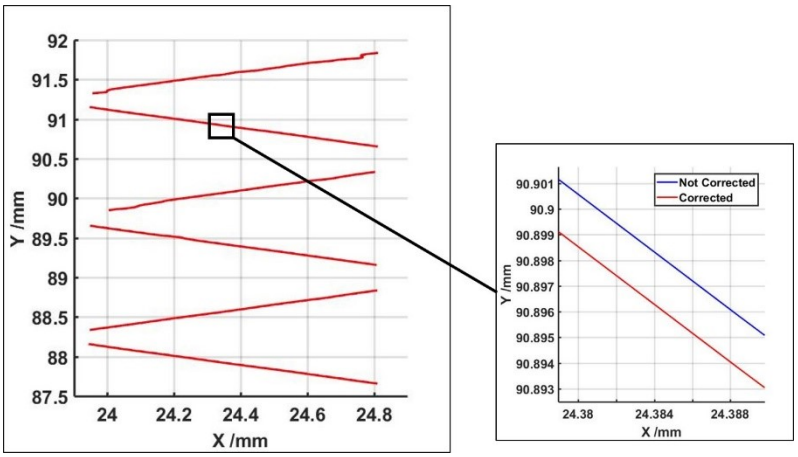

Figure 92 Zoom of the correction

The correction obtained with this procedure ensures different correction for each flank, because of the differences in the real angle values and the differences in x_0^*. *Figure 93* presents an example of an application on six different flanks of the same image: the image on the right clearly shows that every single flank needs a different and dedicated correction.

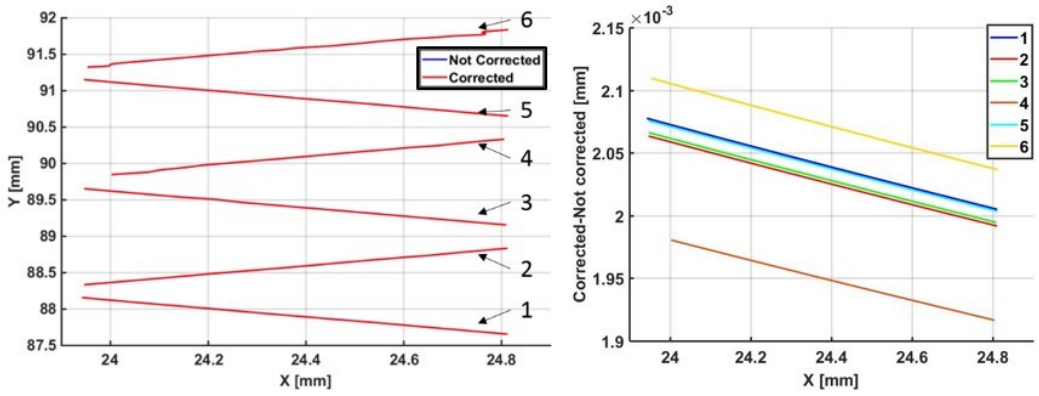

Figure 93 Correction obtained for six different profiles

At this point on the corrected profile are calculated the parameters of the thread.

Preliminary verification

A set of preliminary images were analysed in order to highlight limitations or problems related to the application of the method. Three different images were analysed and the results were compared with the calibration certificate of the sample. Three different repetitions were done. The nominal external diameter of the three samples was equal to 30mm, 35mm and 50mm and the nominal pitch is equal to 1.4mm for the M30 and 1.5 for the M35 and M50. The parameters used for the comparison were: external diameter

and pitch without any correction and pitch diameter, β, γ and α obtained from the corrected profile.

All the results are reported in tables Table 43, Table 44 and Table 45.

Sample 1						
Repetition	**De**	**P**	**Dm**	**α**	**γ**	**β**
1	49.9904	1.5001	49.0314	59.9339	29.8259	30.1080
2	49.9903	1.5001	49.0311	59.9232	29.8174	30.1058
3	49.9903	1.5001	49.0311	59.9284	29.8209	30.1074
Mean	49.9903	1.5001	49.0312	59.9285	29.8214	30.1071
Std.dev.	0.0001	0.0000	0.0002	0.0053	0.0043	0.0011
CERTIFICATE	49.9996	1.5001	49.0248	59.6964	29.9697	29.7267
DIFFERENCE	0.0093	0.0000	-0.0064	-0.2321	0.1483	-0.3804

Table 43 Sample number 1: results expressed in mm for diameters and pitch, deg for the angles

Sample 2						
Repetition	**De**	**P**	**Dm**	**α**	**γ**	**β**
1	35.0059	1.5003	33.9596	60.1838	29.8652	30.3186
2	35.0059	1.5003	33.9605	60.2376	29.9553	30.2823
3	35.0059	1.5003	33.9606	60.2363	29.9495	30.2867
Mean	35.0059	1.5003	33.9602	60.2192	29.9234	30.2959
Std.dev.	0.0000	0.0000	0.0005	0.0307	0.0504	0.0198
CERTIFICATE	35.0111	1.4999	33.9456	59.9650	29.0044	29.9606
DIFFERENCE	0.0052	-0.0004	-0.0146	-0.2542	-0.9190	-0.3353

Table 44 Sample number 2: results expressed in mm for diameters and pitch, deg for the angles

Sample 3						
Repetition	**De**	**P**	**Dm**	**α**	**γ**	**β**
1	30.2428	1.4107	29.3432	60.0491	29.8576	30.1915
2	30.2426	1.4107	29.3430	60.0480	29.8571	30.1909
3	30.2425	1.4107	29.3429	60.0481	29.8512	30.1968
Mean	30.2426	1.4107	29.3431	60.0484	29.8553	30.1931
Std.dev.	0.0002	0.0000	0.0001	0.0006	0.0035	0.0033
CERTIFICATE	30.2510	1.4110	29.3328	60.1511	30.1681	30.9831
DIFFERENCE	0.0084	0.0003	-0.0103	0.1027	0.3128	0.7900

Table 45 Sample number3: results expressed in mm for diameters and pitch, deg for the angles

From the analysed images the measurements present a good repeatibility, but from the comparison of the results with the certified values the differences are significant. From an analysis of the results, the error could be related to the differences obtained on the external diameter. The external diameter is not corrected and directly get from the image. The difference obtained on this parameter highlights some problems on the alignment of the sample and some problems on the evaluation of this diameter. This drift on the external diameter implies possible distortions also on the flanks and required additional investigations before developing the last and final correction method.

Extended and final correction method

The last step of the correction development is related to the generalization to every thread with no limitations on the thread and flank angles. The correction should be suitable and adjustable automatically for every type of thread. In order to reach this result, all the information should be gained from the shadow, moreover the model used for the creation of the correction should be developed starting from the shadow, with no preliminary information. The previous correction model requires a thread model for the correction (in the particular case the thread angle was fixed). In all the previous parts the thread angle α is assumed equal to 60° and this implies that β and γ are equal to 30°. However, the model should be extracted from the shadow profile also for geometries that are far from the standard one (characterized by asymmetric threads and different from 60°). Only if the correction method is obtained directly from the shadow, without any preliminary information, a flexible and largely applicable correction method for straight flanks could be provided.

The only well known aspect is that because of the helicoidal revolution of the threads, the projection reduces the section. The obtained profile is no more perfectly straight, but could be simplified using fitting algorithms. This means that the only useful information from the shadow are:

- Pitch
- External diameter
- Angle of the fitting line of the shadow

In order to develop a general and flexible correction method, it is necessary that the correction method and algorithms are only function of these parameters. For the creation of the correction method is used the intersection point between the shadow of two flanks (intersection point on the external diameter). This point should not be distorted and from this point is possible to identify the flank angle of the model. For this step, different solution are possible:

- Use of the shadow projection as a model
- Round of the angle calculated on the shadow on the nearest integer
- Use of a constant delta independent from the thread parameters
- Creation of a proportional correction, function of the thread parameters.

Each of these possible solutions present advantages and disadvantages.

The use of the shadow projection as a model permits to use the shadow profile directly. But using the shadow as a reference is possible to obtain a projection that is more distorted than the shadow, moreover in the direction of the reduction of the section. This method would cause an amplification of the difference between the projection and the projection of the reference.

The round of the angle is too arbitrary. In this case the reference model would be bigger (referring to the section) respect the shadow profile, but it is independent from the thread parameters, moreover it is not considering proportion between the delta and the thread parameters. The error introduced could be inversely proportional to the accuracy of the thread angle (e.g. in the case of a flank with a shadow angle of 30.02° would be rounded to 31°).

The use of a constant delta would maintain constant the difference between the shadow and the model of the thread. In addition, this solution causes variable error and is not proportional to the parameters.

At the end, the identification of a proportional correction is the most corrected way to proceed from a formal point of view. It is necessary to identify the relation that links the measured parameters directly to the variation of the angle for the creation of the reference profile. In order to find the correction the relations are extracted through a mathematical procedure.

$$z = z_0 - x\tan\beta + \frac{p\varphi}{2\pi} \quad 4.16$$

From equation 4.16 and using the relation previously presented,the calculation of the projection of a random point *L* could be done

$$z_L = z_0 - \frac{x}{\cos\varphi_L}\tan\beta + \frac{p\varphi_L}{2\pi} \quad 4.17$$

where

$$\varphi_L = \sin^{-1}\left(-\frac{\pi x}{p}\tan\beta + \sqrt{\left(\frac{\pi x}{p}\tan\beta\right)^2 + 1}\right) \quad 4.18$$

Considering two points of the profile characterized by the coordinates x_1, z_1 and $x_2,\ z_2$, it is possible to calculate the projection of these points and then, from this projection evaluate the angle of the interpolating line (assuming this angle similar to the one obtained through the fitting on all the points).

Replacing the coordinates of two different points in 4.17 is described the projection: starting from these points the angle β is obtained. Then, defining $\Gamma = \frac{z_{L2}-z_{L1}}{x_{L2}-x_{L1}}$, considering two different angles φ_{L1} and φ_{L2} (evaluated starting from 4.18) could be obtained the relation between Γ x, β and p. From the extracted relation (the explicit expressions are not shown because are involved in a patenting process, moreover protected by an agreement) is possible to evaluate $\beta_p = \tan^{-1}\Gamma$. In the case of the thread model could be necessary to calculate β starting from β_p. The relation $\beta = f(\beta_p)$ was studied with a numerical simulation and a sensitivity analysis, changing all the parameters and analysing the obtained difference between β and β_p.

The flank angle β was changed between two boundaries, called β_m and β_n, the diameter between D_m and D_n, the pitch between $p_m$and p_n. A non-disclosure agreement with Marposs S.p.A. prevents the publication of the numerical values used for simulations (for the same reason the scales of the axis in the next figures are masked). The extreme values were chosen in between the most common thread dimensions on the market, not considering particular relations between diameter, pitch and angle. The evaluation of the relation was developed on 15.967.320 different simulations. As an example of the obtained trend, the difference between the angles (delta) for a particular value of β (named β_i) is shown in Figure 94.

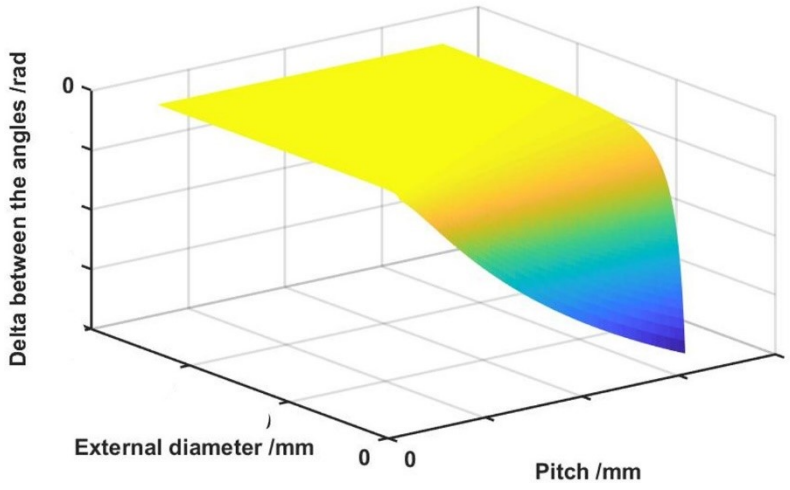

Figure 94 Delta obtained varying pitch and diameter for a particular flank angle β_i

From these results the trend of the mean value is obtained, moreover the trend of the standard deviation of the delta, function of the model angle. Figure 95 and Figure 96 show the parametrized curves for β equal to β_i, parametrized on the pitch of the thread (only some simulated pitches are shown)

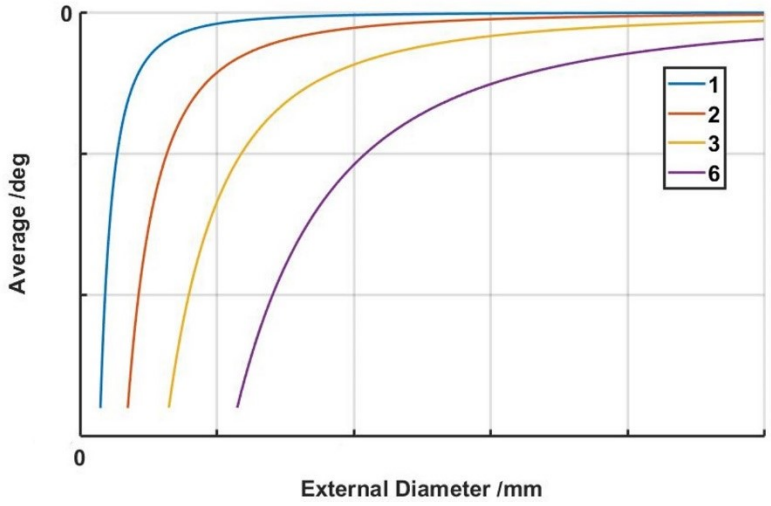

Figure 95 Trend of the mean value of the difference, function of the diameter and parametrized on the pitch

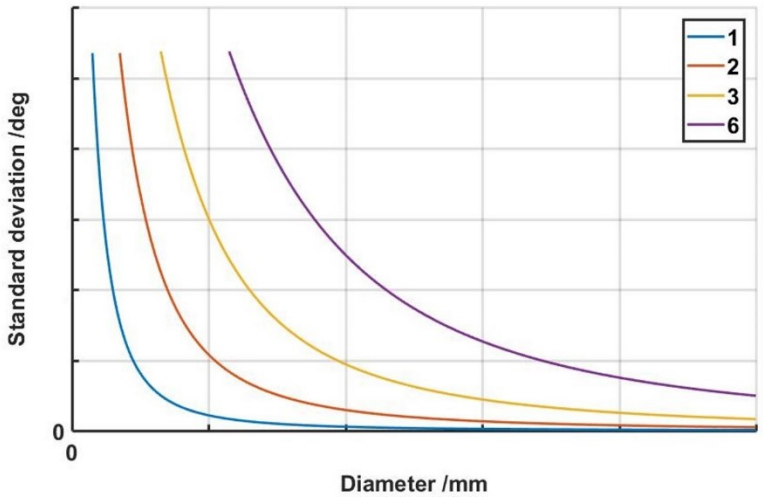

Figure 96 Trend of the standard deviation of the difference function of the diameter and parametrized on the pitch

In order to obtain a useful relation, the ratio between pitch and diameter was considered, the results with no dimension are shown in *Figure 97*. The standard deviation is calculated in order to generalize the results for all the β angles. The delta increases with the ratio, the difference $\beta - \beta_p$ causes the negative sign of the delta.

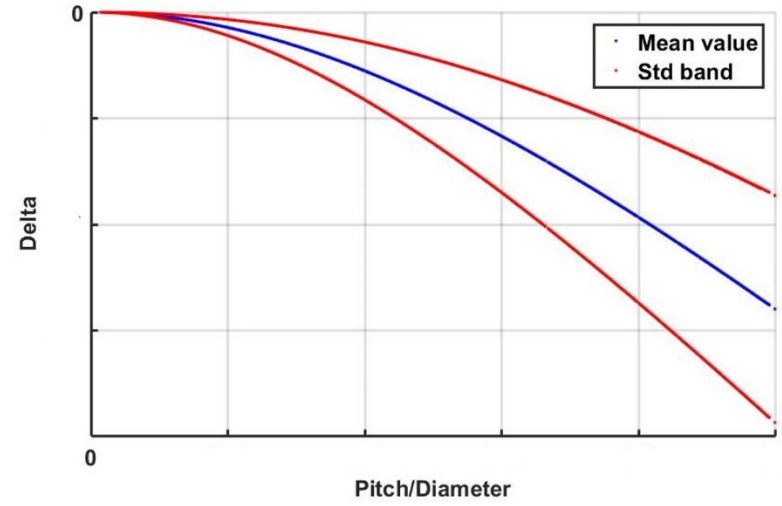

Figure 97 Trend of the mean difference and standard deviation band in function of the ratio pitch on diameter

The relation is obtained following the mean value: this is a simplification, but permits to follow the trend in function of the parameters obtained directly from the shadow projection.

Considering that the ratio between the pitch and the diameter is generally very small (around the 10% for the ISO metric threads), *Figure 98* shows the trend for this reduced number of values.

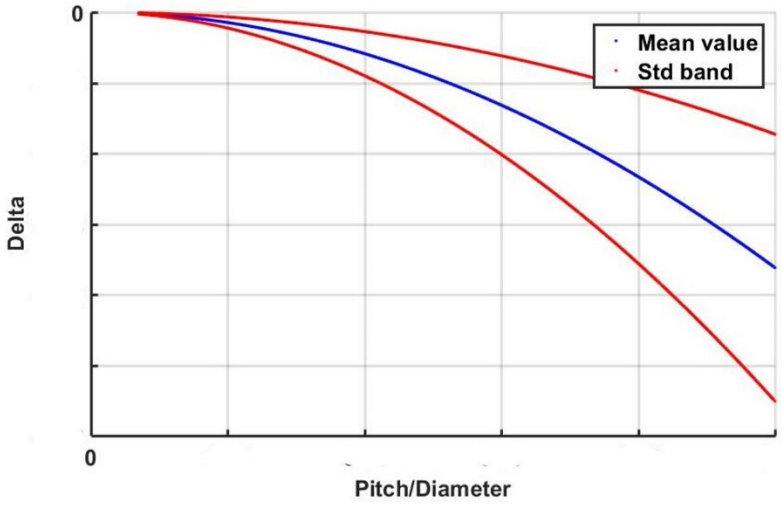

Figure 98 Trend of the mean difference for ratio of pitch on diameter lower than 10%

From the obtained data, the determination of the coefficients of the equation could be developed. The exponential model of the equation is expressed in 4.19

$$\Delta = f\left(p/D\right) = a\left(p/D\right)^{b} \quad 4.19$$

The coefficients were calculated through least square fitting.

The delta is expressed in degrees and is equal to the difference β of the model (or eventually is the same for γ) and β_p of the projection (or eventually γ_P).

So, the final correction model applicable to every type of straight threads, symmetric and asymmetric, with no restrictions to the thread angle with no preliminary information, will follow the subsequent steps:

- Acquisition of the shadow profile;
- Calculation of the parameters not influenced by the projection (external diameter and pitch)
- Extraction of the flank profile
- Linear fitting on the flanks for the calculation of the projection angle (angles β^*_p and γ^*_p);
- Calculation of Δ using the previously presented relation $\Delta = f(p\ /\ D)$
- Creation of a reference profile (β and γ calculated using Δ, $\beta = \beta_p^* + \Delta_\beta$ and $\gamma = \gamma_p^* + \Delta_\gamma$);
- From the projection of the reference evaluation of the angles β_p and γ_p and the distance Δx_0;
- From the angles β_p, γ_p, β^*_p and γ^*_p are calculated the parameters $k_\beta = \beta_p^* / \beta_p$ and $k_\gamma = \gamma_p^* / \gamma_p$;
- Assuming the relation $k_\beta = \beta_p^* / \beta_p = \beta^* / \beta$ (and the same $k_\gamma = \gamma_p^* / \gamma_p = \gamma^* / \gamma$) are calculated the angles β^* e γ^*;
- Calculation of $x_0^* = x_0^*{}_p - \Delta x_0$;
- Creation of the projection of the profile characterized by x_0^*, β^* and γ^*
- Calculation of the correction;
- Calculation of the thread parameters.

A scheme that resumes the procedure is presented in *Figure 99*. The image shows the procedure for the angle β, same steps are followed for the angle γ

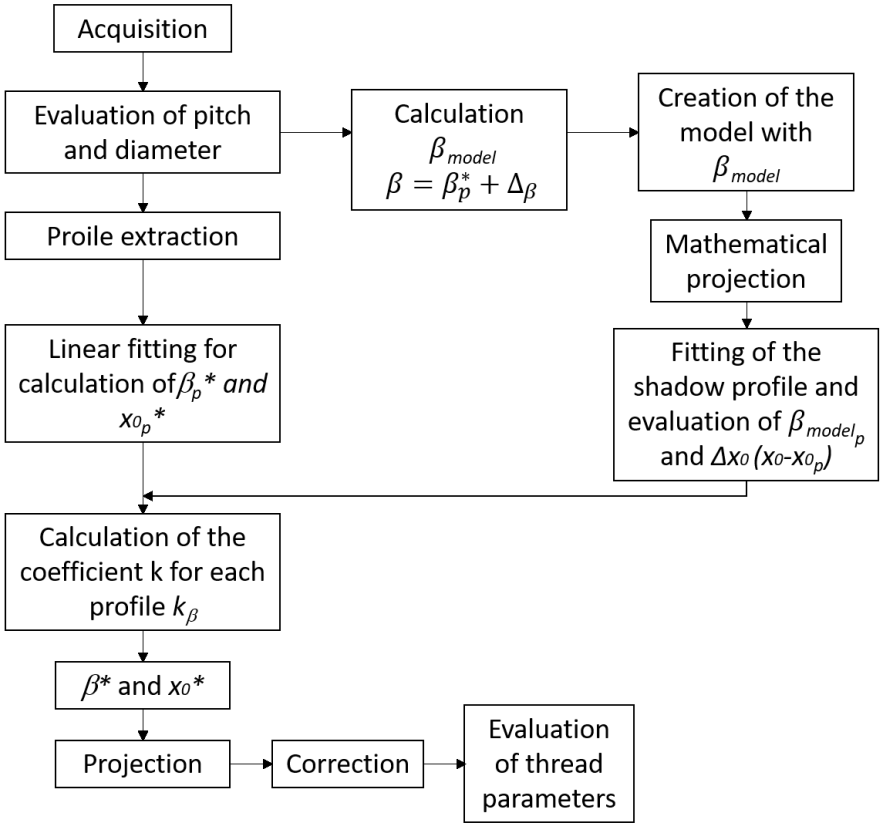

Figure 99 Scheme of the extended correction

Numerical validation

In order to numerically validate the procedure and the final algorithm, numerically generated shadow were used. These shadows are then imported as images and used as the result of the optical measuring system. A first verification was developed on an ISO M30 coarse pitch and M20 coarse pitch threads, applying the procedure for the calculation of the pitch diameter to the geometric profile (the profile from which the shadow is calculated) and comparing the value with the one calculated after the correction of the shadow profile.

Therefore, the subsequent steps characterize the applied procedure:

- creation of the geometry using the nominal dimensions (from standard values);
- calculation of the pitch diameter in order to verify the algorithm for the calculation of the parameter;
- creation of the shadow;
- application of the correction method, calculation of the pitch diameter and comparison.

After this verification on two different cases, different threads were numerically generated and in this case the comparison was done only between the nominal diameter (pitch diameter calculated on the generated profile, before the projection) and the corrected one.

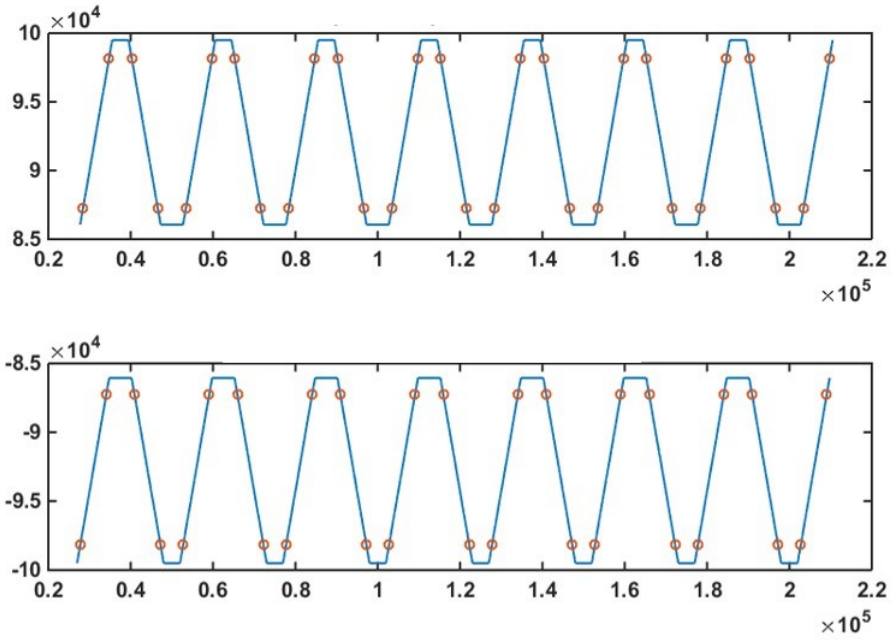

Figure 100 Example of an M20 profile, top and bottom profile

Figure 100 shows an example of the shadow profile obtained for the M20 thread. In this figure could be identified the points in which the thread will be cut for the identification of the flanks and the application of the different corrections.

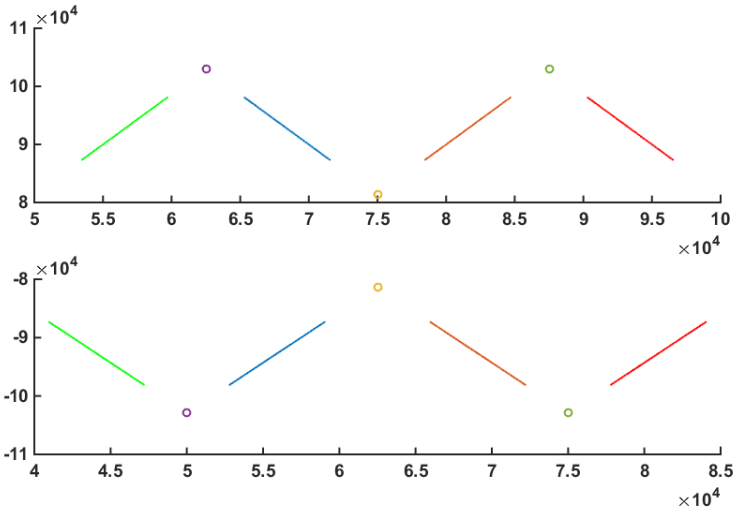

Figure 101 Example of the extraction and separation of the different flanks

The result of the flank extraction process is presented in Figure 101. The points presented in the figure are the result of the fitting and intersection steps (described in the previous paragraph). Instead Figure 102 shows different flanks in the same image, after isolation and separation steps. On these profiles will be applied the correction.

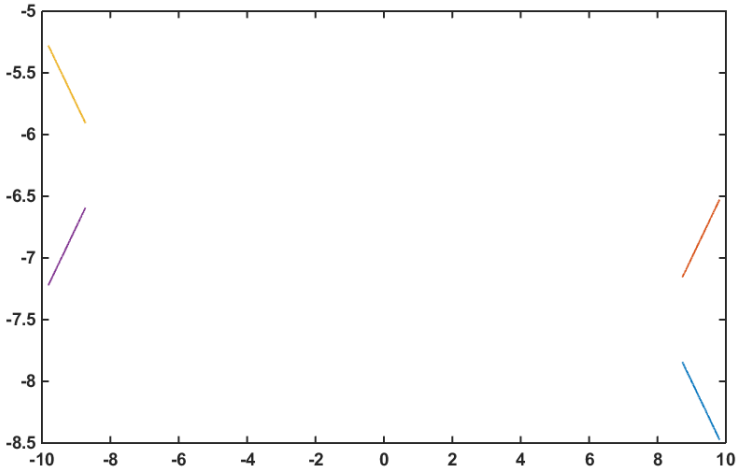

Figure 102 Example of the projected flanks isolated and separated

After the correction, the pitch diameter is calculated, as shown in *Figure 103*.

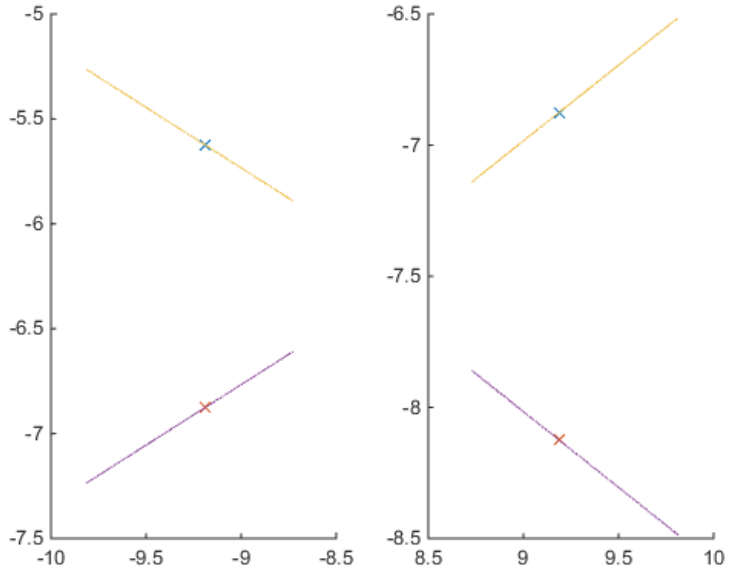

Figure 103 Example of the calculation of the pitch diameter for M20 coarse pitch

All the verified geometries are presented in Table 46. The standard diameter is the value taken from the catalogue. Only the first two samples present the standard diameter, because they are the only one characterized by a standard geometry with references to

catalogues. The nominal diameter is calculated on the numerical profile used for the generation of the shadow and the pitch diameter after correction is calculated on the shadow profile, after the application of the correction method.

External Diameter	γ [°]	β [°]	Nominal pitch diameter [mm]	Pitch diameter after correction [mm]	Standard diameter [mm]
20	30	30	27.766	27.7268	27.727
30	30	30	18.3762	18.3762	18.376
30	29	32	27.7896	27.7895	-
30	31	33	27.9584	27.9583	-
30	30	15	26.6173	26.6173	-
36	33	18	32.7606	32.7606	-

Table 46 Verified geometries and obtained pitch diameters

From the presented results could be stated that the correction method is applicable to every type of thread, with different flank angles, symmetric and asymmetric. The differences on the diameters between the nominal value and the value obtained after the correction is lower than 1 μm in each condition. This confirms the flexibility and reliability of the developed correction method.

Applied corrections

In the following are shown the different correction applied on all the different flanks. This images highlight the flexibility and in particular the capability of the correction method to fit the different situations and geometries. The correction applied on the symmetric threads are not shown, because in this case the nominal geometry implies same correction for both the flanks.

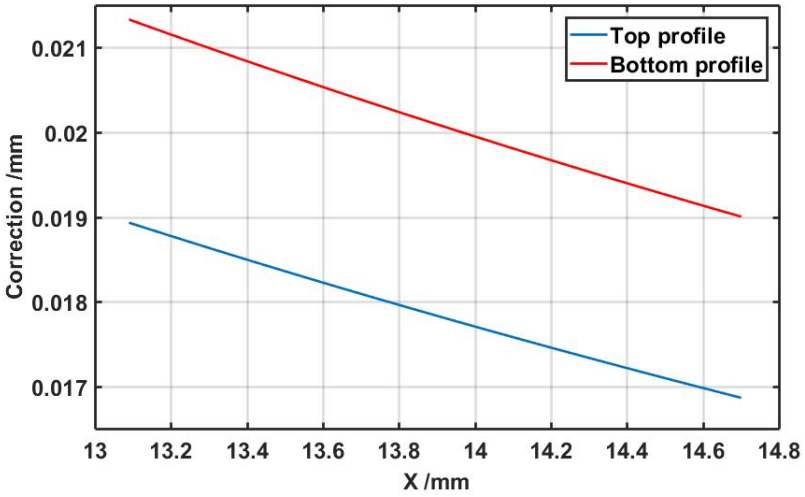

Figure 104 Correction for the different flanks in the case of diameter 30 mm, γ=29° and β=32°

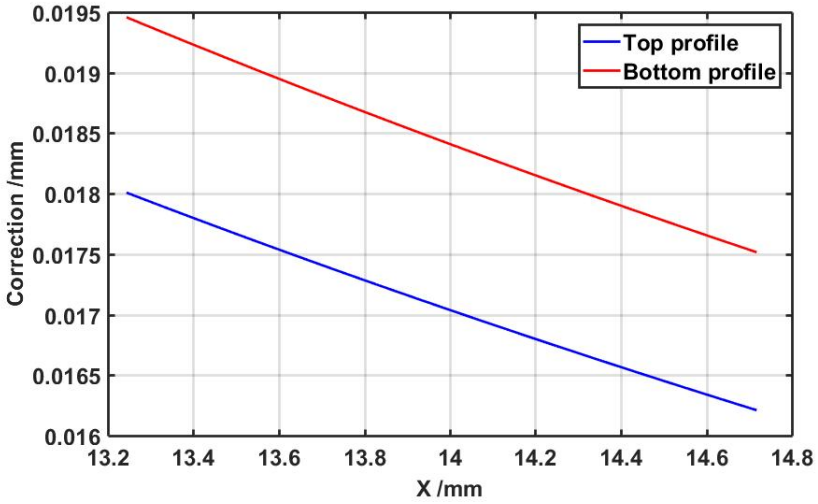

Figure 105 Correction for the different flanks in the case of diameter 30 mm, γ=31° and β=33°

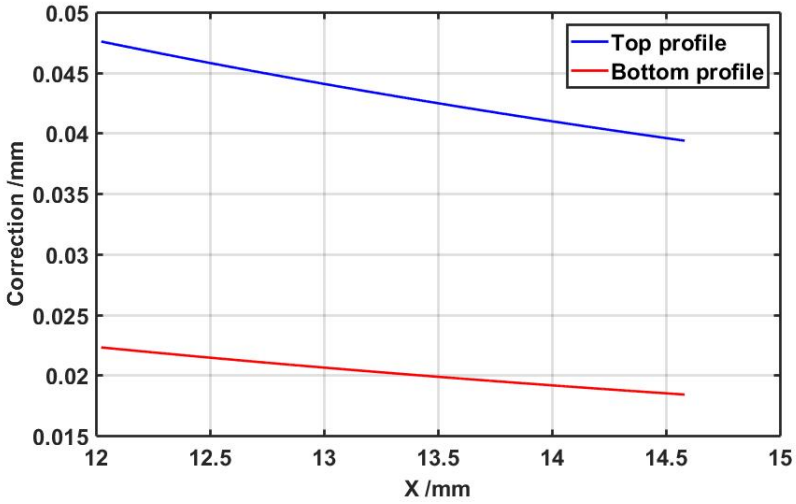

Figure 106 Correction for the different flanks in the case of diameter 30 mm, γ=30° and β=15°

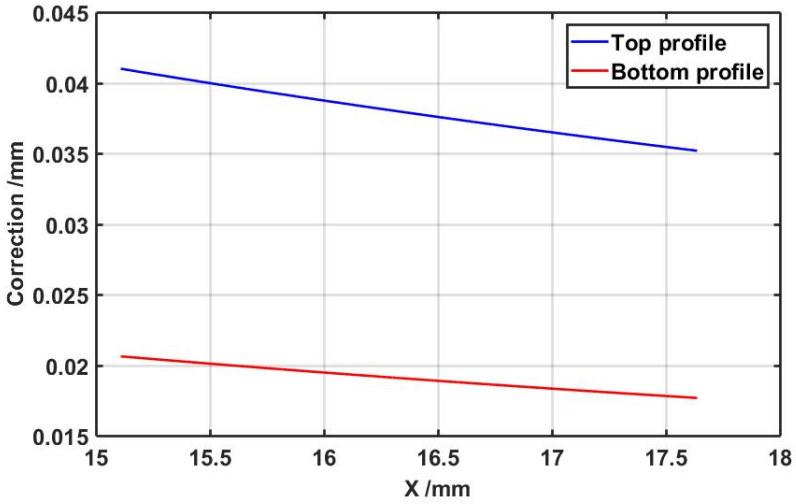

Figure 107 Correction for the different flanks in the case of diameter 36 mm, γ=33° and β=18°

Comparing the corrections reported in Figure 104, Figure 105, Figure 106 and Figure 107 could be understood how the algorithm calculates in a completely different manner the corrections for each flank and for each different geometry.

In order to highlight these differences, all the correction profiles are plotted together in *Figure 108*. The results for the diameter equal to 30 mm are not shown; on the contrary, the profile characterized by a diameter of 36 mm is not presented in the same image because of the scale: it will cause an extension of the x-axis, causing a bad and not completely clear representation.

The blue line in Figure 108 represents the ISO 30 standard thread. This would be the common correction for every different profile in the case of a non-flexible correction

method based on a fixed thread model. The differences and errors associated with the application of a fixed correction would be relevant in the case of a distorted thread (like the light blue one).

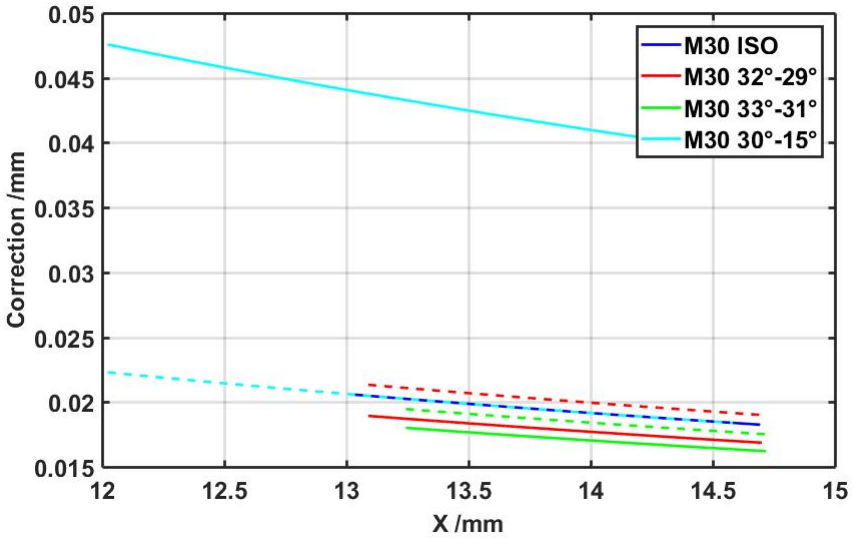

Figure 108 Comparison between all the corrections

Experimental verification

For the verification of the correction method were used images of calibrated threads. The standard procedure used is as follow:

- **Scan of the threads**: measure of the threads using the Marposs measuring system. The obtained results, after the application of the edge detection techniques property of *Marposs S.p.a.* were saved as text files, with a resolution of 0.1 μm.
- **Import of the text files in Matlab:** the text file are imported in Matlab software for the elaboration. The two different profiles are saved in two matrices containing the axial coordinates and the heigths of the extracted profile.
- **Alignment:** the axis of the thread is aligned with the x axis of the reference system.
- **Identification of the crests and flanks:** using a thresholding technique the flanks (used for the correction and calculation of the pitch and pitch diameter) and the crests (used for the calculation of the external diameter) are identified and divided.

  .

- **Calculation of the external diameter:** the external diameter is calculated considering the most external point evaluated on the crests on the upper and lower profile.
- **Pitch calculation:** the pitch is calculated considering the intersection between a line parallel to the axis of the thread and the flanks. The final value is obtained as an average of the values calculated on all the upper and lower single threads. As previously said this evaluation could be done directly on the shadow profile.
- **Application of the correction algorithm:** after the calculation of the pitch and external diameter for each flank of the thread, the calculation of the correction for each flank is developed.
- **Calculation of the pitch diameter:** considering a line parallel to the axis of the thread, the coordinate of the point in which the distance between the flanks is equal to half pitch is calculated. The value of the diameter used for the comparison is the average one, obtained from all the flanks.

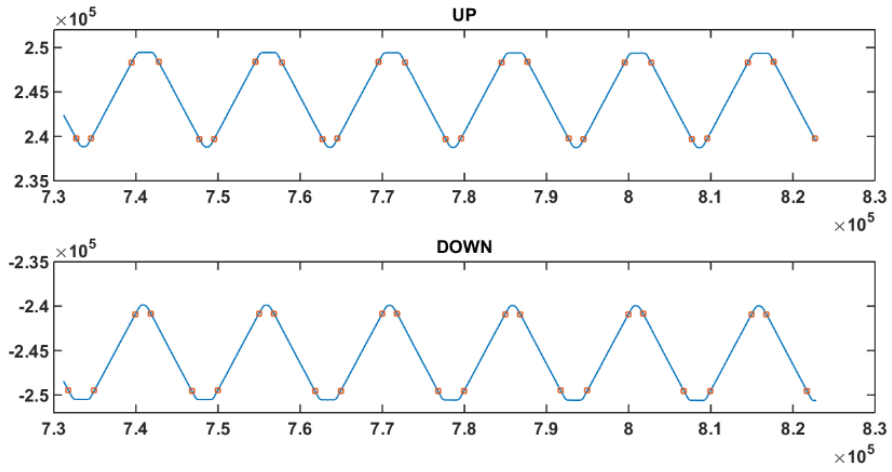

Figure 109 Example of acquired and aligned profiles. The values are expressed in one tenth of microns

The four different profiles used for the validation are presented in Figure 109.

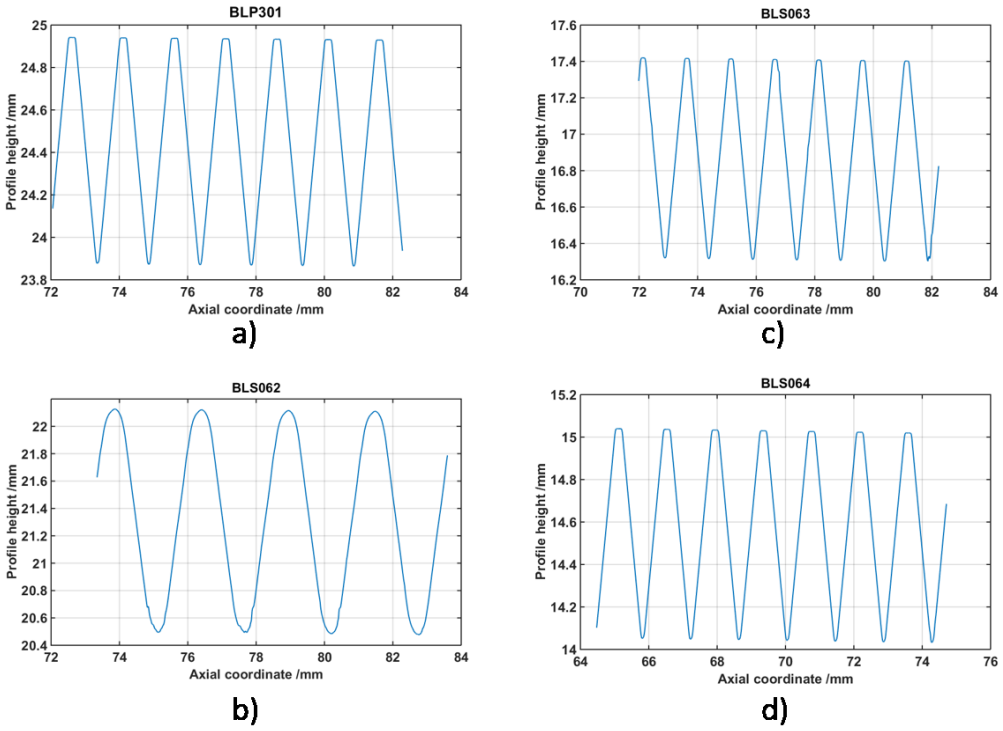

Figure 110 Upper profiles of the four different samples: a) sample 1, b) sample 2, c) sample 3 and d) sample 4

The reference values obtained using a Masterscanner measuring instrument from IAC are reported in Table 47.

	Sample 1		**Sample 2**		**Sample 3**		**Sample 4**	
	Sez. A	Sez. B	Sez. A	Sez. B	Sez. A	Sez. B	Sez. A	Sez. B
External diameter *[mm]*	49.997	49.999	44.480	44.481	35.012	35.014	30.250	30.249
Pitch diameter *[mm]*	49.025	49.025	42.875	42.875	33.945	33.946	29.333	29.333
Pitch *[mm]*	1.5	1.500	2.539	2.539	1.499	1.499	1.410	1.410
Thread angle *[deg]*	59.629	59.629	55.933	55.943	59.975	59.977	60.099	60.09

Table 47 Resuming table of the reference values

The parameters were evaluated on two different sections of the thread; for the comparison the mean between section A and section B were used. In the next tables (Table 48, Table 49, Table 50 and Table 51) are shown all the results obtained with the *Marposs* measuring system following the newly developed correction method. For each sample 4 different sections are measured, rotating the sample 90 deg after each measurement. The mean value and the standard deviation were calculated on the different values obtained for all

the profiles. The results for sample number 2 are calculated on a single thread, that's the reason why there's no standard deviation.

Sample 1								
	0 deg		**90 deg**		**180 deg**		**270 deg**	
	Media	**Dev. Std.**	**Media**	**Dev. Std.**	**Media**	**Dev. Std.**	**Media**	**Dev. Std.**
External diameter *[mm]*	50.002		50.002		50.002		50.002	
Pitch diameter *[mm]*	49.035	0.0005	49.035	0.0008	49.035	0.0011	49.035	0.0006
Pitch *[mm]*	1.499	0.001	1.499	0.001	1.499	0.001	1.499	0.001
Thread angle *[deg]*	59.833	0.0136	59.799	0.001	59.822	0.0144	59.820	0.01

Table 48 Results obtained with the correction method for sample 1

Sample 2								
	0 deg		**90 deg**		**180 deg**		**270 deg**	
	Media	**Dev. Std.**	**Media**	**Dev. Std.**	**Media**	**Dev. Std.**	**Media**	**Dev. Std.**
External diameter *[mm]*	44.482	/	44.483	/	44.482	/	44.481	/
Pitch diameter *[mm]*	42.893	/	42.887	/	42.887	/	42.908	/
Pitch *[mm]*	2.539	/	2.545	/	2.538	/	2.549	/
Thread angle *[deg]*	55.488	/	56.115	/	55.447	/	56.410	/

Table 49 Results obtained with the correction method for sample 2

Sample 3								
	0 deg		90 deg		180 deg		270 deg	
	Media	Dev. Std.	Media	Dev. Std.	Media	Dev. Std.	Media	Dev. Std.
External diameter *[mm]*	35.019		35.019		35.016		35.016	
Pitch diameter *[mm]*	33.959	0.002	33.959	0.001	33.960	0.003	33.959	0.001
Pitch *[mm]*	1.499	0.001	1.499	0.001	1.499	0.001	1.499	0.001
Thread angle *[deg]*	59.947	0.003	60.022	0.014	59.939	0.02	59.979	0.072

Table 50 Results obtained with the correction method for sample 3

Sample 4								
	0 deg		90 deg		180 deg		270 deg	
	Media	Dev. Std.	Media	Dev. Std.	Media	Dev. Std.	Media	Dev. Std.
External diameter *[mm]*	30.257		30.257		30.255		30.256	
Pitch diameter *[mm]*	29.345	0.001	29.347	0.001	29.347	0.001	29.347	0.0004
Pitch *[mm]*	1.4107	0.001	1.4111	0.001	1.4111	0.001	1.4111	0.001
Thread angle *[deg]*	60.073	0.018	60.071	0.01	60.070	0.019	60.060	0.009

Table 51 Results obtained with the correction method for sample 4

Table 52, Table 53, Table 54 and Table 55 show the results obtained for each sample, comparing the parameters obtained with the correction method and the reference values. The reference values are characterized by only two sections, in this case are reported the mean value and the difference between the two values (called Δ in the tables). Moreover in the column named "Difference" is calculated the difference between the mean value of the reference and the mean value of the corrected parameter.

	Corrected profile		**Reference**		**Difference**
	Avg	Dev.std.	Avg	Δ	
External diameter *[mm]*	50.002	0.0003	49.998	0.0022	**-0.004**
Pitch diameter *[mm]*	49.035	0.0008	49.026	0.0000	**-0.009**
Pitch *[mm]*	1.4996	0.0008	1.5001	0.0001	**0.0005**
Thread angle *[deg]*	59.818	0.0166	59.629	0.0006	**-0.189**

Table 52 Comparisons of the results for sample 1

	Corrected profile		**Reference**		**Difference**
	Avg	Dev.std.	Avg	Δ	
External diameter *[mm]*	44.482	0.0009	44.481	0.0010	**-0.001**
Pitch diameter *[mm]*	42.894	0.0087	42.875	0.0008	**-0.018**
Pitch *[mm]*	2.5429	0.0075	2.5399	0.0001	**-0.0030**
Thread angle *[deg]*	55.865	0.677	55.938	0.0090	**0.0731**

Table 53 Comparisons of the results for sample 2

	Corrected profile		Reference		Difference
	Avg	Dev.std.	Avg	Δ	
External diameter *[mm]*	35.017	0.0013	35.014	0.0014	**-0.004**
Pitch diameter *[mm]*	33.959	0.0018	33.945	0.0003	**-0.013**
Pitch *[mm]*	1.4997	0.001	1.4999	0.0000	**0.0002**
Thread angle *[deg]*	59.972	0.05	59.976	0.0019	**0.0039**

Table 54 Comparisons of the results for sample 3

	Corrected profile		Reference		Difference
	Avg	Dev.std.	Avg	Δ	
External diameter *[mm]*	30.256	0.0007	30.250	0.0016	**-0.006**
Pitch diameter *[mm]*	29.347	0.0006	29.333	0.0004	**-0.014**
Pitch *[mm]*	1.4112	0.0007	1.4109	0.0000	**-0.0003**
Thread angle *[deg]*	60.068	0.0158	60.094	0.0090	**0.026**

Table 55 Comparisons of the results for sample 4

The obtained results confirm the good repeatability of the correction method and of the measuring system. The pitch diameter presents a standard deviation lower than 1 µm and this confirms the repeatability of the correction on the different flanks.

From the comparison of the external diameters is possible to identify a systematic error: external diameter calculated on the shadow is bigger than the reference one. In average this difference is around 4 µm and the maximum obtained difference is equal to 6 µm in the case of sample 4 (clearly shown in Table 55).

For the pitch, the differences are lower than 1 µm, except for the sample number 2 in which the difference is equal to 3 µm, but this could be caused by the different profile and moreover the small number of measured profiles. Standard deviation in that case is high, as shown in Table 49 and Table 53, and considering them, the results are perfectly comparable.

The differences on the thread angle are small, in average equal to -0.022°, and the maximum difference, for sample 1, is 0.2°.

The pitch diameter presents differences lower than 20 µm for all the samples. In addition, in this case, the pitch diameter measured on the shadows is constantly bigger than the reference value. If we consider the difference on the external diameter as a systematic

error and we correct the pitch diameters, all the differences will be reduced under 10 μm. Moreover, considering the small differences on the angles, this means that the result of the correction is adherent with the reference, and the evaluated profile is finally parallel to the reference one.

Conclusions

In this chapter a method and a relative algorithm for the improvement of the thread measurement with optical systems was presented. The shadow generated from the measuring system is influenced by the geometry of the thread. In order to characterize the geometry of the thread according to ISO standards have to be applied a correction on the measured profiles. In this chapter firstly is analysed and quantified the effect of the thread geometry on the distortion caused by the shadow projection. Starting from these findings a newly correction method based is developed. A preliminary method needs a thread model defined from the user for error compensation. Then the influence factors are studied through sensitivity analysis and a generalized and completely self-adapting correction method is presented and verified. A fast and flexible method for the correction of straight, symmetric, asymmetric and not-metric threads. Differences between corrected values and calibrated ones in average equal to -0.022° for the thread angle and smaller than 10 μm for pitch diameter. The applied method ensures an enhancement of the performance of the measuring system, correcting the distortions associated with the nature and the characteristics of the sample under investigation.

5. Modelling of surface roughness effect in computed tomography dimensional measurements

X-ray computed tomography (CT) is increasingly used in dimensional metrology. However, several influence factors affect CT dimensional measurements. In particular, significant deviations can be observed between CT and tactile measurements especially when measuring parts with rough surfaces. The dependence of such deviations from surface morphology has not been thoroughly studied yet. Generally this effect was considered as a source of uncertainty, reducing the accuracy of the CT measurements. Nevertheless, a deep investigation demonstrates that this effect is systematic, thereby should be considered as a bias. In order to identify a clear and general relation between the surface morphology (in particular some surface roughness parameter) the experimental study is generalized through numerical simulations. These simulations confirm the experimental results, therefore used for determine the systematic effect on CT dimensional measurement for roughness profiles with different morphology.

Introduction

X-ray computed tomography (CT) has emerged over the last years as an advanced dimensional measuring technique (Kruth et al. 2011). Computed tomography has peculiar characteristics that ensure important advantages respect to other measuring systems. In particular, CT has the possibility of performing non-contact and non-destructive analyses on difficult to access geometries, including internal features. However, also the limitations of the CT technology are still not completely overcome and improved. Multiple error sources influence the final accuracy of the measuring system. Surface roughness of the scanned part represent one of these limitations (Schmitt & Niggemann 2010; Fiedler et al. n.d.). In particular, parts with highly rough surfaces – e.g. castings and additive manufactured (AM) parts – can cause significant deviations between CT and tactile dimensional measurements. The two measuring methods are characterized by different surface filtering characteristics and this causes differences in the final results (Salzinger et al. 2016). Tactile coordinate measuring machines (CMMs) produce a mechanical low-pass filtering which depends on the probe size: larger is the probe diameter, higher is the probability that the acquired points will lie only on the peaks of

the measured surface (Weckenmann et al. 2004). CT also generates a low-pass filtering, which has a different nature: it filters both peaks and valleys depending mainly on the unsharpness of CT images and on spatial discretization of the reconstructed volume using voxels of finite size (Kruth et al. 2011).

Different works in the past have dealt with the influence of surface roughness on CT dimensional measurements. Schmitt and Niggemann (Schmitt & Niggemann 2010) included the surface roughness as one of the uncertainty contributions related to the dimensional measurement of a sandblasted aluminium part with mean *Rz* of about 7 µm; a rectangular distribution was assumed and an uncertainty contribution of 0.6/2 times the mean *Rz* was calculated. Bartscher et al. (Bartscher et al. 2010) stated that an uncertainty contribution in the order of *Rz*/2 can be considered as an upper limit; in particular, effects of less than a quarter of *Rz* were determined for a cast aluminium workpiece with *Rz* up to 134 µm. All these works were mainly focused on how to include the surface effect in the uncertainty budget. On the contrary Aloisi et al. (Aloisi & Carmignato 2016; Aloisi et al. 2015) showed that correcting for systematic effects due to roughness enables a significant decrease of measurement uncertainty when dealing with AM parts characterized by high surface roughness. Boeckmans et al. (Boeckmans et al. 2015) observed an offset of *Rp* (maximum peak height of the profile in the sampling length) between CT and tactile CMM measurements in the case of turned surfaces. Although the abovementioned works document that an influence of surface roughness on CT dimensional measurements actually exist, the dependence of measurement deviations from surface morphology has not yet been studied in detail. There is no work still available that analyse the effect of different surface profiles on the systematic error. Moreover, no information is available so far about influences provided by CT surface filtering characteristics. In this chapter, the influence of surface roughness on CT dimensional measurements is investigated. The effect of surface morphology and filtering characteristics are considered and studied. In particular, the work aims at determining systematic errors of CT measurements with respect to reference tactile measurements. Since the effects of roughness for tactile measurements have already been studied (Weckenmann et al. 2004), this work focuses on the effects for CT measurements, considering the deviations from tactile measured points that ideally lie only on the peaks of the measured surface. Determining the systematic effects is relevant especially for measurements of surfaces with high roughness, as they produce larger bias, which should

be corrected for (rather than considered as uncertainty). In order to generalize the results is necessary to extend the experimental analysis with numerical analysis and simulation. The focus of this chapter is clearly the numerical generation of radiographic images in order to study extensively surface morphology effect. The entire work was published in CIRP annals (Carmignato et al. 2017).

Materials and methods

The work was organized basically considering an experimental campaign, focus of the work of a part of the research group, then this chapter is mainly focus on the sensitivity and numerical analysis. Experimental analyses were performed using various CT spatial resolution settings on samples with periodic roughness profiles having different bearing properties, i.e. different Abbott curves (ISO13565-2:1996). A short description of this part will be provided in order to understand the final results. As previously said, to extend the study, simulation analyses were implemented, considering a wider set of roughness profiles, imaged with a range of different voxel sizes.

Experimental analyses

Two samples were manufactured using two very different production processes: fused deposition modelling (FDM) and turning. These processes were chosen in order to obtain samples characterized by significantly different roughness profiles, for experimentally investigating the influence of different surface topographies (with dissimilar Abbott curves) on CT measurements. The first sample is a cylinder produced by FDM (nominal diameter 16 mm), using a 0.33 mm ABS wire. In this case, the workpiece is characterized by roughness profiles with the material more distributed on the peaks (higher Abbott curve than in the case of turned surfaces). The second sample is a turned aluminium cylinder, obtained using a conventional CNC lathe and designed to have four different zones with nominal diameters ranging from 9.9 mm to 12.4 mm. Each zone was machined using the same tool radius but with different feed rate, in order to obtain different roughness parameters for each zone (surface roughness increases from zone 1 to zone 4). This allows studying the influence of the amplitude of roughness parameters with respect to CT surface filtering characteristics.

For both samples, reference measurements were performed with a contact CMM (Zeiss Prismo Vast; MPE of length: 2 + L/300 μm, where L is the length in mm). Circular probing paths, orthogonal to the sample axis, were acquired in scanning mode. Roughness

measurements were performed by means of a contact roughness profiler (Zeiss TSK Surfcom 1400) and an optical profiler (Sensofar Plu Neox) applying cut-off filters according to ISO 4288 (ISO4288:1996). The FDM sample is characterized by an *Rp* value of 37 µm, whereas the *Rp* values obtained for the different zones (from 1 to 4) of the turned sample are respectively 11 µm, 16 µm, 29 µm and 33 µm.

Each sample was CT scanned using a metrological CT system (Nikon Metrology MCT 225). To vary the spatial resolution of the CT scans without changing other scanning parameters, the magnification factor was changed in a series of measurements, resulting in three different voxel sizes for the FDM sample (19 µm, 100 µm and 125 µm) and four different voxel sizes for the turned sample (17 µm, 50 µm, 91 µm and 125 µm). Both samples were scanned with low electron beam power to keep the X-ray focal spot at a minimum. This allowed studying the influence of the voxel size on measurement results for different *voxel size/Rz* ratios.

Each CT scan was analysed by means of the software VGStudio MAX 3.0 (Volume Graphics, Germany) using local advanced surface determination. For each sample, the same alignment used for the tactile CMM measurements was adopted, and each diameter was evaluated by fitting a cylinder with a height corresponding to the period of the profile, (e.g. 0.33 mm for the FDM sample). Fitting a cylinder instead of a circle was necessary to simulate the same probing areas interested by CMM measurements. Least-squares fitting was used for the evaluation (as it is widely used in CT dimensional measurements (Carmignato 2012), and a high density of fitting points was used so that they were well distributed on the whole roughness profile.

Simulation analyses

From experimental analyses it is difficult to isolate single influence quantities affecting CT measurement results and, in addition, CMM measurements are also influenced by high surface roughness, increasing the uncertainty of reference values. Therefore, simulation analyses were also performed, because they enable to study large numbers of profiles (including those difficult to be manufactured), use nominal dimensions as reference dimensions and isolate different influence quantities (e.g. voxel size and focal spot). Simulated CT scans were performed using Scorpius XLab (Fraunhofer EZRT, Germany) and analysed in VGStudio MAX 3.0 with advanced local surface extraction. To allow a high number of analyses was necessary to develop something faster and

simplified. For these reasons, numerical simulations were implemented in newly developed Matlab routines. A set of 16 bit grey scale images were generated for simulating CT bidimensional sections of cylinders (thus, image pixels will be hereafter referred as voxels), each featuring a specific roughness profile. This enabled to further extend the study with significant reduction of the required simulation time with respect to 3D simulations performed using Scorpius XLab. After verifying the consistency of the results with those obtained with Scorpius XLab on corresponding profiles, a large number of roughness profiles in between two extreme cases were analysed. Figure 111 shows an example of three different profiles: the additive profile, the turned profile and the ideal triangular profile.

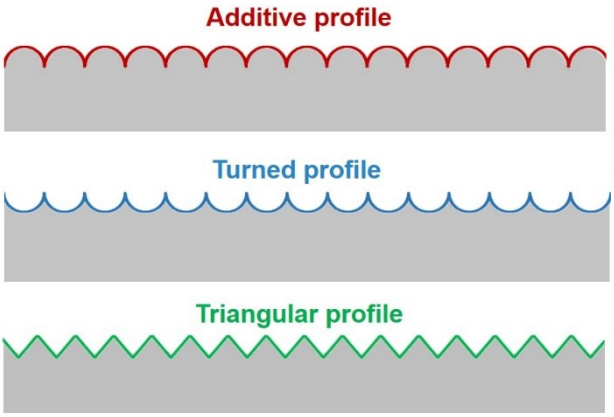

Figure 111 Example of three different and extreme surface roughness profiles

All the simulated profiles are in between the correspondent Abbott curves of the additive and turned profiles (red one and blue one in Figure 112, the green one is the triangular).

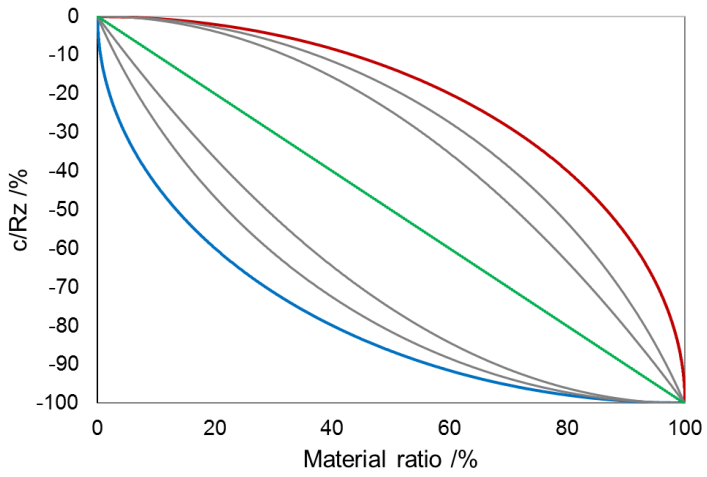

Figure 112 Abbott-Firestone curves of some studied profiles

Since all the investigated profiles were generated based on their analytical description, an ideal form characterizes them. For example, the turned profiles were created using a function in which the control parameters are *Rz* and *tool radius*. *Tool radius* is the ideal radius of the profile (tool radius is used in order to maintain an ideal connection with the machining process). Different turned profiles are characterized by completely different steepness of the peaks: increasing the *Rz* with the same *tool radius*, causes significant differences in the peaks morphology. In order to consider this characteristic, the ratio *RSm/Rz* was considered. *Table 56* summarises the ranges of *Rz* and *RSm* parameters used for the simulated roughness profiles. Clearly if the *Rz* and the *tool radius* are equal, this means that the profile is perfectly round.

	Nr. of profiles	***Rz* /µm**	***RSm* /µm**
Turned	11	[20, 125]	[135, 556]
FDM	11	[20, 125]	[135, 556]
Triangular	1	125	250

Table 56 Number of profiles and range of roughness parameters intervals used for profile generation.

Therefore, after the mathematical description of the profiles, the reference image is created using an ideal pixel of 0.5 µm. The diameter of the simulated cylinder is fixed to 4mm. The choice of a constant diameter was verified considering different diameters and verifying that the diameter does not influence the final result. The image is generated considering a matrix in which all the values in between the two profiles (bottom and top profile of the cylinder) are completely white, elsewhere is black. An example of a reference image is shown in figure Figure 113.

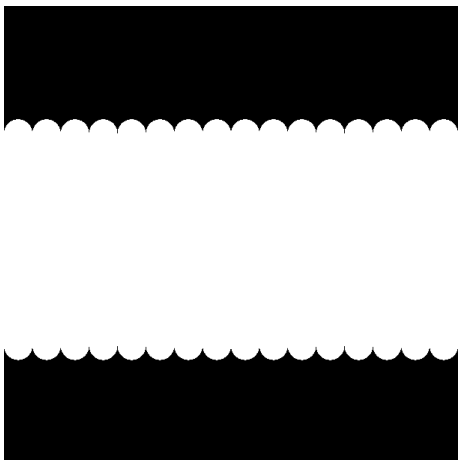

Figure 113 Example of a generated image

This is the starting image, necessary for the subsequent analysis. The reference images are used for the evaluation of the reference characteristics, that are evaluated on both image and numerical profile and compared in order to verify the reliability of the edge detection method. Starting from the reference image is possible to set-up the sensitivity analysis considering the voxel size and the partial volume effect. In Figure 114 both effects are shown. As clearly described from the figure, the voxel size effect is associated with the dimension of the voxel size used for the measurement of the component. Voxel size in this case is simplified with a pixel size effect, not considering the third dimension and simplifying the study in only two dimensions (mainly for the generalization).

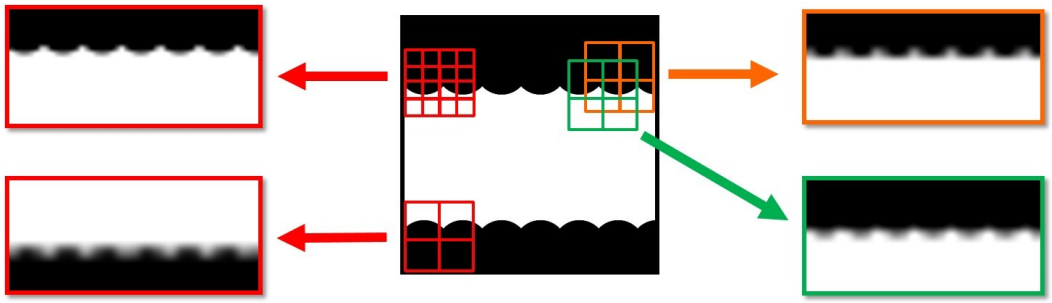

Figure 114 Voxel size and partial volume effect

The voxel size is influencing the quality and the definition of the edge. Instead of a perfect transition from white to black, a gradient of different greyscale levels is generated. Left part of Figure 114 presents two examples of pixel sizes: on the left-top the pixel size is small (10 μm) but also in that case it is evident the gradient, otherwise in the bottom-left image, the pixel is big (75 μm) and the edge is no more clearly understandable.

In order to simulate this effect, the reference matrix is discretized using matrices of different dimensions (simulating the dimensions of the pixel). The grey level of each new pixel of the new matrix is calculated considering all the pixels of the reference matrix contained inside and the dimension of the new pixel. The total sum of the values of each pixel is then divided by the number of pixels, obtaining the correspondent level of grey of the new pixel. In this way, edges are smoothed, because of the combined effect of the white part and the black part, causing different grey levels in between.

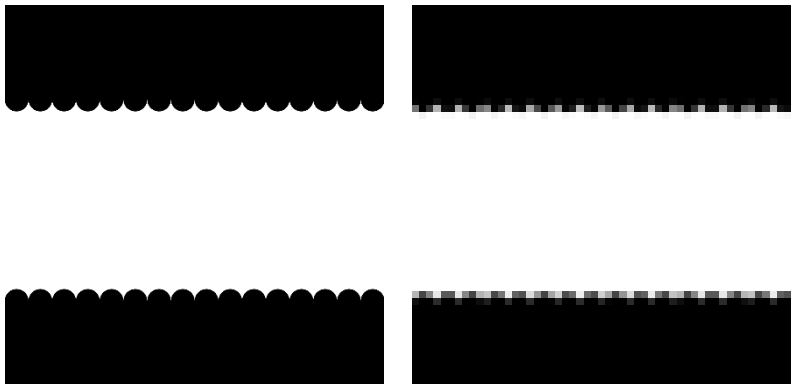

Figure 115 Example of images obtained from the same reference: on the left pixel size of 2.5 um and on the right pixel size of 75 um

Figure 115 shows an example of this effect, for the perfectly rounded turned profile (ideal profile). The dimension of the pixel was fixed according to the *Rz* value of the profile, in order to compare all the different profiles.

The second effect simulated is the position of the pixel respect to the surface roughness profile. If the pixel is centred on the peak, the obtained profile is completely different from the case of the profile centred on the valleys. This effect is well known as partial volume effect (Kruth et al. 2011). The morphology of the peaks (or valleys) is reconstructed in a completely different way because of this centring effect. This is obtained changing the alignment between the reference matrix and the matrix with the new pixel dimension.

Then, each profile was imaged with 20 different voxel sizes (from 1 μm to a maximum of $3 \cdot Rz$), obtaining 20 images with different resolutions for each profile. Moreover, because of the partial volume effect, a total amount of 81 different positions inside the pixel grid (i.e. combination of 9 different positions for both x and y directions) were considered for each investigated surface profile. In this way, for each profile a total amount of 1620 images (81 positions and 20 voxel sizes) was generated. The images were then processed automatically using an edge detection algorithm implemented in Matlab (Trujillo-Pino et al. 2013). From the extracted profiles, the measurands of interest depicted in Figure 116 (i.e. maximum, minimum and least-squares diameters) were evaluated. As previously said, the reference diameter used for the numerical simulations is computed using only the extreme peaks points determined from the analytical profile (i.e. reproducing an ideal CMM measurement probing only the peaks of the profile).

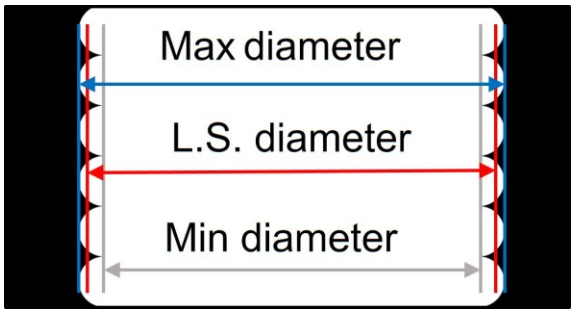

Figure 116 Measurands of interest: maximum diameter, least squares diameter and minimum diameter

Results

Results obtained from experimental investigations and numerical simulations are presented and compared. The results obtained form the experimental analysis are shortly described an used only for the validation of the numerical analysis.

Experimental results

The experimental results are shown in Figure 117. In the ordinate axis, the ratios between deviations b (calculated as CT measurements minus reference measurements) and Rp values are plotted, whereas in the abscissa axis the ratios between voxel sizes and Rz parameters are plotted. FDM samples are represented with crosses while the round are the turned profile (different colours for different roughness). Voxel size and bias are divided by Rz and Rp in order to allow comparing different profiles with different roughness characteristics scanned with different voxel sizes. The results presented in Figure 117 clearly point out that the bias with respect to the reference measurements is constant and independent from the surface roughness: least-squares CT measurements of outer diameters are smaller than reference measurements of approximately two times the *Rp* value of the scanned workpiece.

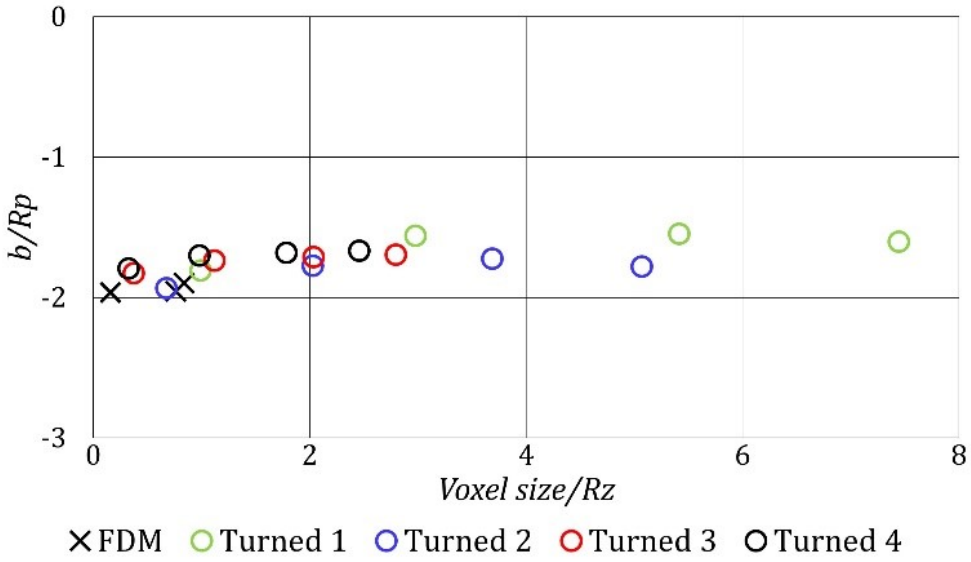

Figure 117 Results obtained from the experimental investigation. Diameter measurements of the FDM sample are represented as crosses, whereas results obtained for the different diameters measured in each zone (characterized by increasing roughness) of the turned

Moreover, the deviations experimentally found do not show significant variations with the different voxel sizes used in this work (up to 125 µm). In fact, it can be seen how varying the voxel size (i.e. *voxel size/Rz* ratio) for the given measurand, the *b/Rp* values are still close to -2*Rp*. Additional investigations were also conducted on another turned aluminium cylinder characterized by a lower surface roughness, with an *Rp* value of 2 µm. A higher dispersion of *b/Rp* values was found in this case. This can be explained because the surface roughness is not the predominant influence quantity among those that usually occur in CT measurements of parts with reduced surface roughness. While parts with high surface roughness produce higher values of b (resulting in systematic errors that should be corrected), for parts with small surface roughness the systematic effect is more difficult to be identified and, therefore, in this case the influence of surface roughness on CT measurements could be considered in the measurement uncertainty (e.g. using the methods proposed in (Bartscher et al. 2010) and (Schmitt & Niggemann 2010).

Simulation results

Figure 118 shows the results obtained through the numerical simulation. The deviations b are plotted in function of the voxel size (a-dimensionalized also in this case using the same parameters described in the previous paragraph). In this case the bias b is calculated as the difference between the least-squares diameter and the reference diameter

(maximum diameter evaluated on the reference image). Each point shown Figure 118 represents the average of 81 evaluations (considering the alignment of the voxel grid, 9 *y* translations and 9 *x* translations). The standard deviations were found to be within 3% of the voxel size.

Simulation results are in good agreement with experimental results: the deviations between least-squares diameters and reference diameters are constantly around -2*Rp* on average, independently from the profile roughness characteristics. In particular, simulation results are in between -1.9 and -2.1 *b/Rp* (except for voxel size/Rz < 0.2, for specific profiles). For *voxel size/Rz* ratios smaller than 0.2, the results related to profiles with the steepest peaks/valleys (i.e. FDM and turned profiles with smaller *RSm/Rz* ratio) present larger deviations (going outside the range between -1.9 and -2.1 *b/Rp*). This finding was caused by the edge detection algorithm: in proximity of very sharp peaks/valleys, the algorithm generates a distortion of the extracted edge surface. Consequently, a too high number of fitting points is selected around the peaks/valleys, causing the observed deviations. In addition, numerical simulations showed that profiles with the same *Rsm/Rz* ratio (for given FDM and turned profiles) yield results that are exactly overlapping in Figure 118.

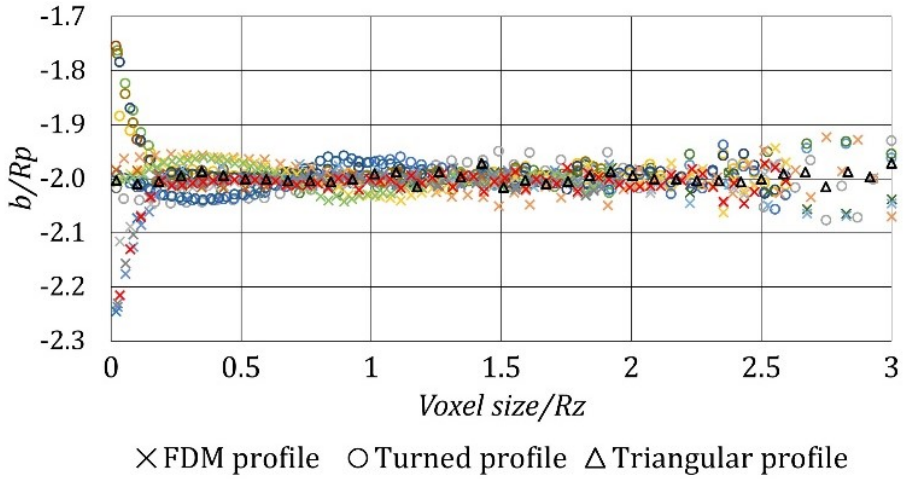

Figure 118 Results of the numerical simulations. FDM profiles are represented as crosses, turned profiles as circles, and triangular profiles as triangles.

Furthermore, the numerical analyses allowed assessing also the effects of voxel resolution on CT measurements of maximum and minimum diameters. Figure 115 shows as an example what was obtained, when applying the subpixel edge location algorithm

(Trujillo-Pino et al. 2013) for two different turned profiles (namely profile A and profile B) characterized respectively by: *Rz* = 50 µm and *RSm* = 557 µm (profile A), and Rz = 125 µm and RSm = 250 µm (profile B). Figure 119 shows the morphology of the two different profiles.

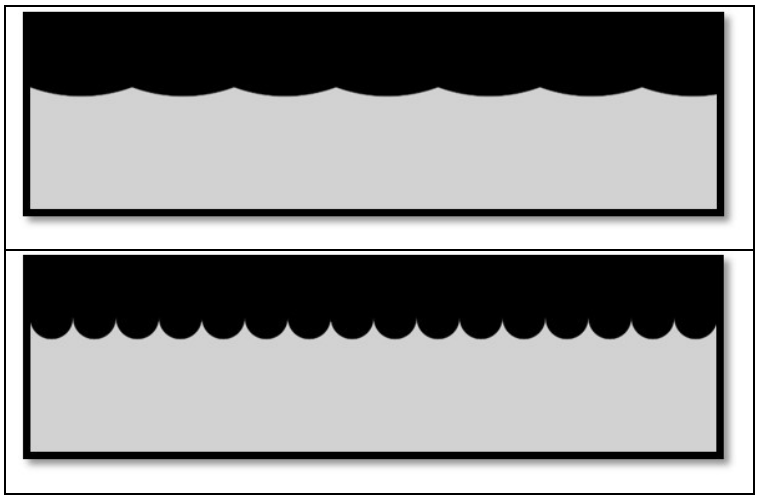

Figure 119 Profile used for the study on the maximum and minimum diameter: top image is profile A, bottom image represents profile B.

In both cases, the evaluated maximum diameter decreases as the voxel size increases, while the evaluated minimum diameter starts worsening in correspondence of larger voxel sizes because of the different morphology of the valley with respect to the peak. Thus, the filtering operation obtained by increasing the voxel size has a reduced effect on the least-squares diameters, but a significantly stronger effect on the maximum and minimum diameters. The decrease of the maximum diameter and the increase of the minimum diameter were found to be less pronounced for profile A than for profile B, which represents the extreme case analysed in this work with a *RSm/Rz* ratio equal to 2 (i.e. with steep peaks). In general, when analysing the maximum/minimum diameters, the combined effect of profile morphology and voxel size produces larger deviations for steeper peaks/valleys. All the considerations presented above are valid also for profiles mirrored with respect to the turned ones (i.e. profiles with the same characteristics of the turned profiles but mirrored Abbott curve). In this case, the minimum diameters increase as the voxel size increases, while the maximum diameters start worsening with larger voxel sizes.

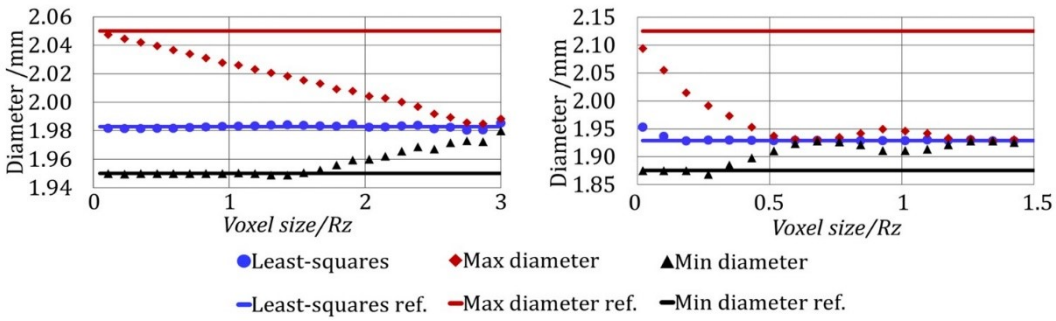

Figure 120 Example of the effect of the voxel size on maximum, minimum and least-squares diameters for profile A (left) and for profile B (right). Each point represents the mean value calculated on 81 different positions.

Moreover, the trends that characterize the variation of the maximum and minimum diameters with the voxel size were found to be dependent from the surface determination method applied. Therefore, it can be concluded that, when evaluating maximum or minimum diameters from CT scans, measurement results are affected by both the voxel size and the surface determination algorithm used, depending on the specific roughness profile that is analysed.

Conclusions

In this work, the influence of surface roughness on CT dimensional measurements was investigated by experimental and simulation analyses on periodic roughness profiles. CT scans of FDM and turned cylinders featuring various surface topographies were performed using different voxel sizes up to 125 µm. From the experimental results, diameters measured by CT using least-squares fitting were found to be smaller than reference measurements of approximately $2Rp$ on average.

This systematic difference was confirmed for different voxel sizes. Simulated analyses were performed in order to deepen the study on a set of simulated CT sections (2D images) reproducing a high number of different roughness profiles (e.g. FDM, turned, triangular). Each profile was imaged at various voxel sizes and considering several different positions inside the pixel grid to take into account the partial volume effect. Simulation results show that mean deviations (between least-squares diameters and reference diameters) of $2Rp$ take place independently from the profile roughness characteristics. However, when using large voxel sizes, the expected standard deviations increase; for example, when using the subpixel edge location algorithm based on partial area effect, standard deviations were found to be within 3% of the voxel size.

The effect of surface roughness in this work was investigated by performing bidirectional measurements, i.e. evaluating diameters of cylindrical parts. However, it could be generalized also for other types of measurements (e.g. position of flat surfaces) by considering an offset equal to *Rp* of the CT least-squares surface from the reference surface measured on the peaks.

It was also shown that maximum and minimum diameters evaluated from CT scans are affected by both voxel size and surface determination algorithm used, depending on the specific roughness profile that is analysed. The combined effect of profile morphology and voxel size is significantly stronger in this case than for least-squares diameters, and produces larger deviations for steeper peaks/valleys.

Finally, additional investigations were performed to show how CT dimensional measurements on rough parts are influenced by other factors, such as focal spot size, surface determination method and fitting operations. Further work is planned to extend these investigations to other cases.

Conclusions

In this thesis, four different models for enhancing optical measurements were presented. Different fields of application were analysed and different solutions were found, ensuring in the different cases an improvement of the instrument capabilities and a reduction of the process source of uncertainty. A correction method for the measurement of threads with optical systems was studied and validated. Starting from the solutions provided by different optical measuring systems factories and analysing the limitations of the different methods, was developed a more flexible and general correction. A sensitivity analysis brought to an inverse relation used for the correction of the shadow profile without any a-priori information. The pitch diameter presents a standard deviation lower than 1 μm and this confirms the repeatability of the correction on the different flanks, moreover the overall differences between the reference value and the corrected ones are lower than 20 μm. Moreover, considering a systematic error on the external diameter the differences are reduced under 10 μm. The study on the interaction between surface roughness and CT dimensional measurement brought to a generalized conclusion. A numerical simulation enlarged the number of roughness profiles and voxels sizes. This numerical approach confirmed that mean deviations between least –squares diameters and reference diameters is *2Rp* independently from the profile roughness characteristic. This systematic difference generalizes the experimental results and confirms that the effect of the surface roughness could be considered as a systematic effect instead of an uncertainty contribution. Numerical sensitivity analysis also confirms that the surface roughness parameters evaluated on the reconstructed surfaces are less influenced by the presence of void pixels. In this case was demonstrated that the interpolation of the void pixels reduces the variability of the calculated surface parameters. The relation between the absolute value of the variability and the percentage of void pixels was found for *Sa, Ssk* and *Sku*. The effect of the random distributed void pixels on *Sa* parameter causes a variability on the determination of the parameter described by $u=0.006*\%Void$ for the reconstructed surfaces and $u=0.01*\%Void+0.02$ for the not-reconstructed ones. For all the parameters under investigation, was demonstrated that the calculation on the reconstructed topography ensures lower variability. Finally, enhancement of the confocal microscopy was also reached through an uncommon use of the void pixels. Confocal microscopy topographies taken from a micro-machined slot were managed in order to control the

burrs dimensions. A method that combines 3D data and image processing tools was developed and applied. The results are confirmed by the evaluation developed on the SEM images. The effect of depth of cut and cutting speed were finally correlated with the mean burr width. This newly developed method permits to control the quality of the machined slot with a single, fast and non-invasive measuring phase.

Bibliography

Aloisi, V. & Carmignato, S., 2016. Influence of surface roughness on X-ray computed tomography dimensional measurements of additive manufactured parts. *Case studies in nondestructive testing and evaluation*, 6(1), pp.104–110.

Aloisi, V., Carmignato, S. & Savio, E., 2015. Effect of surface roughness on uncertainty of X-ray CT dimensional measurements of additive manufactured parts. *Proceedings of the 15th International Conference of the European Society for Precision Engineering and Nanotechnology, EUSPEN 2015*, pp.187–188.

Andreini S., 2012. Metodo di determinazione optoelettronica di parametri di filettatura. *Italian patent Nr. ITRN20110031 (A1)*.

Aramcharoen, a. & Mativenga, P.T., 2009. Size effect and tool geometry in micromilling of tool steel. *Precision Engineering*, 33(4), pp.402–407.

Aurich, J.C. et al., 2009. Burrs-Analysis, control and removal. *CIRP Annals - Manufacturing Technology*, 58(2), pp.519–542.

Aurich, J.C. et al., 2009. Burrs—Analysis, control and removal. *CIRP Annals - Manufacturing Technology*, 58(2), pp.519–542.

Bartscher, M. et al., 2010. Performance assessment of geometry measurements with micro-CT using a dismountable work-piece-near reference standard. *10th European Conference on Non-Destructive testing*.

Bergstrom, D., 2008. *The absorption of laser light by rough metal surfaces*. Luleå University of Technology.

Bissacco, G., Hansen, H.N. & De Chiffre, L., 2006. Size Effects on Surface Generation in Micro Milling of Hardened Tool Steel. *CIRP Annals - Manufacturing Technology*, 55(1), pp.593–596.

Blateyron, F., 2011. Chromatic confocal microscopy. In R. K. Leach, ed. *Optical Measurement of Surface topography*. Springer, Berlin, Heidelberg, pp. 71–105.

Boeckmans, B. et al., 2015. eu spen ' s 15 th International Conference & Roughness offset differences between contact and non-contact measurements. , (June),

pp.189–190.

Bruzzone, A.A.G. et al., 2008. Advances in engineered surfaces for functional performance. *CIRP Annals - Manufacturing Technology*, 57(2), pp.750–769.

Butte, V.K. & Tang, L.C., 2008. Engineering process control: a review. In B. M. Krishna, ed. *Handbook of performability engineering*. Springer London, pp. 203–223.

Câmara, M.A. et al., 2012. State of the Art on Micromilling of Materials, a Review. *Journal of Materials Science and Technology*, 28(8), pp.673–685.

Carmignato, S., 2012. Accuracy of industrial computed tomography measurements: Experimental results from an international comparison. *CIRP Annals - Manufacturing Technology*, 61(1), pp.491–494. Available at: http://dx.doi.org/10.1016/j.cirp.2012.03.021.

Carmignato, S. et al., 2017. Influence of surface roughness on computed tomography dimensional measurements. *CIRP Annals - Manufacturing Technology*, 66(1), pp.499–502. Available at: http://dx.doi.org/10.1016/j.cirp.2017.04.067.

De Chiffre, L. et al., 2014. Industrial applications of computed tomography. *CIRP Annals - Manufacturing Technology*, 63(2), pp.655–677. Available at: http://dx.doi.org/10.1016/j.cirp.2014.05.011.

Colledani, M. et al., 2014. Design and management of manufacturing systems for production quality. *CIRP Annals - Manufacturing Technology*, 63(2), pp.773–796.

EURAMET, 2007. Determination of Pitch Diameter of Parallel Thread Gauges by Mechanical Probing. , 1(July).

Fang, F.Z. et al., 2017. Nanomanufacturing—Perspective and applications. *CIRP Annals - Manufacturing Technology*, 66(2), pp.683–705. Available at: http://dx.doi.org/10.1016/j.cirp.2017.05.004.

Fiedler, D. et al., Misurazioni dimensionali di un tomografo industriale 2D : influenza della rugosità del componente.

Filiz, S. et al., 2007. An experimental investigation of micro-machinability of copper 101 using tungsten carbide micro-endmills. *International Journal of Machine*

Tools and Manufacture, 47(7–8), pp.1088–1100.

Gonzalez, R. & Woods, R., 2008. *Digital image processing* 2nd editio., Pearson Education.

Hocken, R.J., Chakraborty, N. & Brown, C., 2005. Optical Metrology of Surfaces. *CIRP Annals - Manufacturing Technology*, 54(2), pp.169–183.

Hocken, R.J. & Pereira, P.H., 2017. *Coordinate measuring machines and systems*, CRC Taylor & Francis Group.

Hunsicker, R.J. et al., 1994. Automatic Vision Inspection and measurement system for external screw threads. *Journal of Manufacturing Systems*, 13(5), pp.360–384.

Ismail, M.F., Yanagi, K. & Fujii, A., 2010. An outlier correction procedure and its application to areal surface data measured by optical instruments. *Measurement Science and Technology*, 21(10), p.105105.

ISO13565-2:1996, Geometrical Product Specifications(GPS) - Surface texture: Profile method: Surfaces having stratified functional properties-Part 2:Height characterization using the linear curve.

ISO16610-30:2015, Geometrical Product Specification (GPS) - Filtration - Part 30: Robust profile filters:basic concepts.

ISO16610-60:2015, Geometrical Product Specification (GPS) - Filtration - Part 60: Linear areal filters: Basic concepts. , (November).

ISO25178-2:2012, Geometrical Product Specification (GPS)-Surface texture: areal - part 2: Terms, definitions and surface texture parameters.

ISO261:1998, ISO general purpose metric screw threads-General plan.

ISO4287:1997, *Geometrical Product Specifications(GPS) - Surface texture: Profile method - Terms, definitions and surface texture parameters*,

ISO4288:1996, Geometrical Product Specifications(GPS) - Surface texture: Profile method - Rules and procedures for the assessment of surface texture.

ISO5408:2009, Screw threads-Vocabulary.

ISO5436-1:2000, Geometrical Product Specifications(GPS) - Surface texture: Profile

method - Part 1: material measures.

ISO724:1993, ISO general purpose metric screw threads-Basic dimensions.

ISO965-1:2013, ISO general purpose metric screw threads-Tolerances-Part 1: Principles and basic data.

Jahanmir, S., 2011. Surface integrity in ultrahigh speed micromachining. In *Procedia Engineering*. pp. 156–161.

Jiang, J. & Zhang, Q., 2012. Research on screw thread vision measurement. *Advanced materials research*, 346, pp.600–606.

Junhua, C., Xiancheng, W. & Shaofeng, S., 2011. Method for eliminating error of cylinder screw thread non-contact measurement. *Chinese Patent CN102221349 (B)*.

Kiswanto, G., Zariatin, D.L. & Ko, T.J., 2015. The effect of spindle speed, feed-rate and machining time to the surface roughness and burr formation of Aluminum Alloy 1100 in micro-milling operation. *Journal of Manufacturing Processes*, 16(4), pp.435–450.

Ko, S. & Park, S., 2006. Development of an effective measurement system for burr geometry. *Proc. IMechE*, 220, pp.507–512.

Kosarevsky, S., 2010. Alignment problem while measuring thread pitch of large thread gauges on the profile-measuring machines. *International Journal of Advanced Manufacturing Technology*, 48(1–4), pp.267–272.

Kou, Z. et al., 2015. Burr Controlling in Micro Milling with Supporting Material Method. *Procedia Manufacturing*, 1, pp.501–511.

Kratsch, N., 2008. Method for optoelectronic determination of screw thread parameters, whereby a shadow image of the thread is generated and a correction value determined by comparison of measured thread pitch and diameter values with known values. *German Patent Nr.DE10152038 (C5)*.

Kruth, J.P. et al., 2011. Computed tomography for dimensional metrology. *CIRP Annals - Manufacturing Technology*, 60(2), pp.821–842. Available at: http://dx.doi.org/10.1016/j.cirp.2011.05.006.

Kumar, P. et al., 2017. Recent advances in characterization, modeling and control of burr formation in micro-milling. *Manufacturing Letters*, 13, pp.1–5. Available at: http://linkinghub.elsevier.com/retrieve/pii/S221384631730007X.

Kunzmann, H., Pfeifer, T. & Schmitt, R., 2005. Productive metrology-Adding value to manufacture. *CIRP Annals- Manufacturing Technology*, 54(1), pp.155–168. Available at: http://www.sciencedirect.com/science/article/pii/S0007850607600249.

Leach, R., 2013. Welcome to surface topography: Metrology and properties. *Surface Topography: Metrology and Properties*, 1(1).

Leach, R.K., 2011. *Optical Measurement of Surface Topography*,

Lee, K. & Dornfeld, D.A., 2005. Micro-burr formation and minimization through process control. *Precision Engineering*, 29(2), pp.246–252.

Lonardo, P.M. & Bruzzone, A.A.G., 2000. No Title. *CIRP Annals*, 40(1), pp.427–430.

Lotze, W. & Will, J., 1991. Measurement By Optical Coordinate Measuring Systems. , 9(4), pp.153–156.

MacAulay, G., 2015. *Characterization of structured surfaces and assessment of associated measurement uncertainty*, National Phisical Laboratory.

Marinello, F. et al., 2007. Increase of maximum detectable slope with optical profilers, through controlled tilting and image processing. *Measurement Science and Technology*, 18(2), pp.384–389. Available at: http://stacks.iop.org/0957-0233/18/i=2/a=S09?key=crossref.d6b65036c415a3c50adc7a336759a27d.

Medeossi, F. et al., 2016. Effect of void pixels on the quantification of surface topography parameters. *Proceedings of the 16th International Conference of the European Society for Precision Engineering and Nanotechnology, EUSPEN 2016*.

Medeossi, F. et al., 2017. Micro-milling tool wear monitoring through a novel method for burrs evaluation. *Proceedings of the 17h International Conference of the European Society for Precision Engineering and Nanotechnology, EUSPEN 2017*.

Mian, A.J., Driver, N. & Mativenga, P.T., 2010. A comparative study of material phase effects on micro-machinability of multiphase materials. *The International Journal*

of Advanced Manufacturing Technology, 50(1–4), pp.163–174.

Özel, T. et al., 2011. Experiments and finite element simulations on micro-milling of Ti–6Al–4V alloy with uncoated and cBN coated micro-tools. *CIRP Annals - Manufacturing Technology*, 60(1), pp.85–88.

Piquard, R. et al., 2014. Micro-end milling of NiTi biomedical alloys, burr formation and phase transformation. *Precision Engineering*, 38(2), pp.356–364. Available at: http://dx.doi.org/10.1016/j.precisioneng.2013.11.006.

Salzinger, M., Hornberger, P. & Hiller, J., 2016. Analysis and comparison of the surface filtering characteristics of computed tomography and tactile measurements. , 1(iCT), pp.1–8.

Savio, E., 2012. A methodology for the quantification of value-adding by manufacturing metrology. *CIRP Annals - Manufacturing Technology*, 61(1), pp.503–506. Available at: http://dx.doi.org/10.1016/j.cirp.2012.03.019.

Savio, E. et al., 2016. Economic benefits of metrology in manufacturing. *CIRP Annals - Manufacturing Technology*, 65(1), pp.495–498. Available at: http://dx.doi.org/10.1016/j.cirp.2016.04.020.

Schmitt, R. & Niggemann, C., 2010. Uncertainty in measurement for x-ray-computed tomography using calibrated work pieces. *Measurement Science and Technology*, 21(5), p.54008.

Schwenke, H. et al., 2002. Optical methods for dimensional metrology in production engineering. *CIRP Annals-Manufacturing Technology*, 51(2), pp.685–699.

Senin, N., Blunt, L.A. & Tolley, M., 2012. Dimensional metrology of micro parts by optical three-dimensional profilometry and areal surface topography analysis. *Proceedings of the Institution of Mechanical Engineers, Part B: Journal of Engineering Manufacture*, 226(11), pp.1819–1832. Available at: http://journals.sagepub.com/doi/10.1177/0954405412461240.

Senin, N., Blunt, L. & Tolley, M., 2012. The use of areal surface topography analysis for the inspection of micro-fabricated thin foil laser targets for ion acceleration. *Measurement Science and Technology*, 23(10), p.105004. Available at: http://stacks.iop.org/0957-

0233/23/i=10/a=105004?key=crossref.3a4e0521f8e4cafeb99fc37660386139.

Shchurov, I.A., 2011. Calculation of the virtual pitch thread diameter using the cloud of points from CMM. *International Journal of Advanced Manufacturing Technology*, 53(1–4), pp.241–245.

Sheng, C., Dongbiao, Z. & Yonghua, L., 2014. A New Compensation Method for Measurement of Thread Pitch Diameter by Profile Scanning. , 14(6), pp.323–330.

Stanley, P.J. & Lawrence, J.Z., 2011. Apparatus and methods for measuring at least one physical characteristic of a threaded object. *United Sates Patent US8039827 (B2)*.

Takata, S. et al., 2004. Maintenance: Changing Role in Life Cycle Management. *CIRP Annals*, 53(2), pp.643–655. Available at: http://www.sciencedirect.com/science/article/pii/S000785060760033X?via%3Dihub [Accessed October 29, 2017].

Thepsonthi, T. & Özel, T., 2012. Multi-objective process optimization for micro-end milling of Ti-6Al-4V titanium alloy. *The International Journal of Advanced Manufacturing Technology*, 63(9–12), pp.903–914.

Trujillo-Pino, A. et al., 2013. Accurate subpixel edge location based on partial area effect. *Image and Vision Computing*, 31(1), pp.72–90. Available at: http://dx.doi.org/10.1016/j.imavis.2012.10.005.

Tsai, D. & Lu, W., 1996. Detecting and locating burrs of industrial parts. *International journal of production research*, 34(1), pp.3187–3205.

Vipindas, K., Kuriachen, B. & Mathew, J., 2016. Investigations into the effect of process parameters on surface roughness and burr formation during micro end milling of TI-6AL-4V. *The International Journal of Advanced Manufacturing Technology*. Available at: http://link.springer.com/10.1007/s00170-016-9210-3.

Wang, Y. & Feng, H.Y., 2014. Modeling outlier formation in scanning reflective surfaces using a laser stripe scanner. *Measurement: Journal of the International Measurement Confederation*, 57, pp.108–121. Available at: http://dx.doi.org/10.1016/j.measurement.2014.08.010.

Weckenmann, A. et al., 2004. Probing Systems in Dimensional Metrology. *CIRP Annals - Manufacturing Technology*, 53(2), pp.657–684. Available at:

http://www.sciencedirect.com/science/article/pii/S0007850607600341%5Cnhttp://linkinghub.elsevier.com/retrieve/pii/S0007850607600341.

Xiaomei, Z., 1989. *Applikationsuntersuchung zu einem neuen optischen Gewindemessverfahren auf Ko-ordinatenmessgeraeten*. TU Dresden.

Yoshizawa, T., 2015. *Handbook of optical metrology*, CRC Taylor & Francis Group.

Ringraziamenti

Un grazie particolare agli amici di sempre.

Ringrazio il Prof. Savio per la guida in questi tre anni di Dottorato e ringrazio il Prof. Carmignato per la passione, la dedizione e l'entusiasmo con cui mi ha coinvolto nella ricerca.

Ringrazio il Prof. Richard Leach per avermi ospitato alla University of Nottingham.

Infine ringrazio il gruppo Mètis e il Prof. Lazzaretto per questi tre anni trascorsi insieme a costruire, rompere e ricostruire sempre con il sorriso, con l'entusiasmo e con la forza di una passione profonda e inguaribile per la vela e per il mare.

Nunc est bibendum, nunc pede libero pulsanda tellus